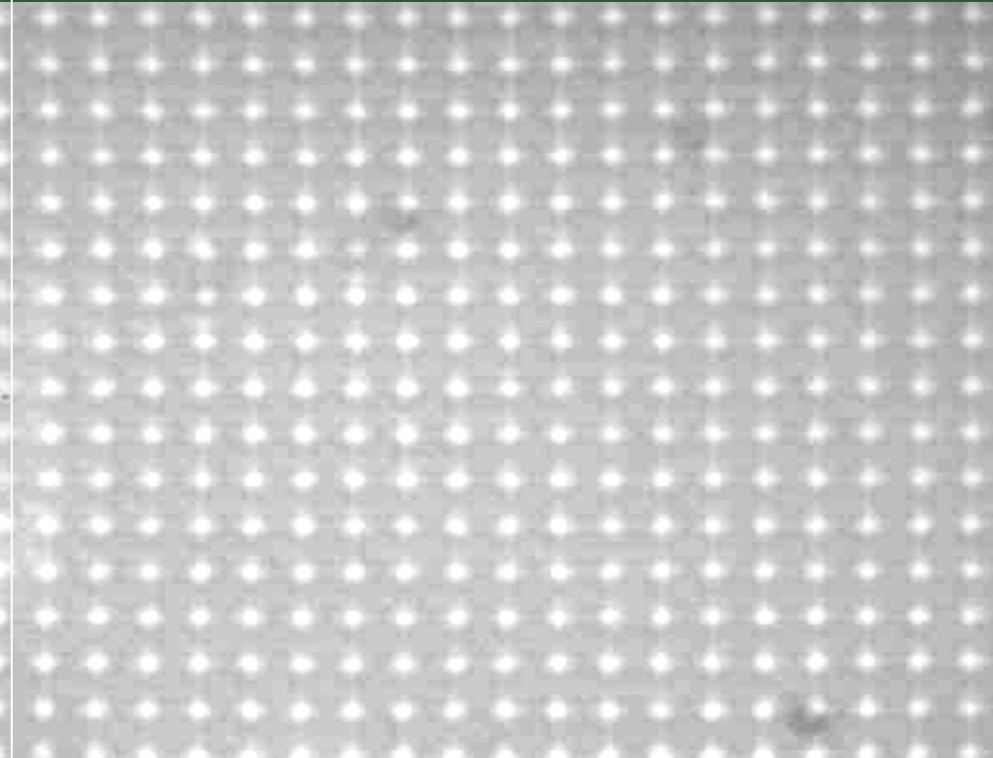
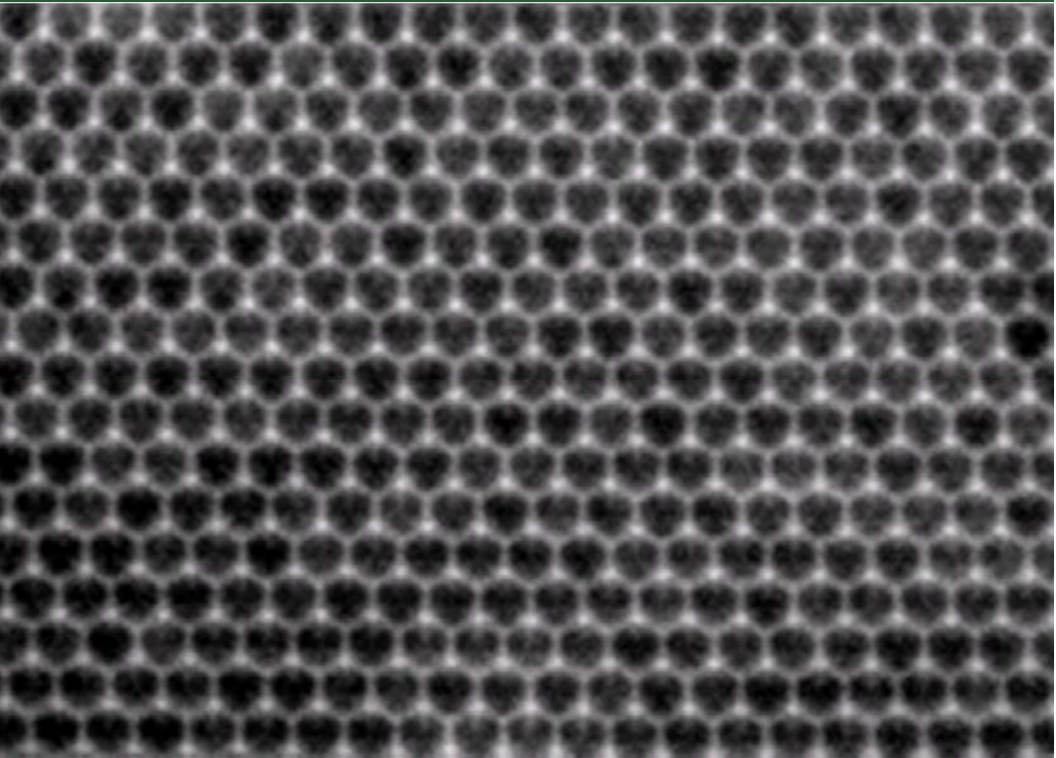


Two-phase Flow in Micro- and Nanofluidic D

Lingling Shui

Two-phase Flow in Micro and Nanofluidic Devices

2009



N: 978-90-365-2836-8

Lingling

Two-phase Flow in Micro and Nanofluidic Devices

The research described within this thesis was carried in the BIOS/Lab-on-a-Chip group at the MESA+ Institute for Nanotechnology at the University of Twente, Enschede, the Netherlands. The NanoNed financially supported this research through a Nanofluidics Flagship (project no.: TMM 6444).

Committee members:

Chairman

Prof. Dr. Ir. A.J. Mouthaan University of Twente

Promotor

Prof. Dr. Ir. A. van den Berg University of Twente

Assistant promotor

Dr. J. C. T. Eijkel University of Twente

Members

Prof. Dr. F. G. Mugele University of Twente

Prof. Dr. Ing. M. Wessling University of Twente

Prof. Dr. Ir. J. den Toonder TU Eindhoven/Philips

Prof. A. Hibara University of Tokyo

Dr. E. S. Kooij University of Twente

Title: Two-phase Flow in Micro and Nanofluidic Devices

Author: Lingling Shui

ISBN: 978-90-365-2836-8

Publisher: Wohrmann Print Service, Zutphen, the Netherlands

Cover pictures: Monodispersed femtoliter droplets organizing into 3D fcc structures in microchannels, (100) plane (front cover) and (111) plane (back cover).

Copyright © 2009 by Lingling Shui, Enschede, the Netherlands

**TWO-PHASE FLOW IN
MICRO AND NANOFUIDIC DEVICES**

DISSERTATION

to obtain
the degree of doctor at the University of Twente
on the authority of the rector magnificus,
prof. dr. H. Brinksma,
on account of the decision of the graduation committee,
to be publicly defended
on Thursday the 14th of May 2009 at 16:45 hrs

by

Lingling Shui

Born on the 28th of September 1977

in Anhui, China

Dit proefschrift is goedgekeurd door

Promotor: Prof. Dr. Ir. Albert van den Berg

Assistant promotor: Dr. Jan C. T. Eijkel

Table of Contents

1 Introduction	1
1.1 Introduction to Two-Phase Flow	2
1.2 Project Aims	3
1.3 Thesis Outline	3
References	5
2 Multiphase Flow in Micro- and Nanochannels - Pumping Methods	7
2.1 Introduction	8
2.2 Actuation Forces	10
2.2.1 Self-pumping	13
2.2.2 Non-mechanical pumping methods.....	15
2.2.3 Mechanical pumping methods.....	17
2.3 Flow Phenomena	20
2.3.1 Flow patterns	22
2.3.2 Flow profiles	24
2.3.3 Film flow and corner flow	24
2.3.4 Slip flow	27
2.4 Conclusions and Outlook	29
References	30
3 Multiphase Flow in Microfluidic Systems - Control and Applications of Droplets and Interfaces	35
3.1 Introduction	36
3.2 Controlling Multiphase Flow in Microfluidic Systems	37
3.3 Applications of Multiphase Microfluidic Flows	44
3.3.1 Droplet-based flows	45
3.3.2 Stratified flows (interfaces)	55
3.4 Conclusions and Outlook	61
References	62
4 Capillary instability, Squeezing and Shearing in Head-on Microfluidic Channels	67
4.1 Introduction	68

4.2 Experimental	70
4.3 Results and Discussion	72
4.3.1. Geometry-determined dripping - capillary instability	74
4.3.2. Flow-rate-dependent dripping - squeezing	77
4.3.3. Flow-rate-dependent jetting - shearing.....	79
4.3.4. Geometry-determined jetting - capillary instability.....	81
4.3.5. Threading.....	82
4.4 Conclusions and Outlook	83
References	84
5 Geometry-Controlled Droplet Generation in Head-on Microfluidic Devices	85
5.1 Introduction	86
5.2 Experimental	86
5.3 Results and Discussion	87
5.4 Conclusions and Outlook	92
References	92
6 Interfacial Tension Controlled W/O and O/W 2-Phase Flow in Microchannels	95
6.1 Introduction	96
6.2 Experimental	100
6.2.1 Chip fabrication.....	100
6.2.2 Surface modification of microchannels.....	101
6.2.3 Preparation of fluids	102
6.3 Results and Discussion	103
6.3.1 Emulsion types at the macroscale.....	103
6.3.2 Emulsions in microchannels.....	104
6.3.3 Emulsion inversion in microchannels.....	107
6.4 Conclusions and Outlook	108
References	109
7 Two-Phase Flow in Nanochannels	111
7.1 Introduction	112
7.2 Experimental	114
7.2.1 Device design	114
7.2.2 Fabrication and setup.....	115

7.2.3 Fluids.....	115
7.3 Results and Discussion	116
7.3.1 Flow control in nanochannels.....	116
7.3.2 Miscible two phases mixing in nanochannels	119
7.3.3 Immiscible two phases flow in nanochannels	121
7.4 Conclusions and Outlook.....	123
References	123
8 Monodisperse Femtoliter Droplet Formation using Nanochannel-Microchannel Interfaces.....	125
8.1 Introduction	126
8.2 Experimental.....	128
8.3 Results and Discussion	129
8.3.1 Droplet formation at the nanochannel-microchannel interface	129
8.3.2 The dependence of the droplet size on the nanochannel height	132
8.3.3 Transitions.....	134
8.4 Conclusions and Outlook.....	136
References	137
9. Liquid Crystallography: 3D Microdroplet Arrangements Using Microfluidics.....	139
9.1 Introduction	140
9.2 Experimental.....	141
9.2.1 Device design	141
9.2.2 Fabrication and setup.....	142
9.2.3 Fluids.....	142
9.3 Results and Discussion	143
9.3.1 3D microdroplet arrangements	143
9.3.2 Liquid crystallography	146
9.3.3 Phase transition.....	148
9.4 Conclusions and Outlook.....	149
References	150
10 Summary and Recommendations.....	151
10.1 Summary.....	152
10.2 Recommendations and Proposals for Further Investigations.....	154
10.2.1 Materials.....	154

10.2.2 Chip design..... 156
10.2.3 Proposals 157

Acknowledgements 159

Publications 162

Chapter 1

Introduction

This chapter introduces the field of two-phase micro- and nanofluidics and formulates the aim of this project. An overview is given of the investigation of two-phase micro- and nanofluidics. We relate the possibilities of this field to the experimental work. The introduction ends with a brief description of each chapter.

1.1 Introduction to Two-Phase Flow

Two-phase micro- and nanofluidics means that two immiscible fluids are introduced and manipulated at the micro- and nanoscale. The study of two-phase micro- and nanofluidics has to include two factors. One is the nature of the immiscible fluids which can be of different chemical compositions – liquid/liquid, or in different physical states – gas/liquid. The other one is the properties of the devices which are to be scaled down to the micro- and nanoscale.

In the past decade, micro- and nanofluidics has been studied in great detail because of the increasing availability of methods for fabricating complicated flow configurations and measuring transport phenomena at the micro- and nanoscale. The micro- and nanofluidic systems with integrated pumps, valves, and detectors are known as “Lab-on-a-Chip” (LOC) or “Micro-total-analysis-system” (μ TAS) [1]. Ideally, every process necessary – e.g. sampling, sample pretreatment, reaction, separation, detection and analysis in an analytical system – is realized in one integrated device. Fluid mechanics studies of these processes therefore also are indispensable for the design and fabrication of LOC and μ TAS.

Fluids that are of interest in nature, biotechnology and chemistry are rarely simple single-phase fluids. Most studies of compartmental chemistry and interfacial phenomena and their applications employ two-phase flows. It is therefore not surprising that recently a surge of interest has arisen in two-phase microfluidic manipulation. When two phases flow together in the same conduit or channel, the flow patterns change between droplet-based flows and stratified flows depending on the physicochemical properties of fluids and channel surfaces [2-10]. Droplet-based flows consist of discrete volumes of fluids, whereas stratified flows rely on fluids which flow in parallel through the system with stable interfaces. Both the individual fluid phases and the interfaces between immiscible fluids offer useful tools that have been applied in many fields. At the same time, in two-phase flow systems, several flow phenomena, such as film flow, corner flow and slip flow play increasingly important roles with

reduction of the dimensions.

Compared to single-phase flow systems or unconfined systems, many questions arise when discussing multiphase flow in micro- and nanochannels even in a simple configuration. Both advantages and disadvantages originate from the confinement in a channel, the reduction in dimension and the coexistence of multiple phases. Manipulating fluids in such systems is much more complicated than in unconfined systems or single-phase systems. The flow of fluids within enclosed channels of glass, silicon, or plastics can be actuated spontaneously, non-mechanically or mechanically. Since the hydrodynamic resistance increases because of the confinement, the most used pumping method– syringe pumping – will be increasingly difficult to use in nanochannels due to the reduction in dimension. The best pumping principle for single-phase channel-flow, named electro-osmotic-flow, can not easily be used for driving because of the coexistence of multiple phases of widely varying conductivity. In view of these considerations, we have employed syringe pumping throughout this thesis, and dealt with the high actuation pressures and low flow rates in nanochannels by designing special dedicated channel layouts with bypasses.

1.2 Project Aims

The aim of this project was to investigate and develop micro- and nanofluidic structures for the creation and manipulation of liquid or gas pockets, and to design devices for the production of extremely small (femtoliter) droplets. Ultimately, trains of such femtoliter droplets could be guided through a network and find application in single (bio)molecule studies or high-throughput low-volume combinatorial chemistry. The project was financed by NanoNed through a Nanofluidics Flagship project number TMM 6444.

1.3 Thesis Outline

In this thesis, we report experiments on oil-water two-phase flow in microchannels

(5~20 μm), nanochannels (100~1000 nm) and at the interface of nanochannel and microchannel. Besides the introduction chapter, this thesis contains two review chapters (2 and 3), six experimental chapters (4-9) and a summary and recommendations chapter (10).

Chapter 2 describes different fluid pumping principles for two-phase flows, mainly providing the way to select an available and versatile pumping method for multiphase flow in micro- and nanochannels.

Chapter 3 focuses on control and applications of two-phase micro- and nanofluidics. Both droplet-based and stratified flows in micro- and nanofluidics find their ways in applications in different fields.

In chapter 4, we present a flow map of two-phase microfluidics in a new type of channel design. We investigated two-phase (oil and water) flow in a head-on microfluidic device operated with the two identical channels as inlets and the “long leg” as a constriction channel leading to a wider outlet section. Over a broad range of capillary numbers, $Ca \in (10^{-6}, 10^{-1})$, the two-phase diagram shows dripping, jetting and threading flow regimes which are interpreted as resulting from the mechanisms of capillary instability, squeezing and shearing by considering the contribution of different forces acting at the oil/water interface.

In chapter 5, we studied a new droplet formation regime in the head-on microfluidic devices. For capillary numbers (Ca) of approximately 10^{-5} or less, we find a Ca -independent droplet volume equal to the volume of the constriction channel, which decreases at higher Ca when shear forces become relevant. The droplet generation mechanism is explained in terms of a global capillary instability involving surprisingly stable intermediate surface configurations.

Chapter 6 discusses the role of interfacial forces in micro- and nanofluidic devices. We modulated solid-liquid and liquid-liquid interfacial forces using chemicals. By combination of different interfacial forces, we could determine the emulsion type (water-in-oil or oil-in-water), droplet deformation, coalescence, and even obtain emulsion inversion in the same microchannel.

Chapter 7 presents the development of devices to study oil and water two phases flow in nanochannels. We developed a flow control method to smoothly manipulate liquid in nanochannels with flow rates as low as $\text{pL}\cdot\text{s}^{-1}$. Using this method, we investigated the mixing of two miscible liquids and flows of two immiscible liquids in nanochannels.

In chapter 8, we report specific properties of devices with a nanochannel-microchannel interface for two-phase flows. The creation of stable and monodisperse attoliter to femtoliter size droplets was obtained at the nanochannel-microchannel interface in a wide range of flow rates and ratios.

In chapter 9, we report on the properties of microdroplet ensembles produced in devices with a nanochannel-microchannel interface. High-density monodisperse microdroplets (femtoliter oil-droplets) are shown to self-organize into 3D close-packed face-centered cubic (fcc) lattices, after being generated at the nanochannel-microchannel interface and flowing together with a continuous water phase in microfluidic channels. The 3D arrays presented in this work could provide platforms for many potential applications.

Finally, overall conclusions are drawn, and recommendations and possible future developments are discussed in chapter 10.

Since most of the chapters are based on manuscripts or published articles, information is repeated more often throughout this thesis, especially in the introductions. This was done to offer a good readability of chapters separately.

References

- [1] A. van den Berg, T. S. J. Lammerink, *Micro total analysis systems: Microfluidic aspects, integration concept and applications*, Vol. 194, Springer-Verlag, Berlin, Berlin 33 **1998**.
- [2] A. S. Utada, E. Lorenceau, D. R. Link, et al., *Science* **2005**, 308, 537.
- [3] M. Joanicot, A. Ajdari, *Science* **2005**, 309, 887.
- [4] T. Kawakatsu, G. Tragardh, C. Tragardh, et al., *Colloid Surface A* **2001**, 179, 29.
- [5] I. G. Loscertales, A. Barrero, I. Guerrero, et al., *Science* **2002**, 295, 1695.
- [6] J. D. Tice, H. Song, A. D. Lyon, et al., *Langmuir* **2003**, 19, 9127.

-
- [7] B. Zheng, J. D. Tice, R. F. Ismagilov, *Anal. Chem.* **2004**, 76, 4977.
- [8] H. Hisamoto, T. Saito, M. Tokeshi, et al., *Chem. Commun.* **2001**, 2662.
- [9] M. W. Losey, R. J. Jackman, S. L. Firebaugh, et al., *J. Microelectromech. Syst.* **2002**, 11, 709.
- [10] B. Zheng, R. F. Ismagilov, *Angew. Chem. Int. Ed.* **2005**, 44, 2520.

Chapter 2

Multiphase Flow in Micro- and Nanochannels - Pumping Methods

Fluids that are of interest in nature, biotechnology and chemistry are rarely either simple single-phase or non-confined (open system) fluids. It is therefore not surprising that recently a surge of interest has arisen in multiphase confined fluid manipulation. This chapter aims at reviewing investigations into complex multiphase micro- and nanochannel flows. In the first part, the pumping principles for this type of flow will be discussed. These should be chosen carefully according to two factors: scaling behavior at the micro- and nanoscale and adaptability to multiphase coexistence in the same channel. Subsequently, multiphase fluid flow behavior in micro- and nanochannels is treated, which differs a lot from that in single-phase and non-confined fluidic systems. This behavior will include flow patterns, flow profiles, film flow, corner flow, and slip flow.

Modified from

L. Shui, J. C. T. Eijkel and A. van den Berg, *Encyclopedia of Microfluidics and Nanofluidics*, 3, 1736-1743 (2008). ISBN: 978-0-387-32468-5(Print), 978-0-387-48998-8(Online).

L. Shui, J. C. T. Eijkel and A. van den Berg, *Sensors and Actuators B*, 121: 263-276, (2007).

2.1 Introduction

In the past 15 years, the use of sensors and actuators has been significantly extended with their incorporation in Micro Total Analysis Systems (μ TAS) or Lab-on-a-Chip devices (LOC) [1, 2]. Essential for this has been the rapid development of the field of microfluidics, and recently nanofluidics, areas that have received enormous attention because of the availability of methods for fabricating complicated flow configurations [3-7] and measuring transport phenomena [8] at the micro- and nanoscale. In LOC systems, sensors or detectors are usually combined with micro- or nanofluidic channels, pumps, mixers, separators and valves to provide much better functionality. Ideally, each process – e.g. sampling, sample pretreatment, reaction, separation, detection and analysis in an analytical system – is hereby realized on an integrated device. In these processes, fluid manipulation should be necessarily a well-known part of the LOC and μ TAS. The fluids of interest in chemistry and biotechnology are rarely simple single-phase liquids [9]. In addition, there is a rapidly growing interest in gas-water and oil-water multiphase systems for high-throughput chemical synthesis [10, 11]. For this reason we will review the use and future potential of multiphase flows for LOC systems.

Complex fluids still require detailed study and interpretation. Multiphase non-confined systems – having one free surface – have recently been studied and reviewed [9, 12, 13]. However, most of fluid transport, compartmental chemistry, interfacial phenomena and applications employ multiphase confined systems. These channel confined and multiphase complex fluidic systems provide complicated but practical tools. Recently, fluid flows in closed systems have been partially discussed in some reviews according to modeling studies [14, 15], dimensionless number analysis [16], flow engineering [13] and applications: heat transfer [17], microreactor [18], mixer [19] and DNA analysis [20]. In this chapter, we focus on multiphase fluid flow in micro- and nanochannels by discussing pumping principles and flow behavior.

Compared to single-phase flow systems or non-confined systems, when discussing multiphase flow in micro- and nanochannels there are many questions that arise even in a simple configuration. Both advantages and disadvantages originate from

the confinement in a channel, the reduction in dimension and the coexistence of multiple phases. Manipulating fluids in such a system is much more complicated than in non-confined or single-phase systems. The flow of fluids within enclosed channels of glass, silicon, or plastic can be actuated spontaneously, non-mechanically or mechanically. As the hydrodynamic resistance increases due to the confinement in channels, the most frequently used pumping method – syringe pumping – is increasingly difficult to use in nanochannels due to the reduction in dimension. The best pumping principle for single-phase channel-flow, named as electro-osmotic flow, can not easily be used for driving because of the coexistence of multiple phases. Some actuation forces however, for example interfacial forces, are more useful in multiphase micro- or nanochannel flow. Clearly, therefore, the pumping principle has to be chosen carefully before designing.

When different phases are injected as adjacent streams in one channel, one phase often preferentially wets the boundaries and encapsulates the second fluid as discrete droplets [21-24]. However, the flow can also become stable by the generation of a clear interface [6]. With downscaling, the gravitational force becomes less important [25]. Multiphase-fluid dynamical responses are commonly successfully characterized by using some dimensionless numbers used in single-phase flows, for example the Reynolds number (Re) and the capillary number (Ca) [13]. Depending on wetting properties, flow velocities, fluid viscosity and geometrical features, the flow patterns in multiphase channel flow change between segmented flow and stratified flow. A segmented flow uses discrete volumes of fluids, whereas a stratified flow relies on fluids which are continuously introduced into the system to form stable interfaces. Both the individual fluid phases and the interfaces between immiscible fluids provide useful tools for different applications – emulsification, encapsulation, microreaction, template synthesis, mixing, extraction, separation, bioassay and kinetic studies. At the same time several flow phenomena, for instance film flow, corner flow and slip flow, play increasingly important roles in with reduction of the dimensions.

In this chapter, actuation forces are discussed in the first section. Potential pumping principles, related important experimental parameters, and scaling behavior

are presented. Multiphase flow behavior in micro- and nanochannels, and its determinative factors are described in the second section.

2.2 Actuation Forces

Fluid is defined as a continuous, amorphous substance whose molecules move freely past one another and which has the tendency to assume the shape of its container; a liquid or gas. Phase is a distinct state of matter in a system; matter that is identical in chemical composition and physical state and separated from other material by the phase boundary. Multiphase fluids are those in which there exist at least two immiscible fluids in one system with different chemical compositions – liquid/liquid, or with different physical states – gas/liquid. The motion of a fluid in a channel can be driven by internal forces which are determined by fluid and channel properties, such as interfacial forces, or by an external field e.g. a gravitational, electrical, magnetic, thermal, photic or phonic field. Table 2.1 lists the force-related dimensionless numbers. In the micro- and nanoareas, the relative importance of forces is given by the following order: buoyancy < inertial force \approx gravitation < viscous force \ll interfacial force. Interfacial forces therefore become prominent upon system downscaling.

Fluid flow in channels of constant cross-sectional shape can be described by Poiseuille's law [26, 27]:

$$Q = \int v_i dA \approx \frac{\Delta P}{R_{hy}} \quad (2.1)$$

where Q ($\text{m}^3 \cdot \text{s}^{-1}$) is the volume flow rate, v_i is the flow velocity ($\text{m} \cdot \text{s}^{-1}$) at the position i (v_i is constant in a flat flow, $v_{\text{effective}} \approx 0.5v_{\text{max}}$ in a parabolic flow), A (m^2) is the area of cross section, ΔP (Pa) is the pressure difference between two ends of the channel, R_{hy} ($\text{kg} \cdot \text{s}^{-1} \cdot \text{m}^{-4}$) is the hydrodynamic resistance which can be approximately expressed as:

$$R_{hy} \approx \eta L C^2 A^{-3} \quad (2.2)$$

where η (Pa.s) is the fluid viscosity, L (m) is the channel length, and C (m) is the

perimeter of the cross section. The scaling of flow velocity for different pumping principles is shown in Table 2.2. We divide pumping principles into three categories – self-pumping, non-mechanical pumping and mechanical pumping.

Table 2.1 Important dimensionless numbers in multiphase flows

Dimensionless numbers	Definition	Equations	Scaling	Values*
Grashof	$\frac{\text{Buoyancy}}{\text{Viscous}}$	$\frac{d^3 \rho^2 g \beta \Delta T}{\eta^2}$	3	10^{-10}
Bond	$\frac{\text{Gravitational}}{\text{Interfacial}}$	$\frac{d^2 \rho g}{\sigma}$	2	10^{-9}
Reynolds	$\frac{\text{Inertial}}{\text{Viscous}}$	$\frac{d \rho v}{\eta}$	1	10^{-4}
Capillary	$\frac{\text{Viscous}}{\text{Interfacial}}$	$\frac{\eta v}{\sigma}$	0	10^{-5}
Mach	$\frac{\text{Inertial}}{\text{Elastic}}$	$\frac{v}{a}$	0	-
Kn	$\frac{\text{Free path}}{\text{Flow dimension}}$	$\frac{\lambda}{d}$	-1	-

d – channel dimension, ρ – fluid density, g – gravity acceleration constant, β – coefficient of expansion, ΔT – temperature difference, η – fluid viscosity, σ – interfacial force, v – flow velocity, a – sound speed, λ – mean free path (the average distance travelled by molecules between collisions).

*For a water-oxygen two-phase flow: $T = 20^\circ$, $\eta(O_2) = 20.317 \times 10^{-6}$ Pa.s, $\eta(H_2O) = 1.025 \times 10^{-3}$ Pa.s, $\sigma(H_2O) = 72.8$ mN.m⁻¹, $\rho(H_2O) = 10^3$ kg.m⁻³, $\rho(O_2) = 1.429$ kg.m⁻³, $\theta(\text{water and glass}) \approx 50^\circ$, $\beta(\text{water at } 20^\circ\text{C}) = 0.00021^\circ\text{C}^{-1}$ assuming that $d = 100$ nm and $v = 1$ mm.s⁻¹.

Table 2.2 Pumping methods

	Forces	Pumping	Velocity scaling	Downscaling	Advantages	Disadvantages	References
Non-mechanical pumping	Electrostatic	Electrokinetic	0	-	Scalability High pump pressure	Continuum of conductivity required High applied voltage	[33-37]
	Ion drag Molecular drag	Electro hydrodynamic	2	-	Availability for non-conducting fluids	Continuum of conductivity required	[38-40]
	Lorenz	Magneto hydrodynamic	2	-	Versatile directions Fast response	Continuum of conductivity required Both electric and magnetic field needed	[41-44]
	Interfacial	Electrocapillary	1	++	Scalability Integratability	Contact angle saturation	[45-49,60]
		Thermocapillary	1	++	Scalability Integratability	Fluidic boiling & freezing point limits High power consumption	[29,51]
		Optocapillary	1	++	Scalability Integratability	Photosensitive material required	[52]
		Solutocapillary	1	++	Scalability Integratability Spontaneous flow	Uncontrollability	[53]
Vapor pressure gradient	Evaporation	2	/	Biomimetic Simple design	Large evaporation area High temperature	[54]	
Chemical potential gradient	Osmotic	2	/	Simple design	Slow equilibrate process	[55]	
Mechanical pumping	Pressure gradient	Syringe	2	+	Versatility	Unfavorable scaling	[80,81]
	Mechanical deformation	Diaphragm	2	+	High actuation force Fast response	High applied voltage Complicated mounting procedure	[82-84]
	Centrifugal	Centrifugal	2	+	Controllable rotation Broad flow velocity	Uni-direction Affected by fluidic density	[87-89]
	Viscous	Shear	2	+	Direct Simple design	Difficult fabrication	[90]
	Oscillating	Acoustic	2	+	No contact between actuator and fluids	Low pump pressure	[92-95]
	Gas pressure gradient	Bubble	2	+	Low power consumption	Long response time	[97]

2.2.1 Self-pumping

A contact angle is set up when a liquid droplet contacts both a solid and a gas (or a solid and a second immiscible liquid) (Fig. 2.1A). The liquid curvature is caused by the differences among interfacial tensions. The force balance is described by Young's equation:

$$\sigma_{sg} = \sigma_{sl} + \sigma_{lg} \cos\theta \quad (2.3)$$

where σ ($\text{N}\cdot\text{m}^{-1}$) indicates the interfacial tension between two phases, the subscripts g, l, s represent gas, liquid and solid, respectively, and θ (degree) is the contact angle. Therefore, in a hydrophilic channel, concave and convex interfaces are created upon filling in with hydrophilic and hydrophobic fluids, respectively (Fig. 2.1B).

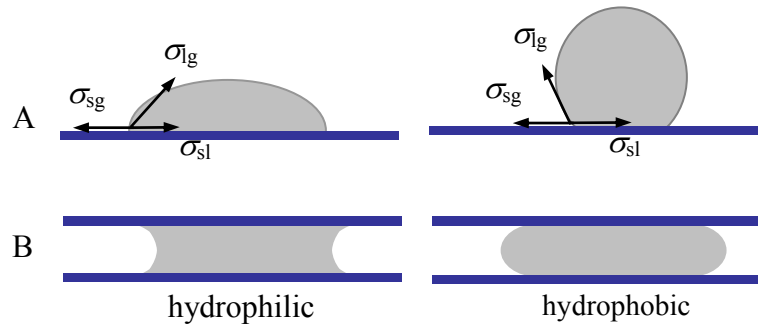


Figure 2.1 Wettability (A) on free surfaces, (B) in channels.

Self-propelling slugs [28] can be realized by careful design, material selection, microfabrication, surface control, and processing. A hydrophilic liquid, water for instance, “pulls” itself into or through a hydrophilic micro- or nanochannel by said capillary action. The capillarity induced pressure pulling the liquid along the channel is expressed by Young-Laplace's equation:

$$P_{cap} = G\sigma_{lg}\cos\theta/d \quad (2.4)$$

where G is a dimensionless geometrical constant which is 4 for a circle, 2 for a slit-like and $2(1+\text{height}/\text{width})$ for a square or rectangular cross section [29], and d (m) is the

characteristic diameter. Fluids, therefore, can be spontaneously propelled by a capillarity induced pressure gradient. In a channel, the motion of a fluid segment can result from capillarity-induced pressure difference between the front and the rear of the fluid column. Such a pressure difference (ΔP) is described by Young-Laplace's equation:

$$\Delta P = P_{\text{cap},1} - P_{\text{cap},2} = G\sigma_{\text{lg}} \left(\frac{\cos \theta_1}{d_1} - \frac{\cos \theta_2}{d_2} \right) \quad (2.5)$$

The pressure difference can thus be obtained by changing the channel diameter (d), the interfacial tension (σ) or the contact angle (θ). For example, a slug will move from the wide part to the narrow part when the channel diameter changes [30] (Fig. 2.2A). The movement can also be realized by using different channel materials [31] (Fig. 2.2B) or fluids [32] (Fig. 2.2C) with different interfacial energy. Similar phenomena happen for two or more juxtaposed phases [28] (Fig. 2.2D). In the flow direction, concave interfaces push fluids in the same direction but convex ones pull fluids to the opposite direction along the channels. The motion can even be inverted by juxtaposing a liquid of low surface tension [28].

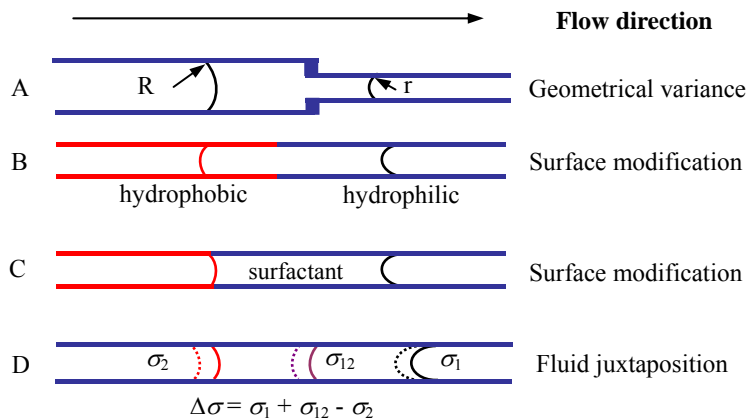


Figure 2.2 Self-propelling flow: (A) geometrical variance, (B) surface modification (solid), (C) surface modification (liquid), and (D) bi-slug (fluid juxtaposition).

2.2.2 Non-mechanical pumping methods

The previous section (2.2.1) considered forces generated by the system components. Here we will consider pumping by externally applied forces of non-mechanical origins. Non-mechanical pumps do not involve any mechanically moving parts. Examples are the electrokinetic pump (EK) [33-37], the electrohydrodynamic pump (EHD) [38-40], the magnetohydrodynamic pump (MHD) [41-44], the interfacial tension gradient-driven pump [29, 45-53], the evaporation-driven pump [54], or the osmotic pump [55].

EK pumping occurs when an applied electric field exerts a force on a non-electroneutral body of liquid [33-37, 56], e.g. a double layer, or when an applied electric field impulses a charged large particle [57, 58], which then will drag the fluid along. EHD pumps drag the fluid by ion drag [39, 59], induction [40] or polarization [38] forces. MHD pumps use Lorenz force acting on moving ions and being perpendicular to the both applied electric and magnetic fields [41-44].

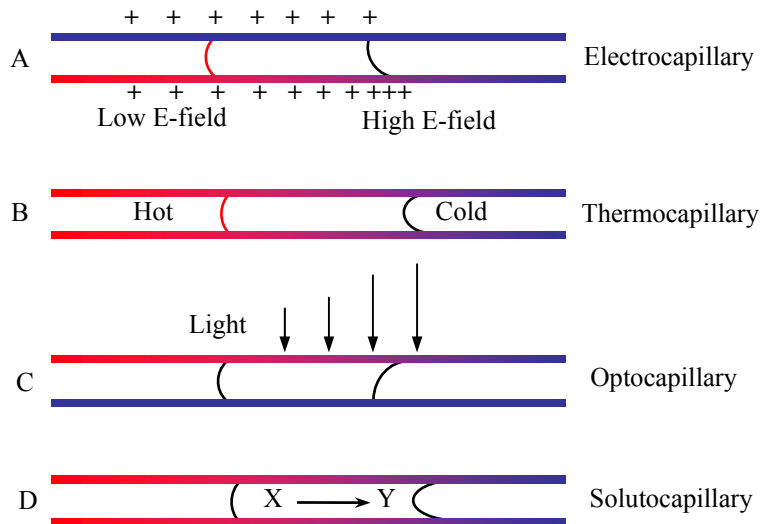


Figure 2.3 Interfacial tension gradient driven flow: (A) electrocapillary, (B) thermocapillary, (C) optocapillary, and (D) solutocapillary (X and Y are solutes with different wetting capability).

A gradient of interfacial tension along a channel also induces fluid movement, as discussed in the previous section. Here we will consider actuating such a gradient which can be done by electrocapillary (electrowetting) [45-49, 60] (Fig. 2.3A), thermocapillary (thermowetting) [29, 51] (Fig. 2.3B), optocapillary (light-driven) [52] (Fig. 2.3C), solutocapillary [53] (Fig. 2.3D) or some combination of these, as for example, optoelectrocapillary [50] pumping.

Table 2.2 lists these pumping principles. Electrocapillary actuation drives fluids by modifying solid-liquid interfacial tension. This method has been successfully applied to move droplets on free surfaces where it is also termed as “electrowetting”. Electrocapillary pumping has been realized either in a direct fashion whereby fluids are actuated by bare electrodes [61, 62], or an indirect fashion – electrowetting on dielectric (EWOD) – in which fluids contact a dielectric and can be actuated by electrodes embedded underneath the dielectric layer [46, 47, 63-69]. Thermocapillary action drives fluid motion by changing the liquid-gas or liquid-liquid interfacial tension by generating gradients in temperature. Optocapillary action can change interfacial tensions of solid-liquid, liquid-gas or liquid-liquid by using light to modify the interfacial energy of solids [52, 70-73]. Furthermore, the solid-liquid or liquid-gas interfacial tensions can be modified by the travelling solution itself, which is called solutocapillary action. Solutocapillary pumping can be realized by thermal [74], electrical [53, 75] or optical [76, 77] methods.

Two further pumping principles which have been recently applied to actuate fluidic flow in channels are evaporation [54] and osmosis [55]. All the actuation techniques mentioned above have already been used in the design of micropumps [78].

Comparing these actuation mechanisms as listed in Table 2.2, the best scaling behavior can be obtained with EK pumping where the flow velocity is not affected by downscaling. Keep in mind that the hydrodynamic resistance scales as $1/d^2$, a good scaling behavior is also shown by the interfacial tension gradient-induced pumping, where the flow velocity is proportional to the channel diameter. The scaling behavior of EHD, MHD, evaporation-driven pumping and osmotic pumping is unfavorable, as the flow velocity is a function of the square of the channel diameter.

With EK pumping, a high outlet pressure comparable to mechanical pumping can be obtained with a high applied voltage. EK however does not work if a continuously conducting fluid medium is interrupted by entrapment of gas bubbles or dielectric droplets [36]. EHD and MHD also present this drawback. Advantage of EHD and MHD actuations however is their straightforward reversibility. Therefore, these pumping principles will generally not fit for multiphase micro- and nanochannel flows. The pumping driven by an interfacial tension gradient is preferred for such applications. Firstly, more interfaces are produced by multiphase coexistence than by a single phase in a channel. This means that a summation of actuation forces on the sequence of plugs can be obtained. Secondly, scaling law is good in micro- and nanochannels.

Among the interfacial tension gradient-driven principles, electrocapillary pumping is the most versatile. Thermocapillary, optocapillary and solutocapillary actions are more or less strongly limited by material properties: thermocapillary pumping is restricted by the fluid freezing- and boiling-points, optocapillary pumping relies on the limited range of photosensitive materials, solutocapillary pumping totally depends on the surface-active-agents. Electrocapillary pumping can be manipulated by optimizing not only the dielectric-layer capacitance by changing the dielectric constant and the layer thickness, but also the available applied voltage [48]. Electrocapillary pumping also shows better scaling behavior than other interfacial force-based methods. Although the flow velocity is proportional to the channel diameter it is also a function of the square of the applied voltage. Furthermore, a versatile microfabrication strategy – integrating actuators to achieve local control of droplet motion by integrated electrode arrays – can be followed. In practice, multiphase fluids have thus been successfully manipulated by electrocapillary pumping [47, 64, 79].

2.2.3 Mechanical pumping methods

Mechanical pumps play an important role for fluid transport in micro- and nanofluidic systems. The pumping methods include syringe pumping, diaphragm pumping, centrifugal pumping, shear pumping, oscillation pumping and bubble pumping.

Hereby, syringe pumping [80, 81] remains the most useful method because of its flexibility, availability and controllability.

Diaphragm pumping [82-84] offers integration of the pumping method with the microfluidic device and is realized by mechanical deformation of channel walls by piezoelectric, magnetoelectric, electrostatic or pneumatic actuators. Among these actuators, piezoelectric actuation provides a high actuation force and a fast mechanical response, but needs a high actuation voltage and involves complicated mounting procedures. Magnetoelectric and electrostatic actuators can only supply low pressures. The pneumatic actuator can also generate high pressures but with long response time. Smart materials [85, 86], which swell or contract in response to different stimulations (electric field, light, temperature, solvent and pH) provide another attractive alternative.

Centrifugal pumping [87-89] manipulates fluids uni-directionally in a channel by applied motor rotation. Mostly, channel manifolds for centrifugally pumped systems are fabricated on a disc plate. The fluid density and position in the channel influence the flow. This characteristic can be used advantageously to separate, merge and mix fluids. However, it becomes disadvantageous for moving different fluids at the same velocity.

Due to the viscoelastic behavior of fluids and the interaction between fluids and channel walls, fluids are forced to move when the channel walls move [90] (Fig. 2.4). This so-called shear pumping is a direct and simple way to pump.

Oscillation pumping makes use of the drag forces induced by a mechanical wave [92-94] along the channel axis or the quartz wind [95] (named for the wind observed to blow away from oscillating quartz crystals) perpendicular to the channel axis. Its advantage is that there is no contact between fluids and actuator. Thereby, contamination is avoided. However, the outlet pressure generated by oscillation pumping remains very low.

In a channel, because of volume conservation, liquids experience a force if another entrapped fluid expands or shrinks. Thus, a bubble pump uses the volume change of gas bubbles to move liquid in a channel. Bubbles can be produced by thermal [96, 97] or electrolytic [98] means. Both can be realized by integrated

elements: microheaters or electrodes. The main drawback is that heating of the medium or electrochemical reactions cannot be avoided. Moreover, the thermal-bubble pump has a long response time.

The advantages of mechanical pumping are: high output pressure (except oscillation pumping), broad range of flow velocities, and insensitivity to the fluidic nature. Mechanical pumping can pump different fluids including liquid and gas. However, the flow velocities scale with the square of the channel diameter (Table 2.2), and a very high pressure has to be used in nanochannels. Except in the case of bubble pumping, it is also difficult to integrate mechanical pumps.

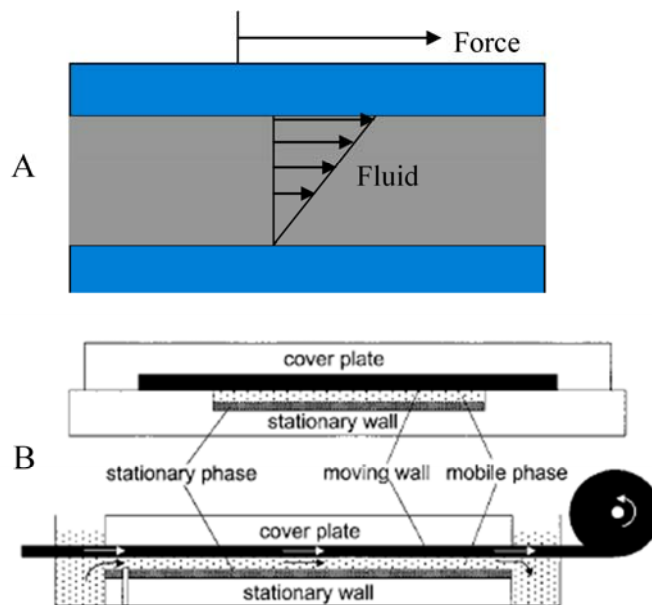


Figure 2.4 Shear flow: (A) schematic shear-driven flow, (B) radial cross section and longitudinal cross section of a basic design for a shear-driven chromatography apparatus. The dimensions of width, length, and thickness are not properly scaled. The white and black arrows, respectively, denote the movement of the movable wall and the mobile phase [91].

Summarizing the previous, we can conclude that from theoretical and practical points of view syringe pumping is a direct and versatile method which is suitable in broad fields including multiphase flow, though the scaling law does not favor its use in nanochannels; whereas electrocapillary action is the favorable method to actuate not only multiphase flow but also nanochannel flow since the actuation pressure increases with downscaling.

2.3 Flow Phenomena

It is important to understand the multiphase flow behavior in micro- or nanochannels that results from the pumping methods described before, since the generation of a stable flow of sample fluids is crucial for performing reliable flow applications [21, 85, 99-101]. For example, the size of synthesized particles and the size distribution change with flow patterns and profiles [102].

When discussing multiphase fluidic flows, the different behavior of liquid and gas must be stressed. The average distance between molecules in a gas is much greater than in a liquid. For example, 1 μm^3 contains 25 million molecules of air (298K, 1atm), but 34 billion molecules of water. The average distance between molecules in a gas phase is one order of magnitude higher than the diameter of its molecules, while it approaches the molecular diameter in a liquid phase. Therefore, gas molecules move ballistically and only rarely collide, whereas molecules in liquid are in constant collision. As a result, a liquid is usually incompressible, and a gas is compressible. The Mach number (Ma) is a dynamic measure of fluid compressibility, and is defined as the ratio of flow velocity (v) to sound speed (a):

$$Ma = v/a \quad (2.6)$$

Without locally changing fluid properties or boundary conditions, strong wall heating or cooling for instance, fluid flow can be treated as incompressible if the local Mach number is less than 0.3. Under such conditions – fluid density does not change

significantly while they flow through the system – the fluid dynamical response of a multiphase flow can be characterized successfully in terms of the dimensionless numbers for single-phase flows, such as the Reynolds number (Re) and the capillary number (Ca) [13].

The most common dimensionless number, the Reynolds number (Re), is a measure of the ratio of inertial to viscous forces, and is written as [103]:

$$Re = \frac{\rho v d}{\eta} \quad (2.7)$$

where ρ is the effective density ($\text{kg}\cdot\text{cm}^{-3}$), v is the average flow velocity ($\text{m}\cdot\text{s}^{-1}$), η is the effective viscosity ($\text{Pa}\cdot\text{s}$), and d is the characteristic flow dimension (m). In a straight channel, the value of $Re \approx 10^3$ is commonly accepted as a limit for the transition from a viscous ($Re < 10^3$) to turbulent flow [104]. In a typical channel with a diameter between 100 nm and 100 μm , where $\eta(\text{H}_2\text{O}) = 1.025 \times 10^{-3} \text{ Pa}\cdot\text{s}$, $\rho(\text{H}_2\text{O}) = 10^3 \text{ kg}\cdot\text{m}^{-3}$ and $v = 1 \text{ cm}\cdot\text{s}^{-1}$, Re lies between 1 and 10^3 . For a gas, such as oxygen $\eta(\text{O}_2) = 20.317 \times 10^{-6} \text{ Pa}\cdot\text{s}$ and $\rho(\text{O}_2) = 1.429 \text{ kg}\cdot\text{m}^{-3}$, Re ranges from 10^{-4} to 10^{-1} . Therefore, laminar flows are expected in micro- and nanochannels and not turbulent or random flows.

The capillary number (Ca) may be the most useful number to describe multiphase flow behavior in micro- and nanochannels [28, 101, 105-109], which is the ratio of viscous to interfacial forces and can be expressed as:

$$Ca = \frac{\eta v}{\sigma} \quad (2.8)$$

where η is the viscosity of the continuous phase ($\text{Pa}\cdot\text{s}$), v is the average flow velocity ($\text{m}\cdot\text{s}^{-1}$), and σ is the interfacial tension ($\text{N}\cdot\text{m}^{-1}$). We will use it extensively in the coming section to describe flow patterns in multiphase flow in micro- and nanochannels.

2.3.1 Flow patterns

The flow patterns found in multiphase fluidic systems are broadly categorized into segmented (droplet-based) flow and stratified (parallel) flow architectures. The basic channel configurations used to generate multiphase flows are T, Y or cross configurations (Fig. 2.5A). Gas-liquid two-phase flow patterns in microchannels have been studied in detail for heat-exchanger applications [110-119]. Between segmented flow and stratified flow patterns there can be several other flow patterns – bubbly, ring, lump, and annular flows (Fig. 2.5B) [112]. The flow of immiscible liquids in channels has been manipulated to study chemical phenomena and for biotechnology purposes [21, 22, 106, 120-127]. Flow dynamics depends on the capillary number and on fluid composition (Fig. 2.5C) [128].

In multiphase micro- and nanochannel flow systems a pair of competitive forces – the viscous force and the interfacial force – act dominantly. The viscous force acts tangentially to the interface by elongating it, whereas the interfacial force acts normally to the interface to induce the formation of droplets (minimizing the interfacial area) [22, 101]. Immiscible gas-liquid and liquid-liquid mixtures form segmented flow over a wide range of flow conditions and channel dimensions without additional control because of the high specific interfacial area [22]. Theoretically, a stable elongated interface between two phases occurs when viscous forces are greater than interfacial forces. The capillary number Ca presents the ratio of viscous to interfacial forces. Stable slug flow was obtained when $Ca = 0.0796$, and stratified flow was observed when $Ca \approx 1$ by adding 0.5% SDS [101]. Droplet deformation and free surface entrainment tubes can be induced when $Ca > 0.1$ [109]. Another typical example was demonstrated by Zheng et al (Fig. 2.5C) [128]. In this experiment, two streams of water were added to a carrier liquid in a cross junction. The two streams of water coalesced to form a big droplet-based flow at extremely small Ca (~ 0.0004). By increasing Ca , alternating droplet-based flow was generated with decreased droplet size. Finally, stratified flow was obtained for $Ca > 0.15$ at a water fraction of 0.2.

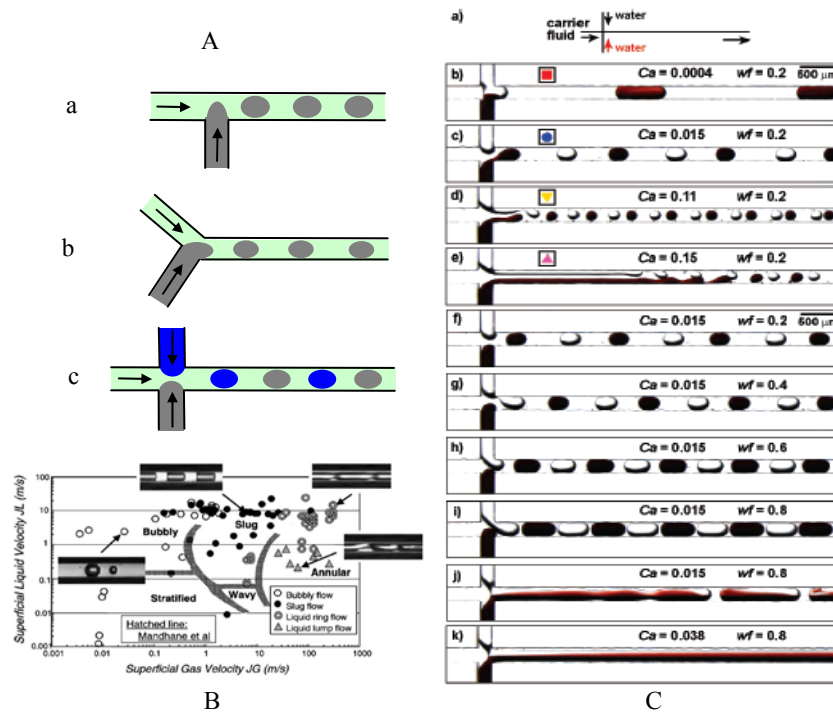


Figure 2.5 (A) Multiphase flow configurations: (a) T, (b) Y, and (c) Cross; (B) gas-liquid flow patterns [112] as functions of gas and liquid flow velocity; (C) liquid-liquid flow patterns [128] as functions of Ca (Capillary number) and wf (water fraction): (a) the microfluidic configuration, from (b) to (e) $Ca = 0.0004, 0.015, 0.11, 0.15, wf = 0.2$, from (f) to (j) $Ca = 0.015, wf = 0.2, 0.4, 0.6, 0.8, 0.8$, k) $Ca = 0.038, wf = 0.8$.

Whether a stable multiphase flow can be obtained in a fluidic system depends on both fluid dynamic conditions and surface chemistries. Based on the definition of the capillary number, the flow patterns in channels can be influenced by interfacial forces, fluidic viscosity, flow velocity and geometric features [19, 99, 102, 112]. The aim is to open the way to control the flow and to achieve versatility and reproducibility in on-chip flow management. The design will require smart network topologies and interplay of multiple physical and chemical effects.

2.3.2 Flow profiles

Fluid flow profiles can differ, depending on the driving forces, fluid properties and interactions between the fluids and channel walls. At low Re , an externally applied pressure and the wall friction generate a parabolic flow profile (pressure-driven flow), whereas electro-osmotic flow produces a flat flow profile [37] and shear-driven flow gives a linear velocity profile (Fig. 2.6). Real flow profiles are however more complex than these simple flow profiles. With downscaling, the electrostatic interactions between electrolyte fluids and charged walls become more important, which changes the flow profiles in nanochannels with respect to microchannels[129, 130]. Complex flow profiles may appear under different conditions.



Figure 2.6 Flow profiles: simple flow profile: EOF (Electro-Osmotic Flow), PDF (Pressure-Driven Flow) and SDF (Shear-Driven Flow).

2.3.3 Film flow and corner flow

Liquid segments can be interconnected through menisci in corners and thin liquid films on walls, which can cover around 5% of the microchannel cross section [102, 131, 132]. This percentage will increase with downscaling of the channel dimensions due to the decrease of fluid amount and the increase of specific interfacial areas. Therefore, film flow and corner flow will become more and more important on downscaling, for example in drying processes [133] and heat exchangers [134] in micro- and nanochannels.

2.3.3.1 Film flow

When droplet-based multiphase flow is considered, there are two possible configurations [13]. In the first, a drop forms a distinct contact line with the walls of

the channel. In the other, a droplet is separated from the boundaries by a thin wetting film. A stable thin liquid film between the tube wall and gas slugs can appear at high velocities on carefully treated clean surfaces [112, 115], and vice versa, so that thin films can be eliminated by surface modification of the channel walls by changing the wetting properties [106, 135].

When fluid slugs flow forward in a channel, the trail left by the previous slug act as a lubricant for the following one (Fig. 2.7). The film thickness is theoretically calculated as the ratio of the loss of the fluid volume to the surface area traveled by the fluid. The thickness of a lubricating film experimentally depends on viscosity of neighboring slugs, fluid velocities and surface properties [28, 112, 115, 132, 135-137].

Viscosity causes the deposition while capillary forces oppose the formation of a film. The film thickness (h_∞) deposited behind a wetting meniscus is therefore a function of Ca . At $10^{-5} < Ca < 10^{-2}$ it can be expressed by [28, 138]:

$$h_\infty = nRCa^{2/3} \quad (2.9)$$

where n is a pre-factor determined by fluid properties, and R is the channel radius. The greater the Ca , the larger the film thickness which allows more liquid flow through the film [136]. As a result, bubbles can be transported by liquid films with higher speeds [136, 139]. Systematical studies of film flow have been made by Churaev and coworkers [140, 141]. A film thickness of several nanometers was obtained in different systems.

Not only do liquid films lubricate hydrophilic surfaces, but also gas films form on non-wetting surfaces lubricating them. Because of the affinity of fluids and surfaces, hydrophilic fluids prefer to flow along hydrophilic channel surfaces, and hydrophobic fluids like to flow along hydrophobic surfaces [79, 99]. As hydrophilic liquids are imbibed by capillary force, hydrophobic gasses flow into hydrophobic channels much more easily. Peulon et al [142] found the liquid introduction sequence influenced the formation of stable interfaces. Thus, nanobubbles were found to exist on hydrophobic surfaces [143, 144]. The nanobubble layer may serve as a lubricant and decrease friction, which will also be one of the sources for a slip flow (section 2.3.4).

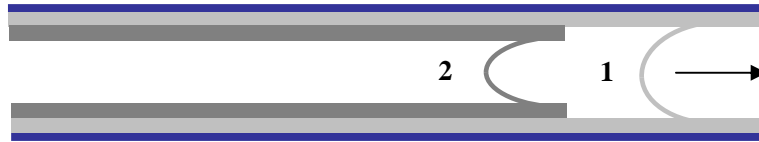


Figure 2.7 Liquid film as a lubricant: 1 and 2 are immiscible fluids.

2.3.3.2 Corner flow

Most of the channels fabricated at the micro- or nanoscale possess rectangular cross sections. To satisfy the contact angle wetting condition the fluid will curve along the perimeter of the interface [146] by minimizing interfacial areas, thus achieving a lower energy state (Fig. 2.8) [99]. The polymorphism of the wetting liquid depends on two parameters: the channel geometry, and the interaction between substrate materials and liquids [146, 147]. Weislogel et al [146] described capillary flow in corners. Their conclusions are that corner flow velocity is influenced by a flow resistance coefficient and geometric factors: the corner half-angle (α) and the contact angle (θ). Computed results showed that the spreading rate in the corner is maximized when $\theta = 0$, $\alpha \approx 17^\circ$ for constant flow rate and constant volume problems; and $\theta = 0$, $\alpha \approx 30^\circ$ for the constant height and exponential flow rate solutions. As the number of the polygon sides decreases [131, 132] and the corners sharpen [133], the cross-sectional area of fluids held in corners increases, and corner flows become more important.

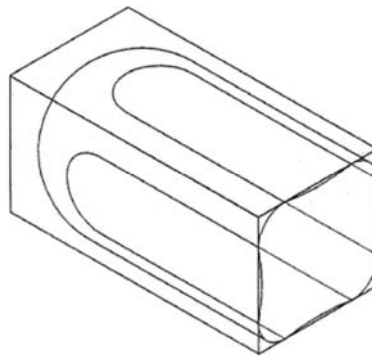


Figure 2.8 Corner flow in a channel with a rectangular cross section [145].

2.3.4 Slip flow

Traditional “non-slip” assumptions have been doubted for a long time in microfluidic systems. Recently, the results from molecular dynamics simulations and experiments at the micro- and nanoscale strongly indicated the existence of a slip flow. The amount of slip is described as slip length which is the notional distance inside the surface at which the velocity equals to zero (Fig. 2.9) [148]. Molecular dynamics (MD) simulations show that slip can occur only when a critical surface shear stress is reached [148], and that there exists a general relationship (linear or nonlinear given by different results) between the slip length and the local shear rate at a solid surface [149]. Slip length depends on the interactional parameters between solid and fluid: shear stress [148, 149], wetting properties [91], fluid properties (e.g. viscosity and density) [149] and interfacial roughness [91].

Significant slip was experimentally found by driving different fluids through micro- and nanochannels [150]. Shear-dependent boundary slip has been demonstrated experimentally [151-153]. No-slip boundary condition changed to partial slip when shear stress exceeded a critical level. The degree of slip changed with the fluid viscosity and the surface wettability (the fundamental conclusion is that slip boundary in aqueous systems is favored by hydrophobic surfaces). Slip length is also influenced by surface roughness. Consistent with MD simulations, slip length decreased by increasing surface roughness by adsorption of chemicals [154, 155]. However, a contrasting result was obtained in another experiment that boundary slip was seen to increase with surface roughness in a completely wetting system by measuring hydrodynamic drainage force, where the roughness features were obtained by etching the solid surface [156]. The difference may be that they altered the slip behavior in different manners [156].

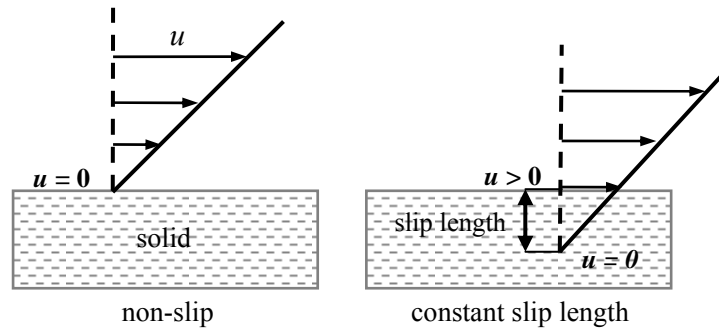


Figure 2.9 Non-slip and slip boundary flow: in both cases the velocity of the moving fluid (horizontal lines with arrows) extrapolates to zero. For non-slip, this occurs at the solid wall, but for slip flow, it occurs at a notional distance inside the wall and is finite where it crosses the wall [148].

Boundary conditions also changed when liquid was saturated with different gases [152, 155, 157, 158]. Segregation of gas to the near-surface region seems to facilitate some kind of low-density surface excitations [159], providing a zero shear stress boundary condition [160]. As discussed in the previous section (2.3.3), not only liquid films establish between a gas and solid surface but also gas bubbles or films can exist between a liquid and solid surface. Different fluids have different friction with solid surfaces, and fluid/fluid intermolecular interactions are stronger than those of fluid/solid surfaces. Therefore, in multiphase flow, boundary conditions are much more complicated. As diagnostic techniques improve our ability to probe the fluid surface at the molecular scale, it is expected that slip flow can be investigated by direct measurement of the fluid velocity [154] or the movement of the contact line.

The slip boundary condition will depend on rational control of interfacial properties: ultra-smooth [152] and superhydrophobic [153] surfaces or low viscosity [151] and density [149, 159] fluids.

2.4 Conclusions and Outlook

Multiphase micro- or nanochannel flow confines small volumes of several immiscible fluids in one device. Compared with single-phase or open systems, multiphase channel systems are more difficult to manipulate. However such systems are very useful since the immiscible fluids are separated from each other by flexible fluidic interfaces. The small-volume confinement and multiphase coexistence provide extra attractive characteristics.

In this chapter, we reviewed the actuation and manipulation methods of multiphase flow in micro- and nanochannels. It was shown that the actuation principles have to be chosen according to miniaturization and multiphase coexistence. For example, very high pressure is necessary for syringe pumping on downscaling to nanoscale, and EOF can not work efficiently when conductive fluids are interspaced with dielectric ones. Subsequently, alternative actuation methods need to be applied. At the nanoscale, the specific interfacial area in multiphase flow is very high and interfacial tension becomes prominent. Therefore, it is logical to use a gradient of interfacial tension to manipulate multiphase flow in nanochannels. Based on actuation principles and scaling behavior, electrocapillary pumping is a good choice. Furthermore, multiphase micro- and nanochannel flow phenomena are dramatically different from single-phase and open flow systems. The flow patterns, flow profiles, film flow, corner flow and slip flow are all complicated. Flow patterns vary between droplet-based flow and stratified flow depending on the capillary number. Flow profiles depend on actuation principles and channel sizes. Film flow, corner flow and slip flow become more and more important on downscaling, and special attention has to be paid to these phenomena in multiphase micro- and nanochannel flows.

The purpose of LOC is to miniaturize and integrate different flow components into complete multifunctional systems [161]. From design to application, there are many points which need input of knowledge from different scientific and engineering fields. This is therefore a strongly multidisciplinary field. With the participation of chemistry, physics, biology and medical science, the integration of LOC has been

successfully realized [4, 5, 19, 161-165]. Multiphase fluidic design and operation involve complex interactions of several physicochemical phenomena, including fluidic hydrodynamics, transport phenomena and surface characteristics. Successful design, control and application of multiphase fluidic systems require a thorough understanding of the interactions of physicochemical properties on different spatial and temporal scales in each phase and between phases.

References

- [1] A. van den Berg, T. S. J. Lammerink, *Micro total analysis systems: Microfluidic aspects, integration concept and applications*, Vol. 194, Springer-Verlag, Berlin, 33, **1998**.
- [2] A. Manz, N. Graber, H. M. Widmer, *Sens. Actuator B, Chem.* **1990**, *1*, 244.
- [3] D. Mijatovic, J. C. T. Eijkel, A. van den Berg, *Lab Chip* **2005**, *5*, 492.
- [4] S. Quake, *Trac-Trends Anal. Chem.* **2002**, *21*, XII.
- [5] T. Thorsen, S. J. Maerkl, S. R. Quake, *Science* **2002**, *298*, 580.
- [6] H. Hisamoto, T. Saito, M. Tokeshi, et al., *Chem. Commun.* **2001**, 2662.
- [7] Y. Kikutani, H. Hisamoto, M. Tokeshi, et al., *Lab Chip* **2004**, *4*, 328.
- [8] D. Sinton, *Microfluid. Nanofluid.* **2004**, *1*, 2.
- [9] T. Pföhl, F. Mugele, R. Seemann, et al., *ChemPhysChem* **2003**, *4*, 1291.
- [10] C. C. Lee, G. D. Sui, A. Elizarov, et al., *Science* **2005**, *310*, 1793.
- [11] I. Shestopalov, J. D. Tice, R. F. Ismagilov, *Lab Chip* **2004**, *4*, 316.
- [12] A. A. Darhuber, S. M. Troian, *Annu. Rev. Fluid Mech.* **2005**, *37*, 425.
- [13] H. A. Stone, A. D. Stroock, A. Ajdari, *Annu. Rev. Fluid Mech.* **2004**, *36*, 381.
- [14] M. Tatineni, X. Zhongt, *American Institute of Aeronautics and Astronautics* **2004**, 11712.
- [15] M. De Menech, *Materials Research Society Symposium - Proceedings* **2003**, *790*, 263.
- [16] T. M. Squires, S. R. Quake, *Rev. Mod. Phys.* **2005**, *77*, 977.
- [17] O. N. Kaban'kov, A. P. Sevast'yanov, *Heat Transfer Res.* **2000**, *31*, 103.
- [18] G. N. Doku, W. Verboom, D. N. Reinhoudt, et al., *Tetrahedron* **2005**, *61*, 2733.
- [19] M. W. Losey, R. J. Jackman, S. L. Firebaugh, et al., *J. Microelectromech. Syst.* **2002**, *11*, 709.
- [20] J. O. Tegenfeldt, C. Prinz, H. Cao, et al., *Anal. Bioanal. Chem* **2004**, *378*, 1678.
- [21] A. S. Utada, E. Lorenceau, D. R. Link, et al., *Science* **2005**, *308*, 537.
- [22] M. Joanicot, A. Ajdari, *Science* **2005**, *309*, 887.
- [23] T. Kawakatsu, G. Tragardh, C. Tragardh, et al., *Colloid Surface A* **2001**, *179*, 29.
- [24] I. G. Loscertales, A. Barrero, I. Guerrero, et al., *Science* **2002**, *295*, 1695.
- [25] J. C. T. Eijkel, A. van den Berg, *Microfluid. Nanofluid.* **2005**, *1*, 249.
- [26] P. Gravesen, J. Branebjerg, O. S. Jensen, *J. Micromech. Microeng.* **1993**, *3*, 168.
- [27] O. C. Jones Jr, F. Kreith, F. M. White, *J. Fluid Eng.-T. ASME* **1981**, *103*, 509.
- [28] J. Bico, D. Quere, *J. Fluid Mech.* **2002**, *467*, 101.
- [29] T. S. Sammarco, M. A. Burns, *Aiche J.* **1999**, *45*, 350.
- [30] K. A. Polzin, E. Y. Choueiri, *J. Phys. D-Appl. Phys.* **2003**, *36*, 3156.

- [31] M. M. Weislogel, *Aiche J.* **1997**, *43*, 645.
- [32] C. D. Bain, G. D. Burnett-Hall, R. R. Montgomerie, *Nature* **1994**, *372*, 414.
- [33] A. P. Vincent Studer, Yong Chen, Armand Ajdari, *Analyst* **2004**, *129*, 944.
- [34] R. Qiao, N. R. Aluru, *Appl. Phys. Lett.* **2005**, *86*, 1431051.
- [35] S. Debesset, Eijkel, J. C. T. Manz, A., Hayden, C. J., Dalton, C., *Lab Chip* **2004**, *4*, 396.
- [36] P. Selvaganapathy, Y. S. L. Ki, P. Renaud, et al., *J. Microelectromech. Syst.* **2002**, *11*, 448.
- [37] J. Y. Min, E. F. Hasselbrink, S. J. Kim, *Sens. Actuator B, Chem.* **2004**, *98*, 368.
- [38] J. Darabi, M. M. Ohadi, D. DeVoe, *J. Microelectromech. Syst.* **2001**, *10*, 98.
- [39] J. Darabi, M. Rada, M. Ohadi, et al., *J. Microelectromech. Syst.* **2002**, *11*, 684.
- [40] C. Tsouris, C. T. Culbertson, D. W. DePaoli, et al., *Aiche J.* **2003**, *49*, 2181.
- [41] J. C. T. Eijkel, C. Dalton, C. J. Hayden, et al., *Sens. Actuator B, Chem.* **2003**, *92*, 215.
- [42] J. S. Jang, S. S. Lee, *Sens. Actuator A, Phys.* **2000**, *80*, 84.
- [43] S. Koster, E. Verpoorte, A. Homsy, et al., *Lab Chip* **2005**, *5*, 466.
- [44] A. V. Lemoff, A. P. Lee, *Sens. Actuator B, Chem.* **2000**, *63*, 178.
- [45] M. W. J. Prins, W. J. J. Welters, J. W. Weekamp, *Science* **2001**, *291*, 277.
- [46] J. Lee, H. Moon, J. Fowler, et al., *Sens. Actuator A, Phys.* **2002**, *95*, 259.
- [47] M. G. Pollack, A. D. Shenderov, R. B. Fair, *Lab Chip* **2002**, *2*, 96.
- [48] H. Moon, S. K. Cho, R. L. Garrell, et al., *J. Appl. Phys.* **2002**, *92*, 4080.
- [49] W. J. J. Welters, L. G. J. Fokkink, *Langmuir* **1998**, *14*, 1535.
- [50] P. Y. Chiou, H. Moon, H. Toshiyoshi, et al., *Sens. Actuator A, Phys.* **2003**, *104*, 222.
- [51] T. S. Sammarco, M. A. Burns, *J. Micromech. Microeng.* **2000**, *10*, 42.
- [52] K. Ichimura, S. K. Oh, M. Nakagawa, *Science* **2000**, *288*, 1624.
- [53] B. S. Gallardo, V. K. Gupta, F. D. Eagerton, et al., *Science* **1999**, *283*, 57.
- [54] N. Goedecke, J. Eijkel, A. Manz, *Lab Chip* **2002**, *2*, 219.
- [55] Y. C. Su, L. Lin, *J. Microelectromech. Syst.* **2004**, *13*, 75.
- [56] D. Lastochkin, R. H. Zhou, P. Wang, et al., *J. Appl. Phys.* **2004**, *96*, 1730.
- [57] T. Schnelle, G. Gradl, S. G. Shirley, et al., *Electrophoresis* **2000**, *21*, 66.
- [58] D. S. Reichmuth, G. S. Chirica, B. J. Kirby, *Sens. Actuator B, Chem.* **2003**, *92*, 37.
- [59] S. H. Ahn, Y. K. Kim, *Sens. Actuator A, Phys.* **1998**, *70*, 1.
- [60] C. J. Kim, *American Society of Mechanical Engineers, Heat Transfer Division, (Publication) HTD* **2001**, *369*, 55.
- [61] W. Satoh, M. Loughran, H. Suzuki, *J. Appl. Phys.* **2004**, *96*, 835.
- [62] W. Satoh, H. Hosono, H. Suzuki, *Anal. Chem.* **2005**, *77*, 6857.
- [63] K. L. Wang, T. B. Jones, *Langmuir* **2005**, *21*, 4211.
- [64] F. Mugele, A. Klingner, J. Buehrle, et al., *J. Phys.-Condens. Mat.* **2005**, *17*, S559.
- [65] M. G. Pollack, R. B. Fair, A. D. Shenderov, *Appl. Phys. Lett.* **2000**, *77*, 1725.
- [66] P. Paik, V. K. Pamula, M. G. Pollack, et al., *Lab Chip* **2003**, *3*, 28.
- [67] A. R. Wheeler, H. Moon, C. J. Kim, et al., *Anal. Chem.* **2004**, *76*, 4833.
- [68] K. Hoshino, S. Triteyaprasert, K. Matsumoto, et al., *Sens. Actuator A, Phys.* **2004**, *114*, 473.
- [69] J. Y. Cheng, L. C. Hsiung, *Biomed. Microdevices* **2004**, *6*, 341.
- [70] L. M. Siewierski, W. J. Brittain, S. Petrash, et al., *Langmuir* **1996**, *12*, 5838.
- [71] C. L. Feng, Y. J. Zhang, J. Jin, et al., *Langmuir* **2001**, *17*, 4593.
- [72] S. Abbott, J. Ralston, G. Reynolds, et al., *Langmuir* **1999**, *15*, 8923.
- [73] M. O. Wolf, M. A. Fox, *J. Am. Chem. Soc.* **1995**, *117*, 1845.
- [74] C. Maldarelli, http://mured.nasaprs.com/report/rt_reports/2001/FAR_CUNY_Maldarelli_Rpt.pdf.
- [75] D. E. Bennett, B. S. Gallardo, N. L. Abbott, *J. Am. Chem. Soc.* **1996**, *118*, 6499.

- [76] J. Y. Shin, N. L. Abbott, *Langmuir* **1999**, *15*, 4404.
- [77] J. Eastoe, M. S. Dominguez, P. Wyatt, et al., *Langmuir* **2002**, *18*, 7837.
- [78] P. Woias, *Sens. Actuator A, Phys.* **2005**, *105*, 28.
- [79] D. Huh, A. H. Tkaczyk, J. H. Bahng, et al., *J. Am. Chem. Soc.* **2003**, *125*, 14678.
- [80] D. F. Capes, D. Herring, V. B. Sunderland, et al., *PDA J. Pharm. Sci. Tech.* **1996**, *50*, 40.
- [81] J. L. Carl, B. L. Erstad, J. E. Murphy, et al., *Am. J. Helath-Syst. Ph.* **1995**, *52*, 1428.
- [82] Y. L. Zhang, J. K. Wu, *Appl. Math. Mechan. (English Edition)* **2005**, *26*, 1026.
- [83] N. T. Nguyen, T. Q. Truong, *Sens. Actuator B, Chem.* **2004**, *97*, 137.
- [84] H. T. G. Van Lintel, F. C. M. Van De Pol, S. Bouwstra, *Sens. Actuators* **1988**, *15*, 153.
- [85] D. E. Smith, S. Chu, *Science* **1998**, *281*, 1335.
- [86] W. Zhan, G. H. Seong, R. M. Crooks, *Anal. Chem.* **2002**, *74*, 4647.
- [87] D. C. Duffy, H. L. Gillis, J. Lin, et al., *Anal. Chem.* **1999**, *71*, 4669.
- [88] A. Penrose, P. Myers, K. Bartle, et al., *Analyst* **2004**, *129*, 704.
- [89] J. V. Zoval, M. J. Madou, *Proc. IEEE* **2004**, *92*, 140.
- [90] G. Desmet, G. V. Baron, **2000**, *72*, 2160.
- [91] C. Cottin-Bizonne, J. L. Barrat, L. Bocquet, et al., *Nat. Mater.* **2003**, *2*, 237.
- [92] S. Daniel, M. K. Chaudhury, P. G. de Gennes, *Langmuir* **2005**, *21*, 4240.
- [93] S. Daniel, M. K. Chaudhury, *Langmuir* **2002**, *18*, 3404.
- [94] R. M. Moroney, R. M. White, R. T. Howe, "Ultrasonically induced microtransport", presented at *IEEE Micro Electro Mechanical Systems Nara, Jpn.* **1991**.
- [95] J. C. Rife, M. I. Bell, J. S. Horwitz, et al., *Sens. Actuator A, Phys.* **2000**, *86*, 135.
- [96] L. W. Lin, A. P. Pisano, V. P. Carey, *J. Heat Transf.-Trans. ASME* **1998**, *120*, 735.
- [97] J. H. Tsai, L. W. Lin, *J. Microelectromech. Syst.* **2002**, *11*, 665.
- [98] D. Okeefe, C. Oherlihy, Y. Gross, et al., *Br. J. Anaesth.* **1994**, *73*, 843.
- [99] D. Huh, Y. C. Tung, H. H. Wei, et al., *Biomed. Microdevices* **2002**, *4*, 141.
- [100] A. Hibara, M. Nonaka, H. Hisamoto, et al., *Anal. Chem.* **2002**, *74*, 1724.
- [101] V. Reddy, J. D. Zahn, *J. Colloid Interface Sci.* **2005**, *286*, 158.
- [102] A. Gunther, S. A. Khan, M. Thalmann, et al., *Lab Chip* **2004**, *4*, 278.
- [103] C. E. Brennen, *Fundamentals of Multiphase Flows*, Vol. California Institute of Technology, Pasadena, California, Cambridge University Press, **2005**.
- [104] K. V. Sharp, R. J. Adrian, *Exp. Fluids* **2004**, *36*, 741.
- [105] D. Dendukuri, K. Tsoi, T. A. Hatton, et al., *Langmuir* **2005**, *21*, 2113.
- [106] M. Y. He, J. S. Edgar, G. D. M. Jeffries, et al., *Anal. Chem.* **2005**, *77*, 1539.
- [107] M. Muradoglu, H. A. Stone, *Phys. Fluids* **2005**, *17*, 1.
- [108] D. R. Link, S. L. Anna, D. A. Weitz, et al., *Phys. Rev. Lett.* **2004**, *92*.
- [109] S. T. Thoroddsen, Y. K. Tan, *Phys. Fluids* **2004**, *16*, L13.
- [110] F. G. T. J.J.Hwang, Chin Pan, *Int. J. Multiphas. Flow* **2005**, *31*, 548.
- [111] G. M. h. Vladimir S. Ajaev, *J. Colloid Interface Sci.* **2001**, *240*, 259.
- [112] A. Serizawa, Z. Feng, Z. Kawara, *Exp. Therm. Fluid Sci.* **2002**, *26*, 703.
- [113] L. A. E. L.P.Yarin, G.Hetsroni, *Int. J. Multiphas. Flow* **2002**, *28*, 1589.
- [114] Q. C. B. T.S.Zhao, *Int. J. Multiphas. Flow* **2001**, *27*, 765.
- [115] S. M. G. K.A.Triplett, S.I.Abdel-Khalik,A.LeMouel, B.N.McCoud, *Int. J. Multiphas. Flow* **1999**, *25*, 377.
- [116] S. M. G. K.A.Triplett, S.I.Abdel-Khalik,A.LeMouel, B.N.McCoud, *Int. J. Multiphas. Flow* **1999**, *25*, 395.
- [117] S. M. G T.L.Narrow, S.I.Abdel-KHALIK, D.L.Sadowski, *Int. J. Multiphas. Flow* **2000**, *26*, 1281.

- [118] Ruben Wedin, A. A. Dahlkild, *Ind. Eng. Chem. Res.* **2001**, *40*, 228.
- [119] L. P. Y. Y.P.Peles, G.Hensroni, *Int. J. Multiphas. Flow* **2000**, *26*, 1063.
- [120] V. Linder, S. K. Sia, G. M. Whitesides, *Anal. Chem.* **2005**, *77*, 64.
- [121] H. Z. Wang, H. Nakamura, M. Uehara, et al., *Chem. Commun.* **2002**, 1462.
- [122] J. Kobayashi, Y. Mori, K. Okamoto, et al., *Science* **2004**, *304*, 1305.
- [123] T. Tokimoto, S. Tsukahara, H. Watarai, *Langmuir* **2005**, *21*, 1299.
- [124] S. Sawada, M. Taguma, T. Kimoto, et al., *Anal. Chem.* **2002**, *74*, 1177.
- [125] B. H. Weigl, P. Yager, *Science* **1999**, 283, 346.
- [126] T. Maruyama, H. Matsushita, J. Uchida, et al., *Anal. Chem.* **2004**, *76*, 4495.
- [127] T. Maruyama, J. Uchida, T. Ohkawa, et al., *Lab Chip* **2003**, *3*, 308.
- [128] B. Zheng, J. D. Tice, R. F. Ismagilov, *Anal. Chem.* **2004**, *76*, 4977.
- [129] S. Pennathur, J. G. Santiago, *Anal. Chem.* **2005**, *77*, 6772.
- [130] S. Pennathur, J. G. Santiago, *Anal. Chem.* **2005**, *77*, 6782.
- [131] H. Wong, C. J. Radke, S. Morris, *J. Fluid Mech.* **1995**, *292*, 95.
- [132] H. Wong, C. J. Radke, S. Morris, *J. Fluid Mech.* **1995**, *292*, 71.
- [133] J. C. T. Eijkel, B. Dan, H. W. Reemeijer, et al., *Phys. Rev. Lett.* **2005**, *95*, 2561071.
- [134] F. J. Higuera, *Phys. Fluids* **2000**, *12*, 2186.
- [135] S. A. Khan, A. Gunther, M. A. Schmidt, et al., *Langmuir* **2004**, *20*, 8604.
- [136] A. Mazouchi, G. M. Homsy, *Phys. Fluids* **2000**, *12*, 542.
- [137] M. L. Gee, T. W. Healy, L. R. White, *J. Colloid Interface Sci.* **1990**, *140*, 450.
- [138] L. W. Schwartz, H. M. Princen, A. D. Kiss, *J. Fluid Mech.* **1986**, *172*, 259.
- [139] S. K. Wilson, *Phys. Fluids A* **1993**, *5*, 2064.
- [140] N. V. Churaev, *Adv. Colloid Interfac.* **2005**, *114-115*, 3.
- [141] N. V. Churaev, *Adv. Colloid Interfac.* **2003**, *103*, 197.
- [142] S. Peulon, V. Guillou, M. L'Her, *J. Electroanal. Chem.* **2001**, *514*, 94.
- [143] N. Ishida, T. Inoue, M. Miyahara, et al., *Langmuir* **2000**, *16*, 6377.
- [144] J. W. G. Tyrrell, P. Attard, *Langmuir* **2002**, *18*, 160.
- [145] A. Mazouchi, G. M. Homsy, *Phys. Fluids* **2001**, *13*, 1594.
- [146] M. M. Weislogel, S. Lichter, *J. Fluid Mech.* **1998**, *373*, 349.
- [147] M. Brinkmann, R. Lipowsky, *J. Appy. Phys.* **2002**, *92*, 4296.
- [148] H. Spikes, S. Granick, *Langmuir* **2003**, *19*, 5065.
- [149] P. A. Thompson, S. M. Troian, *Nature* **1997**, *389*, 360.
- [150] J. T. Cheng, N. Giordano, *Phys. Rev. E* **2002**, *65*, 0312061.
- [151] V. S. J. Craig, C. Neto, D. R. M. Williams, *Phys. Rev. Lett.* **2001**, *8705*, 0545041.
- [152] Y. X. Zhu, S. Granick, *Phys. Rev. Lett.* **2001**, *8709*, 0961051.
- [153] C. H. Choi, K. J. A. Westin, K. S. Breuer, *Phys. Fluids* **2003**, *15*, 2897.
- [154] R. Pit, H. Hervet, L. Léger, *Phys. Rev. Lett.* **2000**, *85*, 980.
- [155] Y. Zhu, S. Granick, *Langmuir* **2002**, *18*, 10058.
- [156] E. Bonaccorso, H. J. Butt, V. S. J. Craig, *Phys. Rev. Lett.* **2003**, *90*, 1445011.
- [157] Y. Zhu, S. Granick, *Phys. Rev. Lett.* **2002**, *88*, 1061021.
- [158] Y. X. Zhu, S. Granick, *Phys. Rev. Lett.* **2001**, *8709*, 0961041.
- [159] S. Granick, Y. Zhu, H. Lee, *Nat. Mater.* **2003**, *2*, 221.
- [160] E. Lauga, H. A. Stone, *J. Fluid Mech.* **2003**, *489*, 55.
- [161] J. A. Schwartz, J. V. Vykoukal, P. R. C. Gascoyne, *Lab Chip* **2004**, *4*, 11.
- [162] M. A. Burns, B. N. Johnson, S. N. Brahmaandra, et al., *Science* **1998**, *282*, 484.
- [163] R. F. Ismagilov, *Angew. Chem. Int. Ed.* **2003**, *42*, 4130.

- [164] R. G. Su, J. M. Lin, K. Uchiyama, et al., *Talanta* **2004**, *64*, 1024.
[165] J. Park, C.-S. Kim, Y. Kim, *Sens. Actuator B, Chem.* **2005**, *108*, 633.

Chapter 3

Multiphase Flow in Microfluidic Systems - Control and Applications of Droplets and Interfaces

Micro- and nanotechnology can provide us with many tools for the production, study and detection of colloidal and interfacial systems. In multiphase flow in micro- and nanochannels several immiscible fluids will be separated from each other by flexible fluidic interfaces. The multiphase coexistence and the small-volume confinement provide many attractive characteristics. Multiphase flow in microfluidic systems shows a complicated behavior but has many practical uses compared to a single-phase flow. In this chapter, we discuss the methods of controlling multiphase flow to generate either micro- or nano-droplets (or bubbles) or stable stratified interfaces between fluidic phases. Furthermore, applications of the droplets and interfaces in microchannels are summarized.

Modified from

L. Shui, S. Pennathur, J. C. T. Eijkel and A. van den Berg, *Lab on a Chip*, 8: 1010-1014 (2008).

L. Shui, J. C. T. Eijkel and A. van den Berg *Advances in Colloid and Interface Science*, 133: 35-49 (2007).

3.1 Introduction

Microfluidics is defined as the study and application of fluid flow on the microscale, and as such has long been part of the fluid mechanical component of colloid science [1], clinical chemistry [2], soil science [3], plant biology [4, 5], biomedical science [6] and so on. In the 1990s, the new research area of microengineered microfluidics emerged due to the appearance of microtechnology, and this field subsequently rapidly developed [7]. In the past decade, with the fast development of micro- and nanotechnology [8-14] research down to the micro- and nanoscale can be performed in very controllable and direct ways, and therefore, colloidal [15-22] and interfacial [23-27] phenomena in microsystems have received much attention recently. Ideally, micro- and nanotechnology can realize each process – e.g. sampling, sample pretreatment, reaction, separation, detection and analysis in an analytical system – on one integrated microdevice. Integrated systems of micro- and nanofluidic channels combined with pumps, valves, and detectors are known as “Lab-on-a-Chip” (LOC) or “Micro-total-analysis-system” (μ TAS) [7, 28].

The fluids of interest in chemistry and biotechnology are rarely simple single-phase liquids [29]. Complex fluidic systems, such as emulsions, play a very important role in drug delivery, food science, oil and dairy industries, and therefore require detailed study. Most of fluid transport, compartmental chemistry, interfacial phenomena and applications employ multiphase fluidic systems. Multiphase microfluidic systems are complicated but practical for applications. A multiphase micro- and nanofluidic system provides the possibilities to design and fabricate well-structured colloidal systems, and therefore, supplies us with enhanced opportunities to study colloidal and interfacial properties.

In this chapter, our focus will be on discussing multiphase microchannel flows based on flow control to generate stable droplets (droplet-based flow or segmental flow) and interfaces (stratified flow), and their applications.

Compared to a single-phase flow, the corresponding multiphase microfluidic flow is more complicated even in a simple configuration. The main characteristics

originate from the reduction in dimension, and the coexistence and confinement of multiple phases in one system.

When different phases are injected as adjacent streams in one channel, one phase often preferentially wets the boundaries and encapsulates the second fluid as discrete droplets due to the high interfacial forces at the microscale [17, 30-34]. However, a stable interface can also be generated between two phases by modifying forces on the channels and fluids [12, 34-36]. Depending on wetting properties, flow velocities, fluid viscosity and geometrical features, multiphase microfluidic flows change between droplet-based flows and stratified flows. The microfluidic dynamical response of multiphase flows can be commonly characterized successfully in terms of some dimensionless numbers, for example the Reynolds number and the capillary number [37].

Droplet-based flows use discrete volumes of fluids, whereas stratified flows rely on fluids which are continuously introduced into the system to form stable interfaces. Both the individual fluid phases and the interfaces between immiscible fluids offer useful tools. They have been applied in many application fields. Droplet-based flows are mainly used as microcapsules, microreactors, micromixers and bioassays. Stratified flows are applied in microreaction, extraction and separation, and kinetic studies.

Our discussion is in two sections. The control of generation of droplet-based flows and stratified flows is described in the first section. And then the applications of multiphase microfluidic flows are discussed based on droplet-based flows and stratified flows.

3.2 Controlling Multiphase Flow in Microfluidic Systems

Fluid is defined as a continuous, amorphous substance whose molecules move freely past one another and which has the tendency to assume the shape of its container; it can be a liquid or gas. Phase is a distinct state of matter in a system; matter that is identical in chemical composition and physical state and separated from other material by the

phase boundary. Multiphase fluids are those in which there exist at least two different fluids in a system with different chemical compositions – liquid/liquid, or with different physical states – gas/liquid.

The different behavior of a gas and liquid must be emphasized when talking about gas/liquid systems. The average distance between molecules in a gas is much greater than in a liquid. For example, $1 \mu\text{m}^3$ contains 25 million molecules of air (298K, 1atm), but 34 billion molecules of water. The average distance between molecules in this gas phase is one order of magnitude higher than the diameter of its molecules, while it approaches the molecular diameter in a liquid phase. Therefore, gas molecules move ballistically and only rarely collide, whereas liquid molecules are in constant collision. As a result, a liquid is almost incompressible, and a gas is easily compressible.

The Mach number (Ma) is a dynamic measure of fluid compressibility, and is defined as the ratio of flow velocity (v) to sound speed (a):

$$Ma = v / a \quad (3.1)$$

The flow of a compressible fluid like air can be treated as incompressible if the local Mach number is less than 0.3. Ma is much smaller in microfluidic systems due to the low flow velocity. The criterion that $Ma < 0.3$ is necessary but not sufficient to exclude compressibility. Also situations like strong density changes (induced by high local pressure changes, wall heating or cooling etc), have to be avoided to allow a treatment of the flow as approximately incompressible. Then incompressible equations can be used in both the gas and liquid phases [38].

Multiphase microflows are familiar from many macroscopic systems. The dynamical response of fluids can be commonly characterized successfully in terms of the dimensionless numbers [37]. Table 3.1 lists the force-related dimensionless numbers. These dimensionless numbers demonstrate competing phenomena among different forces: buoyancy, gravitational, inertial, viscous and interfacial forces. The Grashof number (buoyancy to viscous forces), the Bond number (gravitational to interfacial forces) and the Reynolds number (inertial to viscous forces) scale with the

third, the second and the first power of flow dimensions, respectively. The importance of forces that act on fluids therefore dramatically changes from the macro- to the microscale. With downscaling, the buoyancy, gravitational and inertial forces are less and less important and viscous and interfacial forces become more and more predominant. The capillary number (viscous to interfacial forces) stands out because it is independent of flow dimensions, and is only determined by the physical properties of the fluids and the flow velocity. In the microarea, the relative importance of forces, calculated in a water/oxygen two-phase microflow, is given by the following order: buoyancy forces < inertial forces < gravitational forces < viscous forces < interfacial forces.

Of these dimensionless numbers, the Grashof number and the Bond number will not be discussed further since the buoyancy and gravity are negligible in microdevices. The Reynolds number however is still the most frequently used dimensionless number to effectively describe microfluidics. It is a measure of the ratio of inertial forces to viscous forces:[39]

$$Re = \frac{\rho v d}{\eta} \quad (3.2)$$

where ρ ($\text{kg}\cdot\text{cm}^{-3}$) is the effective density, v ($\text{m}\cdot\text{s}^{-1}$) is the average flow velocity, η ($\text{Pa}\cdot\text{s}$) is the effective viscosity, and d (m) is the characteristic flow dimension. In a straight channel, the value of $Re \approx 10^3$ is accepted as a limit for the transition from a laminar to turbulent flow [40]. For water in a straight micro- or nanochannel with a diameter between 100 nm and 100 μm , where $\eta(\text{H}_2\text{O})=1.025\times 10^{-3}$ Pa.s, $\rho(\text{H}_2\text{O}) = 10^3$ $\text{kg}\cdot\text{m}^{-3}$ and $v = 1$ $\text{mm}\cdot\text{s}^{-1}$, the calculated Reynolds number lies between 10^{-1} and 10^{-4} . For a gas, oxygen for instance, $\eta(\text{O}_2) = 20.317\times 10^{-6}$ Pa.s and $\rho(\text{O}_2) = 1.429$ $\text{kg}\cdot\text{m}^{-3}$, the Reynolds number in the same system ranges from 10^{-5} to 10^{-2} . Therefore, inertial forces are overwhelmed by interfacial forces in microfluidic devices, and laminar flow is expected in micro- and nanochannels, and not turbulent or random flow. Consequently, in simple geometries, parabolic profiles are expected in pressure-driven flows, nearly uniform profiles for boundary forces induced flows (such as electro-osmotic-flow, wall-shear-driven-flow, etc.), or a combination of both in a complex situation [41, 42].

Table 3.1 Important force-related dimensionless numbers in multiphase micro- and nanofluidics

Dimensionless number	Definition	Equations	Scaling	Value*
Grashof	$\frac{\text{Buoyancy}}{\text{Viscous}}$	$\frac{d^3 \rho^2 g \beta \Delta T}{\eta^2}$	3	10^{-4}
Bond	$\frac{\text{Gravitational}}{\text{Interfacial}}$	$\frac{d^2 \rho g}{\sigma}$	2	10^{-5}
Reynolds	$\frac{\text{Inertial}}{\text{Viscous}}$	$\frac{d \rho v}{\eta}$	1	10^{-1}
Capillary	$\frac{\text{Viscous}}{\text{Interfacial}}$	$\frac{\eta v}{\sigma}$	0	10^{-4}

*For a water-oxygen two-phase flow: $T = 20^\circ$, $\eta(O_2) = 20.317 \times 10^{-6}$ Pa.s, $\eta(H_2O) = 1.025 \times 10^{-3}$ Pa.s, $\sigma(H_2O) = 72.8$ mN.m⁻¹, $\rho(H_2O) = 10^3$ kg.m⁻³, $\rho(O_2) = 1.429$ kg.m⁻³, $\theta(\text{water and glass}) \approx 50^\circ$, $\beta(\text{water at } 20^\circ\text{C}) = 0.00021$ °C⁻¹ assuming that $d = 10$ μm and $v = 1$ cm.s⁻¹.

In multiphase microfluidics, it is necessary to include the interfacial effects (σ) into the flow equations. With the assumptions of constant density ρ and viscosity η , and the incompressibility condition $\nabla \cdot v = 0$, the Navier-Stokes equation can then be written as [8, 43, 44]:

$$\rho \left(\frac{\partial v}{\partial t} + v \cdot \nabla v \right) = -\nabla P + f + \eta \nabla^2 v + \nabla \sigma \quad (3.3)$$

where f represents a body force density. Mass conservation furthermore states:

$$\frac{\partial \rho}{\partial t} + \nabla \cdot (\rho v) = 0 \quad (3.4)$$

At the micro- and nanoscale, as shown in Table 3.1, inertial forces become negligible, leaving a modified Stokes equation:

$$\rho \frac{\partial v}{\partial t} = -\nabla P + f + \eta \nabla^2 v + \nabla \sigma \quad (3.5)$$

Flow in microchannels can be driven not only by external pressure or forces generated by an electrical, magnetic, thermal, photic or phonic field, but also by internal forces which are determined by fluid and channel properties such as interfacial forces. Physically, these forces acting on fluids can be split into normal and tangential components. In multiphase microchannel flows, the viscous forces mainly act tangential to the interface elongating it, whereas the interfacial forces chiefly act normal to the interface inducing droplet or bubble formation (minimizing the interfacial area) [30, 45]. The capillary number is hereby used to express the competition among the forces as:

$$Ca = \frac{\eta v}{\sigma} \quad (3.6)$$

where η is the viscosity of the continuous phase (Pa.s), v is the average flow velocity (m.s^{-1}), and σ is the interfacial tension (N.m^{-1}). The capillary number is irrelevant to channel size, and can be controlled by the channel and fluid properties, and the interactions between them. It may be the most useful dimensionless number to describe multiphase microfluidic flow phenomena including flow formation [34], sizing [46], coalescing [36], mixing [47] and splitting [48].

Multiphase flow in microfluidic systems is broadly categorized into segmented (droplet-based) flow and parallel (stratified) flow architectures. The basic channel configurations used to generate multiphase flows are T, Y or cross configurations (Fig. 3.1A). Gas-liquid two-phase flows in microchannels have been studied in detail for heat-exchanger applications [49-58]. Between segmented and stratified flows there can be several other flow patterns – bubbly flow, ring flow, lump flow, and annular flow (Fig. 3.1B) [49]. The flows of immiscible liquids have been successfully manipulated to study chemical reactions and for biotechnology purposes [17, 30, 59-67]. Multiphase microchannel flow changes from the droplet-based flows to stratified flows depending on the capillary number (Ca) and fluid composition (Fig. 3.1C) [34].

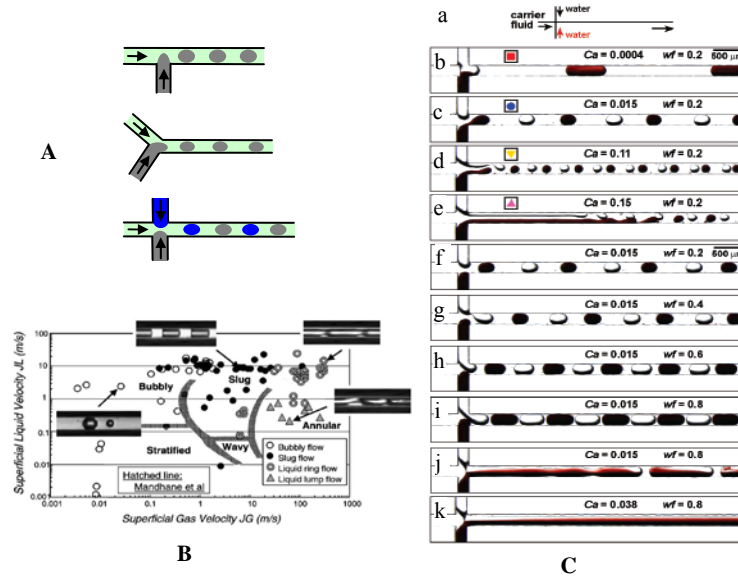


Figure 3.1 (A) Channel configurations for multiphase flow: T (top), Y (middle) and cross (bottom). (B) Gas-liquid two-phase flow patterns. Reprinted from [49] with permission from Elsevier. (C) Liquid-liquid two-phase flow patterns: (a) the cross configuration for multiphase flow, (b-k) flow patterns at different capillary number (Ca) and water fraction (wf). Reprinted with permission from [34]. Copyright (2004) American Chemistry Society.

At the microscale, immiscible gas-liquid and liquid-liquid mixtures form droplet-based flows over a wide range of flow conditions without additional control due to the high specific interfacial area (interface-area-to-volume ratio (m^2/m^3)) and consequently the high interfacial forces [30]. Vice versa, two immiscible streams would flow alongside one other if there were no interfacial forces between them. Theoretically, a stable elongated interface between two phases only occurs when tangential forces (viscous shear forces) are equal to or greater than normal forces (interfacial forces), which can be described as the capillary number on the microscale. The shift between stratified flows and slug flows occurs when the capillary number changes [45], and droplet deformation and free surface entrainment tubes is induced when $Ca \geq 0.1$ [68]. Fig 3.1C shows a typical example of multiphase flow transition

[34]. Two streams of water are added to a carrier liquid in a cross configuration. The two streams of water coalesce to form a big droplet-based flow at extremely small Ca (~ 0.0004). By increasing Ca , alternating droplet-based flow is generated with decreased droplet size. Finally, the stratified flow is obtained for $Ca > 0.15$ at a water fraction of 0.2.

Based on the definition of the capillary number, multiphase flow patterns in microchannels can be influenced by interfacial forces (σ), fluid viscosity (η), flow velocity (v) and geometric features (g_c) [35, 49, 69-71].

The first method to modify flow patterns is to modulate the interfacial forces between fluids and channel walls, or between immiscible fluids. This is also the most important method used in microdevices, and has been studied in detail. Interfacial forces can be modulated using different methods. Firstly, interfacial forces can be changed by adding surfactants [36, 45, 72-76]. Secondly, the channel wall surface can be modified by growing self-assembled monolayers – silanes on glass or silicon surfaces and thiols on Au or Ag surfaces [77-82]. Thirdly, the surface can be patterned using microcontact printing, UV-photolithography, E-beam lithography, AFM lithography and plasma etching techniques [23, 27, 66, 67, 70, 83].

The second way to influence flow patterns relies on modifying fluidic viscosity. This has been done by selecting fluids with suitable viscosity [36, 47, 84], adding components such as polymers [61] or changing temperature [85]. A two-phase droplet-based flow can be turned into a stratified flow if the viscosity of the carrier fluid is very different from that of the aqueous solutions inside the plugs or if the viscosities within different plugs vary significantly [36, 47].

The third method to change the flow pattern consists of tuning fluid velocity. This parameter is usually controlled by the application of actuation forces [35, 86, 87], and it can also be tailored by geometrical design [17, 32, 48, 88]. The droplet size in a multiphase microchannel flow is a function of flow velocity and the flow velocity ratios of two fluids [16, 18, 89]. When the flow velocity difference between two phases increases, the ratio of shear forces to normal forces increases, and droplet-based flow gradually transfers to stratified flow [35]. Thus a stable oil/water stratified stream was

obtained in a $20\ \mu\text{m} \times 100\ \mu\text{m}$ channel by increasing the flow rate to $1.67\ \text{mm}\cdot\text{s}^{-1}$ [86]. The transition between dripping and jetting can also be induced by varying the flow rate of the outermost fluid [17]. However, the flow velocity also has an upper-limit if turbulent flow is to be avoided as determined by Re [27, 70].

Finally, geometry design provides another means to influence flow patterns [70, 90]. The aspect ratio of microchannels is essential for obtaining stable two-phase flows [26, 67]. Besides, the fluid flow can be guided by added microtextures in the microchannels [67, 91].

Compared to a gas, a liquid is more flexible. Liquid viscosity and wettability can be easily changed by different means, whereas gas properties can only be little changed by changing temperature or pressure. Contradictorily, temperature and pressure will dramatically change the gas density, and consequently change the gas compressibility. Therefore, liquid/liquid multiphase flow systems are usually used for most applications, and a gas is only applied when a gaseous phase is specially required [70, 92, 93].

In conclusion, whether a stable multiphase flow can be obtained in a fluidic system depends on both fluid dynamic conditions and interface chemistries. The aim of many researchers therefore is to realize versatility and reproducibility in on-chip flow management. The design will require the smart network topologies and the interplay of multiple physical and chemical effects.

3.3 Applications of Multiphase Microfluidic Flows

Multiphase systems are more complex than their single-phase counterparts [69], but are ubiquitous in process applications. Both the immiscible individual fluids separated by interfaces and the interfaces themselves provide us with mediums that are very suitable to study microreactions and interfacial phenomena. Droplet-based multiphase flows offer controlled mini-volumes (picoliter or femtoliter) of droplets (Fig. 3.2A). These tiny droplets are almost ideal chemical reactors characterized by fast thermal transfer, efficient mixing, narrow residence time and an absence of hydrodynamic dispersion. These flows have been therefore utilized in emulsification and encapsulation [17, 30-

32], microreaction [36, 59, 94-96], synthesis [46, 69, 90], mixing [69, 97] and bioassay [60]. The interfaces between immiscible fluids in stratified flows can form ideal 2-D “nano-reactors” (Fig. 3.2B) [98, 99], and are suitable mediums to study interfacial phenomena [100, 101]. They have been used for microreactions of chemical synthesis [12, 61, 90], triphase hydrogenation [62] and biological enzymatic degradation [67] for extraction and separation [45, 66], and for kinetic studies [26, 63-66, 102].

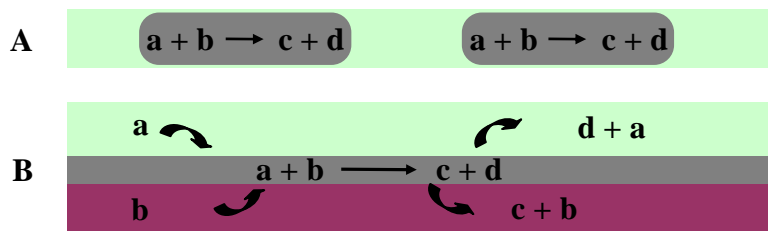


Figure 3.2 Schematic description of applications of multiphase flows as microreactors: (A) droplet-based flow, and (B) stratified flow.

3.3.1 Droplet-based flows

Immiscible gas-liquid and liquid-liquid mixtures form droplet-based flows over a wide range of flow conditions and microchannel dimensions without additional control [29]. There are several advantages for droplet-based flows to be applied in different fields. Specific interfacial areas as large as $9000\text{--}50000\text{ m}^2/\text{m}^3$ have been obtained by decreasing channel dimensions and droplet sizes down to $50\mu\text{m}$, which is a 100 times larger area than generally obtained in macroscopic channels [103]. Thermal and mass transfer is therefore rapid due to the large specific interfacial area and consequently small molecular diffusion distance. Moreover, the process controllability is wide in droplet-based flows. The size, the number, and the composition of droplets can be controlled at each step of the process [95]. By varying the initial composition of droplets, one can assess its effect on reaction yield and kinetics, providing a useful

operational research tool for laboratories. Furthermore, in a droplet-based multiphase flow, droplets are separated from channel walls by a thin layer of another immiscible (carrier) fluid, therefore the internal compositions in droplets can not disperse across the boundary and can be cleanly transported without contacting the channel walls [36, 47]. This supplies us with more flexibility to apply each droplet as a separate microreactor.

3.3.1.1 Emulsification and Encapsulation

Emulsification is one of the most frequently used methods to get droplets with sizes in the micro- and nanometer range. Conventionally, emulsion droplets are produced by applying energy (agitation, heating or ultrasonic) to the system or by adding special-structured surfactants [104-106]. However, these conventional methods often generate polydisperse emulsions. Microfluidic technology offers the capabilities of precisely handling small volume of fluids which creates almost monodisperse droplet emulsions of immiscible fluids. The droplet composition, shape and size are influenced by the wettability and the geometry of channels, and the physical properties (e.g. interfacial tension, viscosity and flow velocity) of fluids. Multi-component droplets can also be controlled by combining several miscible streams of fluids [95].

Wetting control is critical in emulsification in microchannels [16, 17, 76]. Here, surfactants become essential: depending on the surfactant structure, the oil and water two-phase flow can favor the formation of oil droplets in water or the reversed [107]. The carrier fluid must wet the channel walls preferentially over the dispersed phase [33]. The use of hydrophobic channels results in formation of water droplets in a stream of hydrophobic liquid, whereas hydrophilic channels favor the creation of oil-in-water droplets [30]. The droplet size of water-in-oil emulsions decreases when the surface is modified by more hydrophobic surfactants (when $\theta > 120^\circ$ monodisperse small size droplets were obtained) and when the ratio of the viscosity of the dispersed phase to the continuous phase (carrier fluid) increases [31]. Moreover, surfactants are often used to stabilize droplets or bubbles to avoid coalescence.

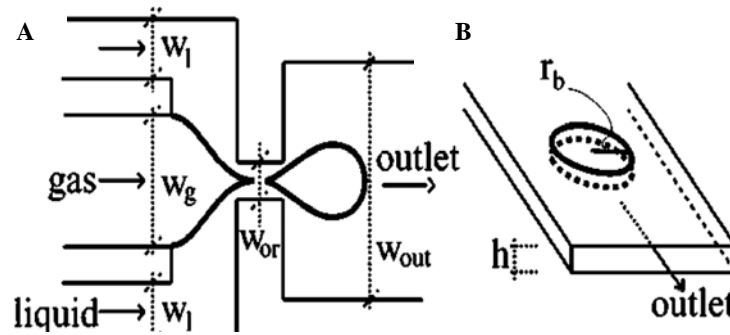


Figure 3.3 (A) Top view of the microfluidic flow-focusing device (FFD): w_l , w_g , w_{or} and w_{out} are the width of the liquid inlet channel, the gas inlet channel, the orifice and the outlet channel, respectively. (B) Illustration of a bubble in the outlet channel: r_b is the bubble radius and h is the channel height. Reused with permission from [108]. Copyright (2004) American Institute of Physics.

Geometrical design plays an important role in emulsification by microfluidic technology. Recently, Whitesides group [88, 89, 109] and the Stone group [16, 108] have done much work on droplet and bubble formation in flow-focusing devices (FFD) (Fig. 3.3). The droplet and bubble size obtained in FFD depend on fluid viscosity, flow rates and flow rate ratio between fluids. Furthermore, smaller droplets can be obtained by breakup of inner threads by surface instabilities in FFD device (satellite droplet on nanoscale) [16, 18, 19], geometrically or obstruction-mediated breakup of mother droplets to daughter droplets in T-junction microfluidic devices [110].

Double-emulsions, which are emulsions with smaller droplets of a third fluid within the larger droplets, can be obtained in one step if two phases break at the same time in a structure with three concentric capillaries. Using a device of cylindrical glass capillary tubes nested within a square glass tube highly controlled double-emulsions have been fabricated (Fig. 3.4) [17]. The capability of independently controlling the three flow rates allows varying the number and the volume of internal droplets and the shell thickness. Wetting control by selective modification of the channel surface or appropriate choice of surfactants is the key factor for making double emulsions in these microfluidic devices.

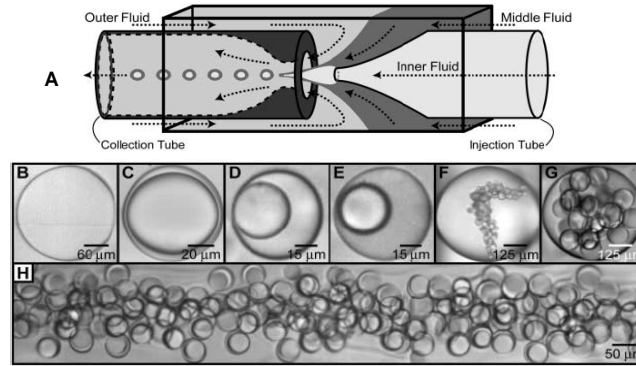


Figure 3.4 Double-emulsion fabrication: (A) schematic of the coaxial microcapillary fluidic device, (B-E) double emulsions containing only one internal droplet, (F-G) double emulsions containing many internal droplets with different size and number distribution, and (H) double emulsion droplets, each containing a single internal droplet, flowing in the collection tube. The devices used to generate these double emulsions had different geometries. Reprinted from [17] with permission from AAAS.

To obtain a controlled droplet-based flow, it is necessary to combine different parameters: geometries, wettability, viscosity and flow velocity.

Droplets surrounded by an immiscible phase in microchannels offer containers with the volume of picoliter or femtoliter, which can be used to confine and protect internal components such as cells or subcellular structures. Reverse micelles (water in oil droplets with an interface filled with surfactants) are simple life-mimicking systems which have been applied to mimic some biomembranous systems, and to be as chemical model systems for cell division, RNA replication and glutathione transferase etc. [111]. If a cell is encapsulated in the droplet, the confinement can be stable, and the confined volume prevents dilution of the molecules of interest [59]. With microfluidic technology, the 100% encapsulation of an active substance can be obtained in a one-step process [17]. Monodisperse capsules (a water droplet surrounded by a thin oil layer in air) with diameters varying between 10 and $0.15\mu\text{m}$ have been created with the Taylor cone [32]. Both the amount of internal fluid and the thickness of the coating

layer can be well controlled [17, 32]. The well-confined small-volume fluids have impressive possibilities for single-cell and single-molecule studies [112, 113].

3.3.1.2 Microreactors

Droplets separated by interfaces will confine substrates of interest inside and thus can act as microreactors. Typical examples of droplets as microreactors were demonstrated by Zheng et al [36, 96, 114]. The simple and scalable methods were used to manipulate protein crystallization in the droplets (Fig. 3.5). Oil droplets or air bubbles were inserted between reactive droplets to avoid contamination. The composition of each droplet was tuned by varying the inlet flow rates and the timescale of droplet formation [114]. Both screening of multiple proteins against a single reagent and screening of a single protein against many reagents were investigated. Crystallization conditions were screened in a micro-batch technique by eliminating evaporation of solutions and by a vapor-diffusion technique to control diffusion of water between droplets. Thaumatin crystals, bovine liver catalase crystals and glucose isomerase crystals have been produced reproducibly in a standard condition without evaporation. Thaumatin crystals [114] and lysozyme crystals [96] have been also generated with evaporation in concentrations which are too low to yield crystals without evaporation. The obtained protein crystals can be on-chip characterized by X-ray diffraction [36].

A droplet-based microchannel chip has many advantages for synthetic reactions, for example fast heat transfer and efficient mass transfer leading to high reaction yields. In particle synthesis, in particular, it is possible to tune sizes and size distributions of synthesized particles in a controllable fashion by varying the linear velocity and mean residence time. Flow profiles and patterns influence the synthesis reactions in microchannels [69, 90]. Stratified flow reactors for particle synthesis are affected by axial dispersion at high linear velocity, resulting in a wide particle size distribution. However, segmented gas-liquid reactors produce a narrow size distribution

of nanoparticles because of the internal recirculation created in the liquid plugs. Compared with a single phase flow, the corresponding multiphase flow has a narrower residence time distribution. Therefore, the particle size distribution in the segmental flow is narrower than in the stratified flow or in the single phase flow [69, 90].

The reactions of bromination [46, 95], cyanation [86], hydrogenation [115], nanoparticle [47] and core-shell particle synthesis [17] have all been carried out inside microfluidic droplets whose size and shape vary with the flow velocity, channel size and geometries. Droplets can be separated from channel walls by a thin layer of immiscible liquid which can transport the products and prevent the buildup of solid products [46, 95]. Yields increase with decreasing droplet size due to the increase of the specific area of the droplets [86].

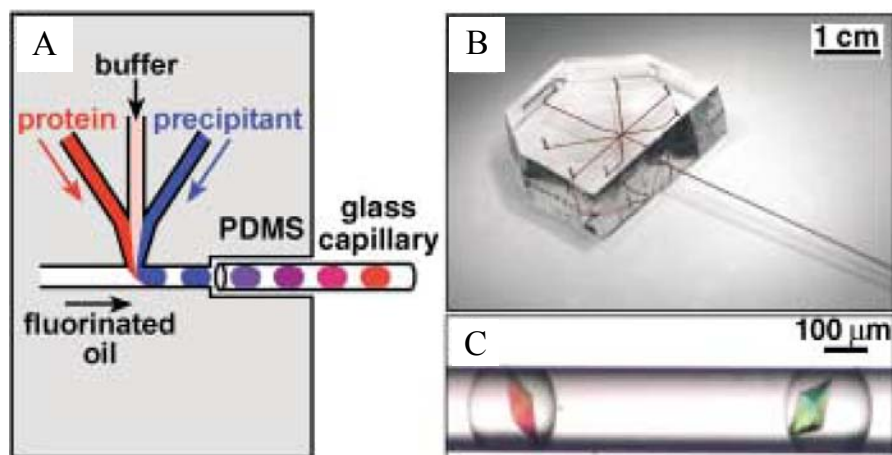


Figure 3.5 Droplet-based flow as microreactors of protein crystallization: (A) a schematic illustration of the method of forming droplets for protein crystallization trials in a PDMS/glass capillary composite microfluidic device, (B) a photograph of the composite device, and (C) a microphotograph of protein crystals grown inside droplets in a capillary. Droplets were generated by the method illustrated in (A) [96].

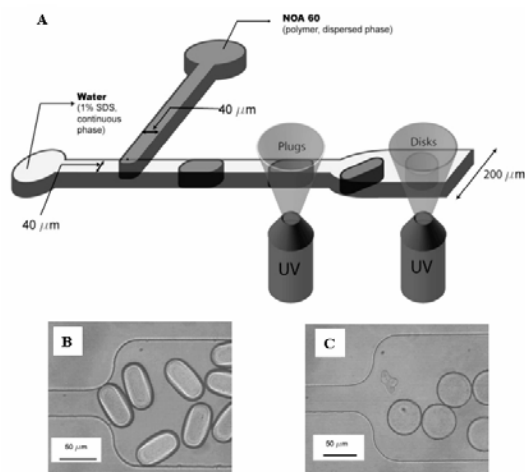


Figure 3.6 Droplet-based flow as templates for shaped particles synthesis using in-channel polymerization: (A) schematic of channel with plug and disk creation zones marked, (B) polymerized plugs, and (C) polymerized disks. Reprinted with permission from [46]. Copyright (2005) American Chemical Society.

Shaped droplets can be used as templates for shaped particles synthesis. Using in-channel polymerization, plug-like and disk-like particles have been obtained in multiphase microfluidic system by geometrical design and flow control (Fig. 3.6) [46]. The monodispersity and dimensions of the particles are influenced by varying flow rates of the continuous phase and the dispersed phase.

3.3.1.3 Mixing

Rapidly and efficiently mixing components is critical in the control of chemical reactions [116]. Droplet-based flows allow reagents to be quantized in discrete packets and mixed in strictly stoichiometric ratios. In a stratified flow, transverse mixing is controlled by diffusion. The mixing time depends on the molecular diffusion and stream width [65]. However, the situation is different in a droplet-based flow. Computational studies show that the critical parameters influencing the mixing in

droplets are the capillary number, the viscosity ratio of the droplet phase fluid to the ambient fluid, and the relative size of the droplets compared to the average channel width [117].

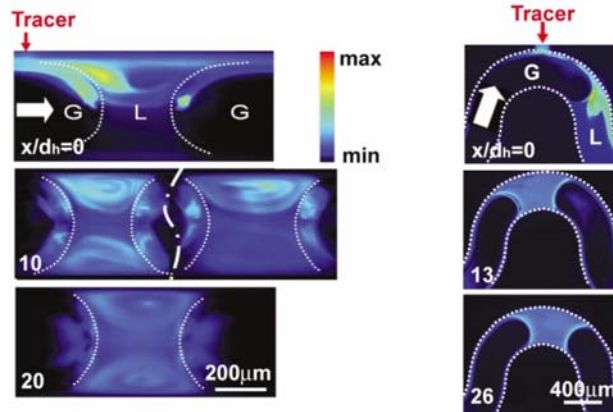


Figure 3.7 Droplet-based multiphase flow used for micromixer: false-color images of instantaneous fluorescence micrographs for the homogenization of the concentration field in a liquid segment after continuously injecting a small amount of fluorescent tracer fluid into a segmented ethanol/air flow in (A) straight channel, and (B) meandering channel. G is the gas phase (air), L is the liquid phase (ethanol), x means mixing length, and d_h is the channel hydrodynamic dimension. Reproduced by permission of The Royal Society of Chemistry [69].

An inert gas introduced into one or several miscible liquid droplets can induce narrow residence time distribution and improved mixing [69]. Fig. 3.7 shows the false-color images of instantaneous fluorescence micrographs for the homogenization of the concentration field in a liquid segment after continuously injecting a small amount of fluorescent tracer fluid into a segmented ethanol-air flow. The difference of flow velocities between the gas and liquid creates the momentum transfer between the bubbles and droplets, which generates the recirculation inside the droplets. The velocity vectors and streamline contours for straight-walled channels show an overall symmetry, whereas the asymmetric liquid velocity fields with respect to the channel

centre line are obtained when the channel walls bend [47, 69, 117]. The asymmetry increases mixing in droplets across the centre line. The mixing in segmented gas-liquid and liquid-liquid flows is even more efficient than in homogeneous chaotic mixers [118, 119] or in a long-term microdroplet mixer [120]. The mixing time can be tuned by adjusting the gas and liquid flow rates, which can be therefore used to rationally design microreactor with different reaction timescales. Furthermore, the advantage of this continuous mixing strategy is that it does not require any patterning of wall surfaces.

When the separating fluid segment between droplets is withdrawn the neighboring fluids merge and mix to each other [69, 121]. The spontaneous fusion of droplets into larger ones depends on initial size [97] and viscosity [36], and can lead to a rapid mixing of the original droplet contents by passive diffusion.

3.3.1.4 Bioassays

Biological applications form an important area of the use of many techniques including micro- and nanofluidic devices. Droplet-based microfluidic devices have been broadly applied in bioassays. In confined droplets, the photolysis of single cells (β -lymphocytes) and of subcellular organelle structures (mitochondria), for instance, has been successfully manipulated, and the activity of β -galactosidase was assayed after the cell lysis [59].

Enzyme activity has been successfully assayed by using a multiphase microchannel flow system as shown in Fig. 3.8 [36]. An array of plugs containing alkaline phosphatase (AP), catalase, ribonuclease A (RNase), and lysozyme was prepared by a capillary with every two neighboring enzyme plugs separated with two plugs containing phosphate buffered saline and air. The activity of enzymes was assayed by merging with fluorescein diphosphate (FDP) which reacts with AP to form a fluorescent product.

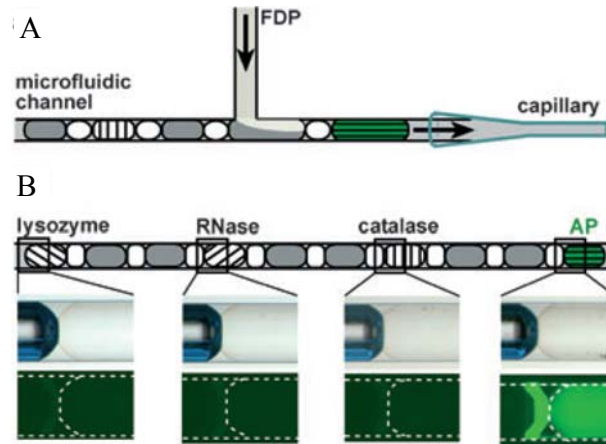


Figure 3.8 Droplet-based multiphase flow used for enzymatic assay: (A) a schematic illustration of the assay of multiple enzymes against a single substrate (fluorescein diphosphate – FDP), and (B) the result of the enzymatic assay. The drawing at the top illustrates the array of plugs. The plugs of phosphate-buffered saline (PBS) are in gray, the air bubbles are in white, and the plugs of enzymes are hatched. The microscope images in the middle are bright-field micrographs of the plugs after merging. The images at the bottom are fluorescence micrographs of the corresponding plugs. In the rightmost fluorescence micrograph, the bright line is because of the reflection of the fluorescence of the alkaline phosphatase (AP) plug from the edge of the air bubble. The dashed line indicates the outline of the capillary and the plugs [36].

The simple and cheap method for a bioassay was carried out with the delivery of multiple reagents in commercially available tubes [60]. Plugs of reagents and air spacers (which prevent reagents from mixing with each other) were sequentially sucked into the tube by applying vacuum via an array of computer controlled valves. An immunoassay was carried out based on the detection of anti-rabbit IgG. After all the plugs have traveled through the microchannel, a clear fluorescence signal on the stripe of rabbit IgG was detected, and no fluorescence was detected outside the stripe. The diagnosis of HIV has also been demonstrated by using the cartridge. Such a system can

stably store and transport the reagents, which may potentially serve as the basis for a portable and rapid analysis microdevice.

A disposable flow cytometry device has also been realized by using air-liquid two-phase flow in hydrophobic microfluidic channels [70].

Besides using the droplets themselves, the interfaces between droplets have recently also been used in studying biochemical analysis[25], interfacial long-range forces [100] and emulsion mechanism [104].

3.3.2 Stratified flows (interfaces)

In a multiphase stratified flow, the interfaces between immiscible fluids have several characteristics. Firstly, the specific interfacial area can be very large. It is for example $8000 \text{ m}^2/\text{m}^3$ [12] in a microchannel ($250 \text{ }\mu\text{m} \times 100 \text{ }\mu\text{m} \times 3 \text{ cm}$) compared with only $100 \text{ m}^2/\text{m}^3$ for conventional reactors used in chemical processes [62]. Secondly, the mass transfer coefficient can be very high because of the small transfer distance and high specific interfacial area. It is more than 100 times larger than that achieved in typical industrial gas-liquid reactors [35]. Thirdly, the interfaces of a stratified microchannel flow can be treated as nano-spaces. Simulation results show that the width of the interfaces of a stratified flow is around 1 nm, and that diffusion-based mixing occurs at the interface [98]. The interface width can be experimentally adjusted by adding surfactants [45]. Finally, reactants only contact and react with each other at the interface. Therefore, the interfaces supply us with mediums to study interfacial phenomena, diffusion-controlled interfacial reactions and extraction.

3.3.2.1 Microreactors

A co-current laminar flow at the microscale can keep streams separated yet in diffusion contact [122]. As mentioned above, the interfaces between immiscible fluids provided us with the “nano-spaces” for reactions [12]. For example, titania particles smaller than 10 nm have been prepared continuously at the interfaces of stratified immiscible liquid flow in microchannels [61].

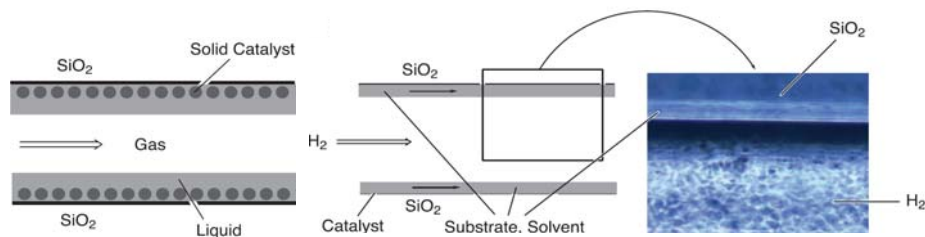


Figure 3.9 Triphase hydrogenation reaction in the stratified flow. Reprinted from [62] with permission from AAAS.

The critical factor affecting catalytic reactions – the contact area – can be extremely increased in multiphase microfluidic systems. Triphase (gas-liquid-solid) hydrogenation reactions (Fig. 3.9) have been proceeded fast and efficiently for various substrates in a very narrow channel space [62] and simulated filter and packed bed structures [35]. The space-time yield is about 10^6 times higher than in ordinary laboratory flasks.

A typical interfacial microreaction was demonstrated by Tatsuo et al [67]. A water-isooctane stratified flow was created in a microchannel ($100 \mu\text{m} \times 25 \mu\text{m}$). The substrate (*p*-chlorophenol) and the enzyme (lactase) were solubilized in aqueous and organic phases, respectively. The *p*-chlorophenol was enzymatically degraded at the aqueous/organic interface when it diffused into it. A one-dimensional diffusion model was proposed to predict the reaction. The final reaction conversion depend on the relative interface area (the aqueous/organic interface area divided by the microchannel volume), the contact time between the aqueous and organic phases, the initial concentration of the substrate, the diffusion coefficient of the substrate, the distance from the interface and the width of the organic phase.

The ability to confine immiscible liquids in specified regions opens a wide range of opportunities for synthesis in microfluidic systems. The interfaces of two immiscible fluids are continuous micro- or nanoreactors. Therefore, an interfacial polymerization reaction produced semipermeable membranes (membrane pore size $< 200 \text{ nm}$) along the

interfaces (Fig. 3.10A) [23]. Kenis et al [123] designed a smart method to fabricate microelectrodes inside capillaries using the chemical reactions in the interfaces of multiphase stratified flows (Fig. 3.10B). With the similar principle, micropatterns have been realized by synthesis of microstrips using a laminar flow microfluidic device [124].

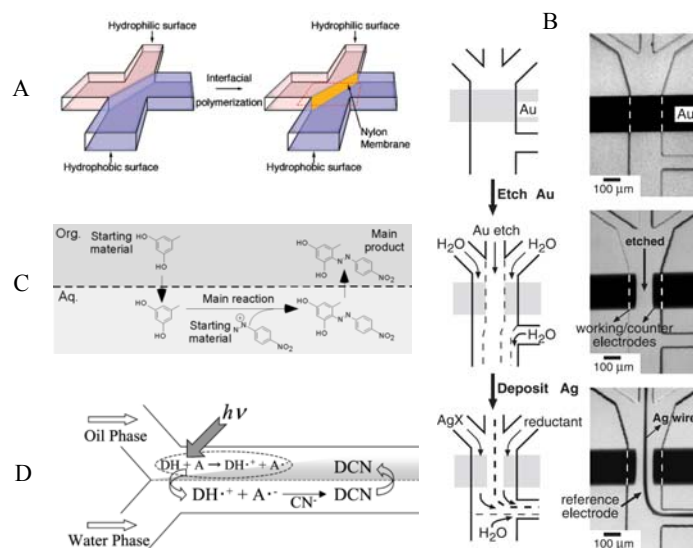


Figure 3.10 Applications of interfaces of stratified flows. (A) Schematic illustration of the polymer membrane fabricated inside the channel by interfacial polymerization. Reprinted with permission from [23]. Copyright(2002) American Chemical Society. (B) Fabrication of microelectrodes inside channels using stratified flows. Reprinted from [125] with permission from AAAS. (C) Phase transfer diazocoupling reaction. Reproduced by permission of The Royal Society of Chemistry [12]. (D) Photocyanation reaction of PyH across the interfaces (DH -an aromatic hydrocarbon, DCN – the cyanated product). Reproduced by permission of The Royal Society of Chemistry [86].

The large specific interfacial area and short molecular diffusion distance play important roles not only in the effective phase transfer of starting materials and produced chemical species, but also in avoiding undesirable side reactions and obtaining higher yield. Thus the phase transfer diazo coupling reaction using stratified

flow in a microchannel (Fig. 3.10C), as compared with the macroscale reaction, has shown fast reaction rate, high conversion ($\approx 100\%$) and minimum side reactions [12]. The reaction yield of the photocyanation of pyrene occurring across the oil/water interface of stratified flows (Fig. 3.10D) could be controlled arbitrarily by the flow rate, the channel geometry, the channel length and the specific interfacial area [86].

3.3.2.2 Extraction and separation

Extraction and separation is another application field of multiphase fluidics. Molecular diffusion governs the mass transfer in the interface between stratified flow fluids. It is well known that particles and molecules can be separated by diffusion according to their sizes [65, 126, 127]. The typical diffusion time t is calculated as:

$$t = h^2 D^{-1} \quad (3.7)$$

where h is the diffusion distance and D is the diffusion coefficient which depends on the temperature, the fluidic viscosity and the particle size. For example, at room temperature in an aqueous solution, a spherical molecule with a molecular weight of 330 (e.g. a small organic dye molecule) on average take 0.2 s to diffuse 10 μm , whereas a larger particle with a diameter of 0.5 μm (e.g. a virus) would require about 200 s to cover the same distance.

Products in a multiphase stratified flow can dissolve in one liquid (extraction) and then be removed (separation) easily due to the high interfacial area, which reduces the need for other treatments such as isolation or purification [12, 62, 128]. A micro- and nanochannel chip can thus be used as an integrated (reaction, extraction and separation) production device. As an example of applications, cell components naturally distribute over two immiscible fluidic phases with the membrane components entering the organic-aqueous interface and DNA staying in the aqueous phase. The purified DNA solution can be therefore obtained with the separated aqueous phase, leaving accumulated membrane components staying with the organic phase and interface [45]. The partitioning efficiency depends on the interface width, the flow rate, the partition coefficient and the channel geometry.

In a three-phase stratified flow, the central phase can function as a liquid membrane for extraction and separation of metal ions. Maruyama et al [66] managed a water/n-heptane/water stratified flow, and successfully processed the selective extraction and separation of a targeted metal ion from the aqueous feed solution to the receiving phase within a few seconds. The interfacial contact time and extractant concentration dominates the extraction ratio.

3.3.2.3 Kinetic Studies

A stratified flow in a microfluidic device offers a high interfacial area and therefore gives a suitable platform to investigate different interfacial phenomena. One of these phenomena is the interfacial mass transport which plays an important role in determining the overall extraction rate [102, 129]. Moreover, the study of electron transport between two phases is also essential, for example, the analysis of representative ions across interfaces [26, 64] and the determination of the exact location of phase boundaries [26]. Furthermore, oil and water interfaces can be simple models for biomembrane studies [130, 131]. The water/octanol interface for instance displays a sufficient organization to make it a valuable model for a biomembrane which has been used to assess molecule bioavailability [132]. A mixed phospholipid monolayer at the tetradecane/water interface has been applied in mimicking a biomembrane (Fig. 3.11), and the rapid hydrolysis reaction by phospholipase A₂ was performed in it [131].

A variety of experimental techniques have been used to probe the kinetics of reactions at the interfaces: mass transfer was determined by microscopic detection of the changes of fluorescent component concentrations [63, 102], ion transfer was measured by voltammetry [26, 64] or chronoamperometry [26], the adsorption of molecules to an interface could be investigated by using a method called interface-specific second-harmonic generation of laser light [130], and the real time changes of interfacial tensions induced by reactions could be tested by laser spectroscopic techniques [131]. Monitoring signal intensities along a T-sensor detection channel (in-flow direction) suggests a method to look at the kinetics of a reaction, allowing kinetic

diagnostic reactions to be measured as a function of distance from the starting point of the diffusion interaction [65].

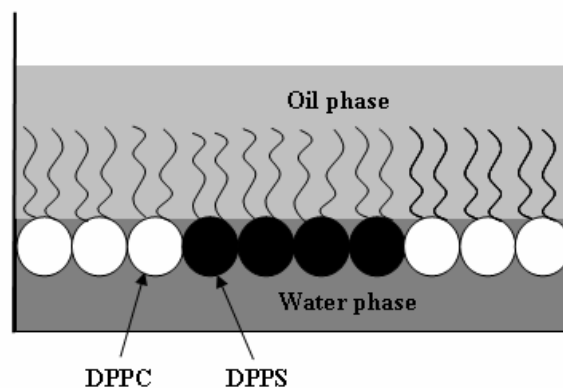


Figure 3.11 The DPPC (dipalmitoyl phosphatidylcholine)/DPPS (dipalmitoyl phosphatidylserine) mixed monolayer at the tetradecane/water interface as a biomembrane model.

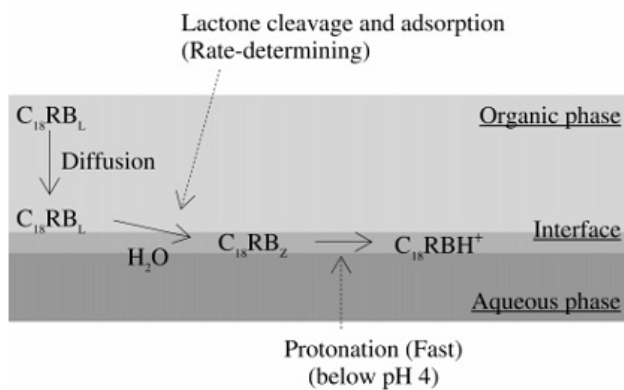


Figure 3.12 Schematic drawing of the lactone cleavage reaction mechanism of C18RB at the liquid/liquid interface. C18RBL, C18-RBZ, and C18RBH⁺ indicate the lactone, zwitterion, and protonated cation forms, respectively. Reprinted with permission from [63]. Copyright (2005) American Chemical Society.

A typical example of the study of reaction kinetics is the use of an organic inner phase with an aqueous outer sheath flow (Fig. 3.12) [63]. The fast interfacial lactone cleavage reaction was measured by two-photon excitation fluorescence spectra, and the diffusion of solutes was described by the Box-model [133]. Calculated by the time-dependent Langmuir adsorption model, different cleavage rate constants have been obtained at the toluene/water and heptane/water interfaces.

3.4 Conclusions and Outlook

Multiphase micro- and nanochannel flow confines small volumes of several immiscible fluids in one device. Compared with single-phase systems, multiphase systems are more difficult to manipulate. They are however very useful since the immiscible fluids are separated from each other by flexible fluidic interfaces, and the small-volume confinement and multiphase coexistence have many applications.

Laminar flow is expected in microchannel flow due to the low Reynolds number. Multiphase microchannel flow varies between droplet-based flows and stratified flows depending on the capillary number. The transition from a droplet-based flow to a stratified flow can be obtained by choosing the properties of the fluids and the flow velocity. According to the different flow patterns a lot of application fields have been exploited. Droplet-based flows allow reagents to be quantized in discrete packets and mixed in strictly stoichiometric ratios. Well-confined small-volume droplets have been used as microcapsules, microreactors, micromixers and bioassay mediums. Stratified flows have clear flexible interfaces between immiscible fluids. These “nano-space” interfaces have been applied in reaction, extraction and kinetic studies.

Multiphase fluidic operation involves complex interactions of several physicochemical phenomena, including fluid hydrodynamics, transport phenomena and surface characteristics. Successful design, control and application of multiphase fluidic systems require a thorough understanding of the interactions of physicochemical properties at different spatial and temporal scales in each phase and between phases. Many applications have already been reported in literatures, but undoubtedly many more will still follow.

References

- [1] D. A. S. W. B. Russel, W. R. Schowalter *Colloidal Dispersions*, Vol. 1-14, UK: Cambridge Univ. Press., Cambridge **1989**.
- [2] T. H. Schulte, R. L. Bardell, B. H. Weigl, *Clinica Chimica Acta* **2002**, 321, 1.
- [3] S. D. Logsdon, *Bound water in Soil*, Vol. 0, Marcel Dekker, Inc., New York **2004**.
- [4] M. J. Canny, *Annu. Rev. Fluid Mech.* **1977**, 9, 275.
- [5] R. D. Jensen, S. A. Taylor, H. H. Wiebe, *Plant Physiol.* **1961**, 36, 633.
- [6] T. J. Ryan, *Pharmacol. Ther.* **1980**, 10, 27.
- [7] A. Manz, N. Graber, H. M. Widmer, *Sens. Actuator B, Chem.* **1990**, 1, 244.
- [8] T. M. Squires, S. R. Quake, *Rev. Mod. Phys.* **2005**, 77, 977.
- [9] J. C. T. Eijkel, A. van den Berg, *Microfluid. Nanofluid.* **2005**, 1, 249.
- [10] S. Quake, *Trac-Trends Anal. Chem.* **2002**, 21, XII.
- [11] T. Thorsen, S. J. Maerkl, S. R. Quake, *Science* **2002**, 298, 580.
- [12] H. Hisamoto, T. Saito, M. Tokeshi, et al., *Chem. Commun.* **2001**, 2662.
- [13] Y. Kikutani, H. Hisamoto, M. Tokeshi, et al., *Lab Chip* **2004**, 4, 328.
- [14] D. Mijatovic, J. C. T. Eijkel, A. van den Berg, *Lab Chip* **2005**, 5, 492.
- [15] M. L. K. Hoa, M. H. Lu, Y. Zhang, *Adv. Colloid Interface Sci.* **2006**, 121, 9.
- [16] S. L. Anna, N. Bontoux, H. A. Stone, *Appl. Phys. Lett.* **2003**, 82, 364.
- [17] A. S. Utada, E. Lorenceau, D. R. Link, et al., *Science* **2005**, 308, 537.
- [18] Y. C. Tan, V. Cristini, A. P. Lee, *Sens. Actuator B, Chem.* **2006**, 114, 350.
- [19] Y. C. Tan, A. P. Lee, *Lab Chip* **2005**, 5, 1178.
- [20] W. Drenckhan, S. J. Cox, G. Delaney, et al., *Colloid Surf. A-Physicochem. Eng. Asp.* **2005**, 263, 52.
- [21] P. Garstecki, G. M. Whitesides, H. A. Stone, *Phys. Rev. Lett.* **2005**, 94, 1645011.
- [22] J. P. Raven, P. Marmottant, *Phys. Rev. Lett.* **2006**, 97, 154501.
- [23] B. Zhao, N. O. L. Viernes, J. S. Moore, et al., *J. Am. Chem. Soc.* **2002**, 124, 5284.
- [24] P. Wilde, A. Mackie, F. Husband, et al., *Adv. Colloid Interface Sci.* **2004**, 108-09, 63.
- [25] L. S. Roach, Song, H., Ismagilov, R. F., *Anal. Chem.* **2005**, 77, 785.
- [26] S. Peulon, V. Guillou, M. L'Her, *J. Electroanal. Chem.* **2001**, 514, 94.
- [27] A. Hibara, M. Nonaka, H. Hisamoto, et al., *Anal. Chem.* **2002**, 74, 1724.
- [28] A. van den Berg, T. S. J. Lammerink, *Micro total analysis systems: Microfluidic aspects, integration concept and applications*, Vol. 194, Springer-Verlag, Berlin, Berlin 33 **1998**.
- [29] T. Pfohl, F. Mugele, R. Seemann, et al., *ChemPhysChem* **2003**, 4, 1291.
- [30] M. Joanicot, A. Ajdari, *Science* **2005**, 309, 887.
- [31] T. Kawakatsu, G. Tragardh, C. Tragardh, et al., *Colloid Surface A* **2001**, 179, 29.
- [32] I. G. Loscertales, A. Barrero, I. Guerrero, et al., *Science* **2002**, 295, 1695.
- [33] J. D. Tice, H. Song, A. D. Lyon, et al., *Langmuir* **2003**, 19, 9127.
- [34] B. Zheng, J. D. Tice, R. F. Ismagilov, *Anal. Chem.* **2004**, 76, 4977.
- [35] M. W. Losey, R. J. Jackman, S. L. Firebaugh, et al., *J. Microelectromech. Syst.* **2002**, 11, 709.
- [36] B. Zheng, R. F. Ismagilov, *Angew. Chem. Int. Ed.* **2005**, 44, 2520.
- [37] H. A. Stone, A. D. Stroock, A. Ajdari, *Annu. Rev. Fluid Mech.* **2004**, 36, 381.
- [38] M. Tatineni, X. Zhongt, *American Institute of Aeronautics and Astronautics* **2004**, 11712.
- [39] C. E. Brennen, *Fundamentals of Multiphase Flows*, Vol. California Institute of Technology, Pasadena, California, Cambridge University Press, **2005**.
- [40] K. V. Sharp, R. J. Adrian, *Exp. Fluids* **2004**, 36, 741.

- [41] J. Y. Min, E. F. Hasselbrink, S. J. Kim, *Sens. Actuator B, Chem.* **2004**, *98*, 368.
- [42] L. Shui, J. C. T. Eijkel, A. van den Berg, **2007**, *121*, 263.
- [43] G. Tryggvason, A. Esmaceli, J. C. Lu, et al., **2006**, *38*, 660.
- [44] F. H. J. v. d. Heyden, Vol. PhD, Technische Universiteit Delft, Delft **2006**, 22.
- [45] V. Reddy, J. D. Zahn, *J. Colloid Interface Sci.* **2005**, *286*, 158.
- [46] D. Dendukuri, K. Tsoi, T. A. Hatton, et al., *Langmuir* **2005**, *21*, 2113.
- [47] I. Shestopalov, J. D. Tice, R. F. Ismagilov, *Lab Chip* **2004**, *4*, 316.
- [48] D. R. Link, S. I. Anna, D. A. Weitz, et al., *Phys. Rev. Lett.* **2004**, *92*, 545031.
- [49] A. Serizawa, Z. Feng, Z. Kawara, *Exp. Therm. Fluid Sci.* **2002**, *26*, 703.
- [50] F. G. T. J.J.Hwang, Chin Pan, *Int. J. Multiphas. Flow* **2005**, *31*, 548.
- [51] S. M. G. K.A.Triplett, S.I.Abdel-Khalik,A.LeMouel, B.N.McCoud, *Int. J. Multiphas. Flow* **1999**, *25*, 377.
- [52] Q. C. B. T.S.Zhao, *Int. J. Multiphas. Flow* **2001**, *27*, 765.
- [53] S. M. G. K.A.Triplett, S.I.Abdel-Khalik,A.LeMouel, B.N.McCoud, *Int. J. Multiphas. Flow* **1999**, *25*, 395.
- [54] S. M. G.TL.Narrow,S.I.Abdel-KHALIK,D.L.Sadowski, *Int. J. Multiphas. Flow* **2000**, *26*, 1281.
- [55] Ruben Wedin, A. A. Dahlkild, *Ind. Eng. Chem. Res.* **2001**, *40*, 228.
- [56] G. M. h. Vladimir S. Ajaev, *J. Colloid Interface Sci.* **2001**, *240*, 259.
- [57] L. P. Y. Y.P.Peles, G.Hensroni, *Int. J. Multiphas. Flow* **2000**, *26*, 1063.
- [58] L. A. E. L.P.Yarin, G.Hetsroni, *Int. J. Multiphas. Flow* **2002**, *28*, 1589.
- [59] M. Y. He, J. S. Edgar, G. D. M. Jeffries, et al., *Anal. Chem.* **2005**, *77*, 1539.
- [60] V. Linder, S. K. Sia, G. M. Whitesides, *Anal. Chem.* **2005**, *77*, 64.
- [61] H. Z. Wang, H. Nakamura, M. Uehara, et al., *Chem. Commun.* **2002**, 1462.
- [62] J. Kobayashi, Y. Mori, K. Okamoto, et al., *Science* **2004**, *304*, 1305.
- [63] T. Tokimoto, S. Tsukahara, H. Watarai, *Langmuir* **2005**, *21*, 1299.
- [64] S. Sawada, M. Taguma, T. Kimoto, et al., *Anal. Chem.* **2002**, *74*, 1177.
- [65] B. H. Weigl, P. Yager, *Science* **1999**, *283*, 346.
- [66] T. Maruyama, H. Matsushita, J. Uchida, et al., *Anal. Chem.* **2004**, *76*, 4495.
- [67] T. Maruyama, J. Uchida, T. Ohkawa, et al., *Lab Chip* **2003**, *3*, 308.
- [68] S. T. Thoroddsen, Y. K. Tan, *Phys. Fluids* **2004**, *16*, L13.
- [69] A. Gunther, S. A. Khan, M. Thalmann, et al., *Lab Chip* **2004**, *4*, 278.
- [70] D. Huh, Y. C. Tung, H. H. Wei, et al., *Biomed. Microdevices* **2002**, *4*, 141.
- [71] G. N. Doku, A. Van den Berg, W. Verboom, et al., *Ind. Eng. Chem. Res.* **2003**, *42*, 3721.
- [72] B. S. Gallardo, V. K. Gupta, F. D. Eagerton, et al., *Science* **1999**, *283*, 57.
- [73] D. Y. K. Yap, D. P. Gaver, *Phys. Fluids* **1998**, *10*, 1846.
- [74] D. E. Bennett, B. S. Gallardo, N. L. Abbott, *J. Am. Chem. Soc.* **1996**, *118*, 6499.
- [75] C. Maldarelli, http://mured.nasaprs.com/report/rt_reports/2001/FAR_CUNY_Maldarelli_Rpt.pdf.
- [76] R. Dreyfus, P. Tabeling, H. Willaime, *Phys. Rev. Lett.* **2003**, *90*, 1445051.
- [77] L. M. Siewierski, W. J. Brittain, S. Petrash, et al., *Langmuir* **1996**, *12*, 5838.
- [78] G. Moller, M. Harke, H. Motschmann, et al., *Langmuir* **1998**, *14*, 4955.
- [79] C. L. Feng, Y. J. Zhang, J. Jin, et al., *Langmuir* **2001**, *17*, 4593.
- [80] M. O. Wolf, M. A. Fox, *J. Am. Chem. Soc.* **1995**, *117*, 1845.
- [81] S. Abbott, J. Ralston, G. Reynolds, et al., *Langmuir* **1999**, *15*, 8923.
- [82] K. Ichimura, S. K. Oh, M. Nakagawa, *Science* **2000**, *288*, 1624.
- [83] C. Rosslee, N. L. Abbott, *Curr. Opin. Colloid Interface Sci.* **2000**, *5*, 81.
- [84] J. Bico, D. Quere, *J. Fluid Mech.* **2002**, *467*, 101.

- [85] J. Z. Chen, S. M. Troian, A. A. Darhuber, et al., *J. Appl. Phys.* **2005**, 97, 014906/1.
- [86] K. Ueno, F. Kitagawa, N. Kitamura, *Lab Chip* **2002**, 2, 231.
- [87] P. Garstecki, G. M. Whitesides, *Phys. Rev. Lett.* **2006**, 97.
- [88] P. Garstecki, M. J. Fuerstman, G. M. Whitesides, *Phys. Rev. Lett.* **2005**, 94, 2345021.
- [89] S. Takeuchi, P. Garstecki, D. B. Weibel, et al., *Adv. Mater.* **2005**, 17, 1067.
- [90] S. A. Khan, A. Gunther, M. A. Schmidt, et al., *Langmuir* **2004**, 20, 8604.
- [91] M. Tokeshi, T. Minagawa, K. Uchiyama, et al., *Anal. Chem.* **2002**, 74, 1565.
- [92] J. H. Tsai, L. W. Lin, *J. Microelectromech. Syst.* **2002**, 11, 665.
- [93] N. De Mas, A. Günther, K. F. Jensen, et al., *Ind. Eng. Chem. Res.* **2003**, 42, 698.
- [94] W. Zhan, G. H. Seong, R. M. Crooks, *Anal. Chem.* **2002**, 74, 4647.
- [95] Z. T. Cygan, J. T. Cabral, K. L. Beers, et al., *Langmuir* **2005**, 21, 3629.
- [96] B. Zheng, J. D. Tice, L. S. Roach, et al., *Angew. Chem. Int. Ed.* **2004**, 43, 2508.
- [97] J. A. Schwartz, J. V. Vykoukal, P. R. C. Gascoyne, *Lab Chip* **2004**, 4, 11.
- [98] P. A. Fernandes, M. N. D. S. Cordeiro, J. A. N. F. Gomes, *J. Phys. Chem. B* **2001**, 105, 981.
- [99] H. Hisamoto, T. Horiuchi, K. Uchiyama, et al., *Anal. Chem.* **2001**, 73, 5551.
- [100] R. Aveyard, B. P. Binks, J. H. Clint, et al., *Phys. Rev. Lett.* **2002**, 88, 2461021.
- [101] M. G. Nikolaidis, A. R. Bausch, M. F. Hsu, et al., *Nature* **2002**, 420, 299.
- [102] D. A. Wenn, J. E. A. Shaw, B. Mackenzie, *Lab Chip* **2003**, 3, 180.
- [103] K. Jähnisch, M. Baerns, V. Hessel, et al., *J. Fluorine Chem.* **2000**, 105, 117.
- [104] S. Pautot, B. J. Frisken, J. X. Cheng, et al., *Langmuir* **2003**, 19, 10281.
- [105] N. Shahidzadeh, D. Bonn, J. Meunier, et al., *Langmuir* **2000**, 16, 9703.
- [106] T. Nishimi, C. A. Miller, *Langmuir* **2000**, 16, 9233.
- [107] C. N. Baroud, H. Willaime, **2004**, 5, 547.
- [108] P. Garstecki, I. Gitlin, W. DiLuzio, et al., *Appl. Phys. Lett.* **2004**, 85, 2649.
- [109] S. Xu, Z. Nie, M. Seo, et al., *Angew. Chem. Int. Ed.* **2005**, 44, 724.
- [110] D. R. Link, S. L. Anna, D. A. Weitz, et al., *Phys. Rev. Lett.* **2004**, 92.
- [111] G. G. Chang, T. M. Huang, H. C. Hung, *Proc. natl. Sci. Counc. ROC(B)* **2000**, 24, 89.
- [112] Y. Rondelez, G. Tresset, T. Nakashima, et al., *Nature* **2005**, 433, 773.
- [113] Y. Rondelez, G. Tresset, K. V. Tabata, et al., *Nat. Biotechnol.* **2005**, 23, 361.
- [114] B. Zheng, L. S. Roach, R. F. Ismagilov, *J. Am. Chem. Soc.* **2003**, 125, 11170.
- [115] Y. Onal, M. Lucas, P. Claus, *Chem. Eng. Technol.* **2005**, 28, 972.
- [116] D. R. Meldrum, M. R. Holl, *Science* **2002**, 297, 1197.
- [117] M. Muradoglu, H. A. Stone, *Phys. Fluids* **2005**, 17, 1.
- [118] A. D. Stroock, S. K. W. Dertinger, A. Ajdari, et al., *Science* **2002**, 295, 647.
- [119] R. H. Liu, M. A. Stremmer, K. V. Sharp, et al., *J. Microelectromech. Syst.* **2000**, 9, 190.
- [120] H. Song, J. D. Tice, R. F. Ismagilov, *Angew. Chem. Int. Ed.* **2003**, 42, 768.
- [121] K. Hosokawa, T. Fujii, I. Endo, *Anal. Chem.* **1999**, 71, 4781.
- [122] E. R. Choban, P. J. A. Kenis, L. J. Markoski, et al., *J. Power Sources* **2004**, 128, 54.
- [123] P. J. A. Kenis, R. F. Ismagilov, G. M. Whitesides, *Science* **1999**, 285, 83.
- [124] D. G. Shchukin, D. S. Kommireddy, Y. Zhao, et al., *Adv. Mater.* **2004**, 16, 389.
- [125] P. J. A. Kenis, R. F. Ismagilov, G. M. Whitesides, **1999**, 285, 83.
- [126] K. Yamashita, D. Ogura, Y. Yamaguchi, et al., *Anal. Bioanal. Chem* **2005**, 382, 1477.
- [127] J. Oakey, J. Allely, D. W. M. Marr, *Biotechnol. Progr.* **2002**, 18, 1439.
- [128] M. Yamada, V. Kasim, M. Nakashima, et al., *Biotechnol. Bioeng.* **2004**, 88, 489.
- [129] T. Tokimoto, H. Watarai, S. Tsukahara, *Analyst* **2004**, 129, 1099.
- [130] D. T. Cramb, S. C. Wallace, *J. Phys. Chem. B* **1997**, 101, 2741.

-
- [131] T. Morisaku, H. Yui, T. Sawada, *Anal. Sci.* **2004**, *20*, 1605.
[132] D. T. Cramb, S. C. Wallace, *J. Phys. Chem. B* **1997**, *101*, 2741.
[133] T. Tokimoto, S. Tsukahara, H. Watarai, *B. Chem. Soc. Jpn.* **2003**, *76*, 1569.

Chapter 4

Capillary instability, Squeezing and Shearing in Head-on Microfluidic Channels

We investigate two-phase (oil and water) flow in head-on microfluidic devices which consist of two identical channels as inlets and the “long leg” as a constriction channel leading to a wider outlet section. Over an exceptionally broad range of flow rates of 10^{-4} ~ 10 $\mu\text{L}\cdot\text{min}^{-1}$ in 10 ~ 100 μm microchannels, corresponding to capillary numbers of 10^{-6} ~ 10^{-1} , a two-phase flow map is presented. The flow patterns are distinguished as geometry or flow related dripping, jetting and threading. These phenomena are interpreted as capillary instability, squeezing and shearing by considering the contribution of different forces acting at the oil/water interface. This device provides us with a broad choice to generate droplets of different size by modifying either the geometrical design or the flow rates.

4.1 Introduction

Multiphase microfluidics is a rapidly expanding field due to its great range of applications [1, 2]. Complex fluidic systems play a very important role in pharmaceuticals, cosmetic, food and oil industries. The fluids of interest in chemistry and biotechnology are rarely simple single-phase liquids [3]. Most of fluid transport, compartmental chemistry, interfacial phenomena and applications employ multiphase fluidic systems. Both droplet-based flow and stratified flow have found applications for chemical and biological purposes [4, 5]. Droplet-based flow is mainly used to create microcapsules, microreactors, micromixers and bioassays. Stratified flow is applied in microreaction, extraction and separation, and kinetic studies.

The dynamics of the inner liquid threads is dominated by the pressure difference (normal stress) exerted across the interface [6]. Since interfacial tension acts only at interfaces, and viscous forces act in the bulk of fluids, boundary conditions must be considered. The normal force is defined as outward-facing and a minus sign is due to pressure being defined as positive if it is compressive (i.e. inward-facing). The boundary condition given balances normal forces at an interface,

$$P = -\tau_{\sigma} + \tau_v + P_{\text{hyd}} \quad (4.1)$$

where P (Pa) is the local pressure, τ_{σ} (Pa) is the force per unit area due to interfacial tension, τ_v (Pa) is the viscous stress per unit area due to the fluidic dynamics, and P_{hyd} (Pa) is the hydrostatic pressure. We see that the interfacial force, dynamic force, and hydrostatic pressure difference contribute to the force at the interface. The local force at the interface is related to typical fluid dimension (d) and flow speed (v), due to the dependence of these forces on both. The three coupled forces and corresponding dimensionless numbers are shown in Table 4.1.

The Bond number is irrelative to flow speed, and only determined by the typical dimension d . At the microscale, $d < 3$ mm, the gravity is negligible because of the small Bond number [7, 8]. The capillary number Ca is the most often mentioned dimensionless number when describing multiphase flow at the nano- and microscale,

Table 4.1 Dimensionless numbers relative to fluidic flow

	Gravity force ($\rho g L$)	Viscous force ($\eta v/L$)	Inertial effects (ρv^2)
Interfacial tension (σ/L)	$Bo = \rho g d^2 / \sigma$	$Ca = \eta v / \sigma$	$We = \rho v^2 d / \sigma$
Viscous force	Bo/Ca	1	$Re = \rho v d / \eta$

Bo , Ca , We and Re represent the Bond number, capillary number, Weber number and Reynolds number, respectively. In the table, ρ is the fluid density, g is the gravity acceleration; σ means the interfacial tension, v indicates the flow speed, η is the dynamic viscosity, and d denotes a typical radial dimension. All forces are per unit area.

especially for droplet-based flow [9]. Ca is independent of d , however proportional to v . In microfluidic system, the flow speed is commonly low, which makes interfacial tension dominant in most cases. In the experiments described in this chapter the balance between viscous and interfacial forces changes considerably since Ca varies between 10^{-6} and 10^{-1} . As seen from the definition, the Weber number is a function of both v and d . It is seldom referred to in gas-liquid microsystems because of the low density of gas and small d . Nevertheless, it can become dominant when high density fluids flow fast in microsystems [10, 11]. In the experiments reported in this chapter, We is smaller than 10^{-5} , implying that inertial effects are negligible. The ratio of inertial effects to viscous forces is described by Re which is also generally low in microfluidic flow. Viscous flow is therefore as a rule sustained for micro- and nanofluidics, and this holds as well for the experimental conditions reported in this chapter [9].

Generally in literature, flow rates in a range corresponding to $Ca \in (10^{-3}, 10^{-1})$ have been investigated [6, 12, 13], in which the breakup mechanism is controlled by the capillary number [1, 14]. In some devices where high viscosity inner fluids are used at high flow rates, inertia also contributes to the formation mechanism [10]. The most used geometries for two-phase flow are T-junctions [12, 14-16], flow-focusing devices (FFD) [6, 13, 17-20] or co-flowing devices [10, 21]. Experiments have thereby mostly been performed in microchannels fabricated in PDMS. Water-in-oil flow would then be

typically obtained due to the wettability of PDMS for oil. However, the permeability and deformability of PDMS prevents investigators from using extremely low or high flow rates (or pressure).

What we present here is a head-on microfluidic device, as shown in Fig. 4.1, consisting of two identical inlets, a constriction channel and a wide outlet channel. Two liquid phases (water-outer liquid and oil-inner liquid) are introduced from two inlets, meet at the junction (or the entrance of the constriction channel), and then flow through the constriction channel and step out into the wide outlet channel. The junction region (j) and the step region from narrow constriction to wide outlet channel (s) are two important geometrical features, shown in Fig. 4.1b. The total pressure across the oil-water interface (P) (Equation 1) in the j and s areas will be called P_j and P_s . This geometry is different from other devices reported in literature. Furthermore, we fabricated these microchannels in hard and strong sealed materials (silicon and glass). The fact that the chip materials are non-deformable enables us to pump fluids at high flow rate (or pressure), and the fact that they are non-permeable enables fluid flow at very low flow rates, this is contrast to the generally used PDMS devices. Therefore, we could perform experiments in a wide range of flow rates (or pressures). Flow behavior ranging from dripping, jetting to threading were obtained in the flow rate range of $10^4 \sim 10 \mu\text{L}/\text{min}$ corresponding to Ca of $10^{-6} \sim 10^{-1}$. We interpret the occurrence of these regimes by considering the contribution of the different forces (τ_σ , τ_v , P_{hyd}) mentioned at the interface.

4.2 Experimental

The head-on configuration employed is illustrated in Fig. 4.1. Microchannels were fabricated using standard photolithography processes. The interconnection holes were opened from the backside of the wafers by using powder-blasting techniques. Two wafers were then thermally bonded. The resulting bonded wafers were finally diced into $10 \text{ mm} \times 20 \text{ mm}$ chips.

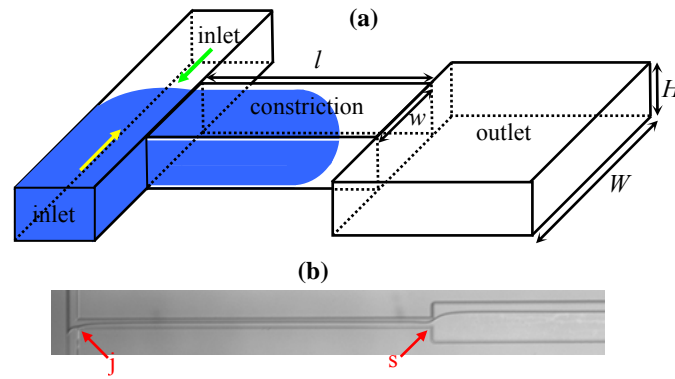


Figure 4.1 Microchannel configuration: (a) schematic 3D drawing of the head-on devices, H – height ($10\ \mu\text{m}$), W – outlet channel width ($100\ \mu\text{m}$), w – constriction channel width ($10, 20, 30, 40, 60, 80$ or $100\ \mu\text{m}$), l – constriction channel length ($100, 500$ or $1000\ \mu\text{m}$), and (b) a photograph of threading oil-water two-phase flow. j and s indicate junction and step areas, respectively.

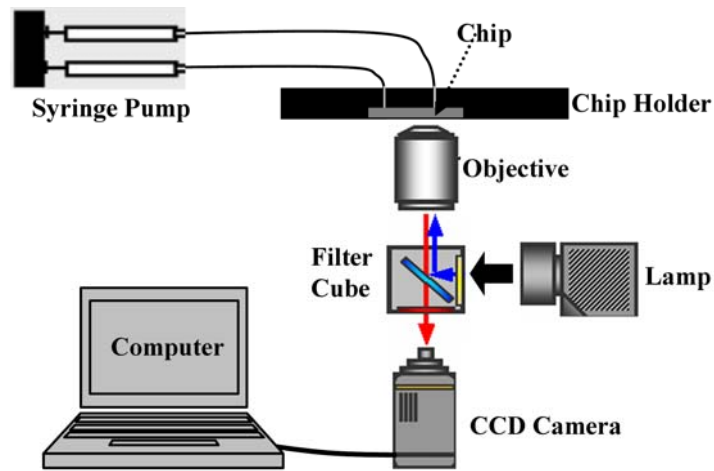


Figure 4.2 Schematic of the experimental setup.

Chips were fixed in a home-made chip holder and connected to syringes via capillary tubing (OD 1/16 inch , ID 50 μm) and Nanoport connectors including a filter (INACOM INSTRUMENTS BV, Upchurch Scientific, Holland). Connectors and chips were sonically cleaned in DI water for 15 min before use. Flow was controlled using a dual syringe pump (Harvard PHD 22/2000, HUGO SACHS ELECTRONIK-HAVARD APPARATUS GmbH). The flow was visualized using an inverted microscope (Leica DMIRM) and recorded by using CCD cameras (Orca ER and Phantom V). The experimental setup is shown in Fig. 4.2.

The oil phase which is hexadecane shows up black in the images, and the water phase which contains 0.01M sodium dodecyl sulfate (SDS 99+%, $\text{CH}_3(\text{CH}_2)_{11}\text{OSO}_3\text{Na}$) and 0.01M fluorescein sodium salt appears white due to the excited fluorescein. All chemicals were bought from Sigma-Aldrich Chemie GmbH, Germany, and used without further treatment. Droplet volume was calculated as measured droplet area from images multiplied by channel height when the droplet diameter was much bigger than channel height, or calculated directly from the measured droplet diameter as a sphere when droplet size was comparable to channel height.

4.3 Results and Discussion

Two immiscible phases (water and oil) are fed from two inlets by a syringe pump. They meet at the entrance of the constriction channel, forming an oil-in-water flow due to the wettability of the channel walls. A typical flow map showing the different observed flow regimes based on the capillary numbers of oil (inner phase) and water (outer phase) phases (Ca_o and Ca_w) is displayed in Fig. 4.3. Due to the existence of the junction (j) and step (s) geometry factors we morphologically find five typical flow regimes: (I) geometry-determined dripping, (II) flow-rate-dependent dripping, (III) flow-rate-dependent jetting, (IV) geometry-determined jetting and (V) threading. In our microfluidic circuits, dripping and jetting correspond to the oil thread breakage occurring at the junction and in the constriction channel downstream from the junction.

Threading (V) is distinguished from dripping and jetting, since the liquid threads display continuous morphology along both the constriction and the outlet channels. All regimes are illustrated by photomicrographs in Fig. 4.3b.

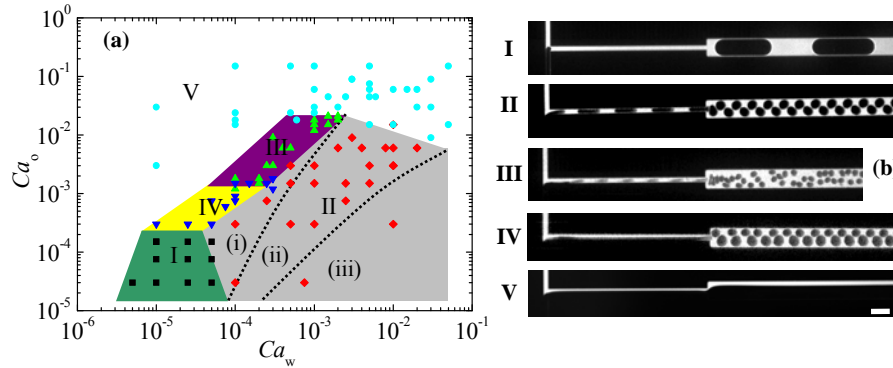


Figure 4.3 Flow map: (a) typical morphologically different flow regimes observed based on oil and water flow rates; (b) photographs of the corresponding flow patterns: (I) geometry-determined dripping (■), (II) flow-rate-dependent dripping (◆) (i, ii and iii: three subregimes treated in section 3.2), (III) flow-rate-dependent jetting (▲), (IV) geometry-determined dripping (▼), and (V) threading (●). $h = 10 \mu\text{m}$, $l = 1000 \mu\text{m}$ and $w = 30 \mu\text{m}$. The scale bar is $100 \mu\text{m}$.

Geometry-determined dripping and jetting (I & IV) is defined as a flow regime where the sudden expansion of the inner liquid (oil) at the step region leads to breakup at the junction (j) or the step (s) area to form droplets (*capillary instability*). Flow-rate-dependent dripping (II) occurs when the oil thread blocks the constriction channel, and the subsequent build-up of the outer liquid pressure (water) leads to breakup at the junction (*squeezing*). Three sub-regimes i, ii and iii can be distinguished, as will be explained in section 4.3.2. Jetting (III) occurs when the outer liquid (water) shears the oil thread in the constriction channel, leading to breakup downstream from the junction (*shearing*). Threading (V) occurs at high shear conditions where viscous stress and interfacial tension are balanced. In the dripping and jetting flow regimes, after the generation of the first droplet, the oil phase flows as droplets and the water phase flows

as segments between oil droplets and water films. The geometry-determined and flow-rate-dependent regimes correspond to a droplet formation which is determined by the channel geometry and the flow rates of two phases, respectively.

4.3.1. Geometry-determined dripping - capillary instability

(τ_σ driven breakup at the junction: j)

In our two-phase flow devices, at low flow rates, the hydrostatic pressure from the syringe pump pushes the oil phase slowly to advance into the constriction channel, and thus restricts the water flow to a thin film at the walls and a flow in the corners. An oil thread advances along the constriction channel towards the outlet channel; its tip is separated by a short water slug from the previous thread. The long oil thread in the constriction channel acts as a leaky piston, which is different from the situation in a circular capillary [22, 23]. In a hydrophilic channel with rectangular cross section, at small Ca , the oil phase is separated from the wall by a thin film and each corner by a meniscus which has the same curvature as the cap [22, 24]. The water phase can either bypass through the corners (corner flow) or drag the oil via the film (film flow).

The corner flow dominates at extremely low flow rates [22-24]. Fig. 4.4a shows a typical droplet formation sequence in this flow regime. We plot the oil tip position (χ) in the constriction channel with respect to the junction versus time (t) at two different flow rates in Fig. 4.4b and the water segment length (l_w) versus time in the constriction channel in Fig. 4.4c. The slopes of the rectangular and circular dot lines in Fig. 4.4b are 3.65×10^{-4} m/s and 7.06×10^{-4} m/s on average. The calculated oil flow velocity is 3.33×10^{-4} m/s and 6.67×10^{-4} m/s when Q_o is 2×10^{-3} $\mu\text{L}/\text{min}$ and 4×10^{-3} $\mu\text{L}/\text{min}$, respectively. The measured flow velocities in the constriction channel are therefore approximately equal to the single pumping oil flow velocity. Since we kept the oil-to-water flow ratio constant most water must flow through the corners without shearing the oil in the constriction channel (significant shearing would cause breakup in the junction area). Furthermore, it can be seen from Fig. 4.4c that the water segment length increases with time. This means that the water is transported faster by the corner flow

than the oil thread due to the cross-sectional shape [24, 25]. As a result, we experimentally prove that the corner flow predominantly transports water in this region where the water pressure work is dissipated predominantly by the motion in the corners.

Furthermore, in the regime of low Ca , the influence of viscous pressure drop can be neglected. This can be verified explicitly by comparing the calculated hydrodynamic pressure drop ΔP_H ($O(10Pa)$) at a flow rate of $10^{-4} \sim 10^{-3} \mu\text{L}\cdot\text{min}^{-1}$ to the characteristic Laplace pressure ΔP_L ($O(10^4 Pa)$) in the system. Hence, under these conditions, the quasi-static oil-water interface has to obey the constraint of constant mean curvature along the entire oil thread. The interfacial force is therefore approximately equal to the hydrostatic pressure difference across the interface; and the total pressure across the oil-water interface $P \approx 0$ along the entire oil thread. However, as the oil thread front reaches the end of the constriction channel the oil thread heads from the shallow constriction channel into the wide outlet channel. The channel width suddenly changes from w to W , which results in a decrease of τ_σ . As a result, the oil tip expands, sucking the oil flow from the constriction into the outlet channel. The resulting increased oil flow rate will cause the oil thread at the junction to shrink. The increase of the interfacial curvature (force) at the junction finally leads to breakup of the oil thread at the junction to form a droplet. (Note: the two liquids therefore flow in parallel along the constriction channel. This would be considered as threading flow if there were no step in the design [11].) After breakup the disconnected droplets flow downstream, while the oil thread retracts into the oil phase inlet channel. The process subsequently restarts. The breakup time is negligible compared to the long spreading time. The droplet volume is therefore approximately equal to the volume of the constriction channels.

The experimental results coincide well with the theoretical values thus expected (Table 4.2). The slight deviation for the small constriction channel may be due to the calculating method since the droplets were not fully disk-like in the outlet channel. It turns out that the final droplet volume is in fact given almost exactly by the volume of the constriction channel provided that the latter is sufficiently long. (see also chapter 5)

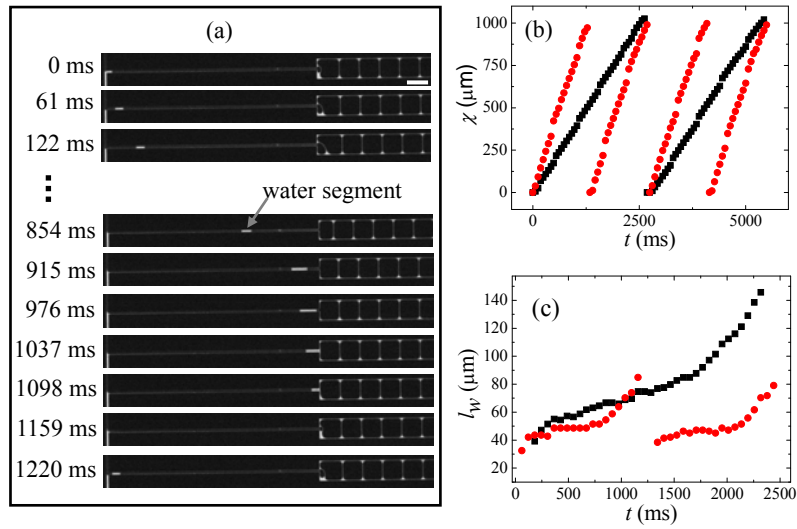


Figure 4.4 (a) Sequential snapshots of a cycle of droplet formation (oil appears as black and water as white) at $Q_{oil} = Q_{water} = 4 \times 10^{-3} \mu\text{L/min}$, $l = 1000 \mu\text{m}$ and $w = h = 10 \mu\text{m}$, (b) the plot of the oil tip position with respect to junction versus time at two different oil flow rates: $\blacksquare 2 \times 10^{-3} \mu\text{L/min}$ and $\bullet 4 \times 10^{-3} \mu\text{L/min}$, and (c) the plot of the water segment length versus time at two different oil flow rates: $\blacksquare 2 \times 10^{-3} \mu\text{L/min}$ and $\bullet 4 \times 10^{-3} \mu\text{L/min}$. The water segment length is considered to be 0 when it reaches the wide outlet channel.

Table 4.2 Comparison of the constriction channel volume with the measured droplet volume in the geometry-determined dripping regime

Constriction channel volume(nL)	Measured droplet volume(nL)*
0.08	0.0681
0.16	0.1611
0.32	0.3211
0.01	0.0104
0.10	0.0930

*Each measured droplet volume is obtained by averaging 10 droplets volume.

4.3.2. Flow-rate-dependent dripping - squeezing

(P_{hyd} driven breakup at junction)

As the water flow rate increases, the oil thread breaks in the junction before the emerging oil thread tip reaches the wide outlet channel. This occurs above a certain threshold flow rate. The droplet size decreases when the imposed water flow rate increases and the oil flow rate decreases in the same microfluidic device. We will explain the droplet generation mechanism as “squeezing”, prior described by Garstecki et al [26-28]. The droplet formation in this regime can be divided into five stages, as shown in Fig. 4.5: (i) the oil tip first intrudes at the junction, (ii) the oil tip grows and blocks almost the entire cross section of the constriction channel, (iii) the water squeezes the oil thread at the junction, (iv) the oil thread starts to break at the junction, and (v) an oil droplet detaches from the oil thread, and the oil thread retracts.

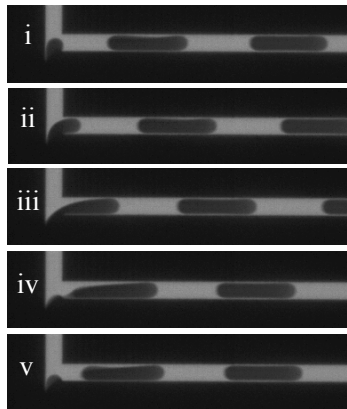


Figure 4.5 Squeezing dynamics: time series of a cycle of droplet formation at the junction: i – entering, ii - blocking, iii – squeezing, iv – breaking and v – detaching.

The oil thread slowly blocks the cross section of the constriction channel after entering, and because the shear stresses exerted on the tip by the water phase are not strong enough to deform the tip, the water is confined to flow in a film through the corners and the gap between the oil thread and the channel walls. The flow in the film

leads to a build-up of pressure in water phase upstream of the tip. When the build-up pressure is larger than the pressure in the oil tip ($P_j < 0$) the water starts to squeeze the neck of the oil thread. The squeezing will lead to the breakup of the oil tip and the detachment of a droplet from the oil thread.

The volume of a generated droplet (V) is proportional to the breakup time t_b (the time interval during which the immiscible thread is open), multiplied by the inner liquid (oil) flow rate (Q_o) in the same device: [6, 29] $V = Q_o t_b$. The experiments show that the water film thickness λ is negligible in comparison to the channel width in a range of intermediate flow rates. The cross-sectional area of oil and water phases is then constant in the same channel. The “squeezing” displacement speed of water to oil is thus proportional to the water flow rate [26-28]. The breakup time: $t_b \propto \frac{1}{Q_w}$, thus at

these flow rates $V = t_b Q_o \propto \frac{Q_o}{Q_w}$, the droplet volume is proportional to the oil-to-water

flow rate ratio. In our experiments the flow rate ratio was kept constant, and the squeezing mechanism would therefore lead to a constant droplet volume. We indeed observed such behavior over approximately 1 order of magnitude of flow rate (subregime ii in Fig. 4.6a). This regime in which the droplet size is independent of flow rate at constant flow ratio is similar to previous reported regimes in T-junction and FFD devices [26-28].

When we looked at the detail of the plot (Fig. 4.6a) of the droplet volume as a function of total flow rate ($Q_{tot} = Q_o + Q_w$) at constant ε in this regime II, we found two flow ratio-dependent subregimes (i, iii) before and after that of subregime (ii), as capillary numbers also approximately indicated in Fig. 4.3a. The reason why subregime (i) exists is still not clear. The existence of subregime (iii) could be explained by the incipient shearing of water phase at higher flow rates [30]. In this regime, we observed that the oil thread only partially blocks the constriction channel. The breakup time t_b is therefore mainly determined by the time the oil tip travels from the inlet to the breakup point, which implies that t_b is a function of both Q_o and Q_w . Thus droplet volume V is

not proportional to ε in this subregime (iii). Depending on the flow rate ratio, this narrow regime is relatively wide or narrow: wide at low ε and narrow at high ε .

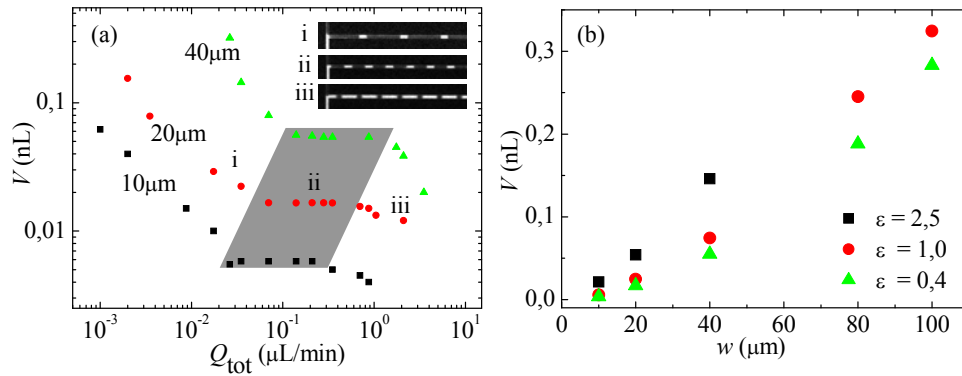


Figure 4.6 Flow-rate-dependent dripping: (a) droplet volume as a function of Q_{tot} in three different devices with $h = 10 \mu\text{m}$, $l = 400 \mu\text{m}$, $w = 10, 20$ and $40 \mu\text{m}$ at $\varepsilon=1$. Inserts show different flow patterns observed in the three subregimes observed; (b) droplet volume as a function of constriction channel width at different flow rate ratios in subregime ii.

At the same squeezing speed, t_b is proportional to the squeezing distance ($w-2\lambda$): $t_b \propto (w-2\lambda)$. We therefore also investigated the influence of geometry on droplet volume by varying the constriction channel width (w) from $10 \mu\text{m}$, $20 \mu\text{m}$, $40 \mu\text{m}$, $80 \mu\text{m}$ to $100 \mu\text{m}$ in regime (ii). The droplet volume as a function of constriction channel width is shown in Fig. 4.6b, and it can be seen that the droplet volume increases with the constriction channel width.

4.3.3. Flow-rate-dependent jetting - shearing

(τ_v driven breakup downstream from the junction)

As the capillary number is further increased, the oil thread breakup point moves progressively downstream, and a jet in the constriction channel is formed (as seen in

Fig. 4.3). This transition experiences an intermediate regime as flow rate increases, where the growing droplets move downstream while still connected to the fluid in the tip through a fluid neck (Fig. 4.7b). Finally, a clear jetting regime is obtained, where the oil thread does not break at the junction but at the tip away from the junction downstream in the constriction channel (Fig. 4.7c).

We follow the main line of the theoretical explanation for the transition due to the force the water phase exerts on the emerging oil thread. In the squeezing regime II, the oil thread blocks the constriction channel and the increasing water pressure subsequently breaks the oil thread. In the junction area, the interface however also experiences a viscous force stretching the oil thread downstream decreasing the oil thread width and preventing buildup of pressure in the water phase and hence squeezing. When the interfacial tension is balanced by viscous forces, the oil thread travels downstream until breakup occurs at its tip where the stress gradient across the jet relaxes. (Droplets do not form at the junction where $P_j \approx 0$ but form when the force balance is broken at the thread tip where $P_{tip} < 0$). The dripping to jetting transition can therefore be induced by increasing flow speed to increase the viscous forces [15, 21], see Fig. 4.7. The droplet size can be theoretically approximated by equating viscous stress and interfacial tension [30].

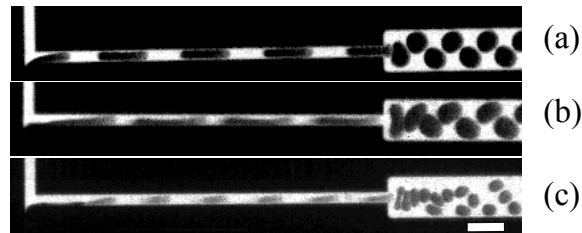


Figure 4.7 Jetting induced by increasing flow speed: (a) $Q_o = 0.1 \mu\text{L}\cdot\text{min}^{-1}$, $Q_w = 0.05 \mu\text{L}\cdot\text{min}^{-1}$, (b) $Q_o = 0.3 \mu\text{L}\cdot\text{min}^{-1}$, $Q_w = 0.15 \mu\text{L}\cdot\text{min}^{-1}$, and (c) $Q_o = 0.5 \mu\text{L}\cdot\text{min}^{-1}$, $Q_w = 0.25 \mu\text{L}\cdot\text{min}^{-1}$. The scale bar is $100 \mu\text{m}$.

4.3.4. Geometry-determined jetting - capillary instability

(τ_σ driven breakup in the step area: s)

As mentioned above, the relaxation of stress gradient induces the breakup of the oil thread tip droplets due to the interfacial instability. In the head-on microfluidic circuit, there is a geometrical step change (s) between the narrow constriction channel and the wide outlet channel. Fluid dynamics changes when water and oil flow together through this geometrical step change. At low oil and water flow rates (regime I) it was seen that that the resulting drop in interfacial tension caused a breakup of the oil thread downstream at the junction area. At increasing oil flow rate, breakup instead was seen to occur at the step area. We explain this by the increased oil supply rate, preventing a sufficient pressure drop at the junction for breakup. Now the decreasing oil pressure on droplet expansion leads to a local thinning of the oil thread and breakage at the step area. In the head-on devices there therefore exists a specific geometry-determined capillary instability regime (Fig. 4.8), which is different from other reported regimes [10, 11].

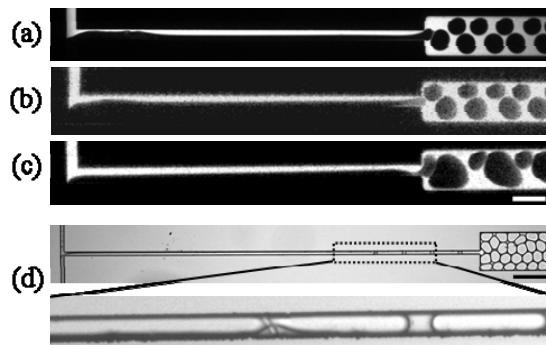


Figure 4.8 (a-c) Geometry-determined capillary instability. (d) Capillary instability droplet formation induced by an obstruction in the microchannel. The scale bars are 100 μm .

The flow in this capillary-instability regime is sensitive to changes in flow speed or geometry. Bifurcations in the droplet-size were for example observed as shown in Figs. 4.8(a-c). This sensitivity is understandable since the oil thread is not confined by the walls as in regime I and hence easily becomes unstable. This process could also be expressed in another way as breakup of an oil thread tip induced by a step change in geometry [31]. A local obstruction in the channel acts as another type of step change which can also lead to a capillary instability, as shown in Fig. 4.8d, the oil and water continuously flow in the constriction channel before they arrive at the obstruction, the geometrical change, where the oil thread tip starts to drip.

4.3.5. Threading

(τ_v driven, no breakup)

Finally, a threading regime is observed where water and oil phases flow parallel to each other both in constriction and outlet channels. The inner more viscous oil liquid is focused and encapsulated by the water phase in the center of the constriction and outlet channels. This behavior is obtained by further increasing the water or oil flow rates to the point where the dynamic pressure difference overcomes both the interfacial forces and the geometrically induced pressure change. The viscous force of the water phase drags the interface straight downstream, and the pressure in the oil phase keeps the thread flow continuous. Therefore, no droplet formation was observed in the view field as defined before. The significant shape differences between the threads shown in Fig. 4.9 are due to the large flow speed difference between the oil and water phases in the different cases. The transition to this regime is not sudden but experiences an intermediate regime where the oil-water interface undulates but does not break. A smooth threading flow is sustained at higher flow rates.

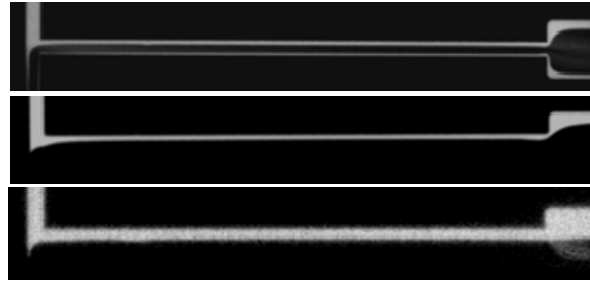


Figure 4.9 Threading in head-on microfluidic channels. Top: $Q_w = 0.5Q_o = 0.5 \mu\text{L}\cdot\text{min}^{-1}$; middle: $Q_w = Q_o = 0.75 \mu\text{L}\cdot\text{min}^{-1}$; and bottom, $Q_w = 2Q_o = 1 \mu\text{L}\cdot\text{min}^{-1}$.

4.4 Conclusions and Outlook

Oil and water two-phase flow in head-on devices is investigated. Different flow regimes are observed in the broad range of flow rates which could be investigated due to the stable, hard and impermeable wall material. Over a broad range of capillary numbers, $Ca \in (10^{-6}, 10^{-1})$, a two-phase flow diagram shows different flow sensitivity in different flow regions. We have provided a theoretical framework to understand the different mechanisms by considering the different forces acting in the system. At extremely low flow rate, we find that droplet size is exclusively determined by the device geometry (especially the constriction channel dimensions). Droplet formation in this regime (I) is by *capillary instability*. At higher flow rates, a flow-rate-dependent *squeezing* regime (II) shows three sub-regimes at a constant flow rate ratio: the droplet size first decreases with increasing flow rate (i), then goes to a regime (ii) where the droplet size is insensitive to the flow rate, while a further flow rate increase leads to a nonlinear and flow-rate sensitive transition regime (iii). Jetting (III) behavior caused by *shear* forces can be obtained by increasing of flow rate. A second *capillary instability* determined regime (IV) was obtained in a narrow flow rate range. Finally the flow reaches a threading regime (V) where the two phases flowed parallel to each other

along both the constriction channel and the outlet channel. This device provides us with the choice to generate droplet-based flow in the regimes that are determined either by flow-rate or device geometry.

References

- [1] B. Zheng, J. D. Tice, R. F. Ismagilov, *Anal. Chem.* **2004**, *76*, 4977.
- [2] B. Zheng, J. D. Tice, L. S. Roach, et al., *Angew. Chem. Int. Ed.* **2004**, *43*, 2508.
- [3] T. Pfohl, F. Mugele, R. Seemann, et al., *ChemPhysChem* **2003**, *4*, 1291.
- [4] L. Shui, J. C. T. Eijkel, A. van den Berg, **2007**, *133*, 35.
- [5] A. Gunther, K. F. Jensen, *Lab Chip* **2007**, *7*, 399.
- [6] P. Garstecki, G. M. Whitesides, H. A. Stone, *Phys. Rev. Lett.* **2005**, *94*, 1645011.
- [7] H. A. Stone, A. D. Stroock, A. Ajdari, *Annu. Rev. Fluid Mech.* **2004**, *36*, 381.
- [8] E. Berthier, D. J. Beebe, *Lab Chip* **2007**, *7*, 1475.
- [9] L. Shui, J. C. T. Eijkel, A. van den Berg, *Adv. Colloid Interfac.* **2007**, *133*, 35.
- [10] A. S. Utada, A. Fernandez-Nieves, H. A. Stone, et al., *Phys. Rev. Lett.* **2007**, *99*.
- [11] T. Cubaud, T. G. Mason, *Phys. Fluids.* **2008**, *20*.
- [12] P. Garstecki, M. J. Fuerstman, H. A. Stone, et al., *Lab Chip* **2006**, *6*, 437.
- [13] P. Garstecki, I. Gitlin, W. DiLuzio, et al., *Appl. Phys. Lett.* **2004**, *85*, 2649.
- [14] J. D. Tice, H. Song, A. D. Lyon, et al., *Langmuir* **2003**, *19*, 9127.
- [15] J. D. Tice, A. D. Lyon, R. F. Ismagilov, *Anal. Chim. Acta.* **2004**, *507*, 73.
- [16] T. Thorsen, R. W. Roberts, F. H. Arnold, et al., *Phys. Rev. Lett.* **2001**, *86*, 4163.
- [17] J. M. Gordillo, Z. D. Cheng, A. M. Ganan-Calvo, et al., *Phys. Fluids* **2004**, *16*, 2828.
- [18] S. L. Anna, N. Bontoux, H. A. Stone, *Appl. Phys. Lett.* **2003**, *82*, 364.
- [19] R. Dreyfus, P. Tabeling, H. Willaime, *Phys. Rev. Lett.* **2003**, *90*, 1445051.
- [20] P. Garstecki, M. J. Fuerstman, G. M. Whitesides, *Phys. Rev. Lett.* **2005**, *94*, 2345021.
- [21] A. M. Ganan-Calvo, P. Riesco-Chueca, *J Fluid Mech* **2006**, *553*, 75.
- [22] H. Wong, C. J. Radke, S. Morris, *J. Fluid Mech.* **1995**, *292*, 95.
- [23] H. Wong, C. J. Radke, S. Morris, *J. Fluid Mech.* **1995**, *292*, 71.
- [24] A. Mazouchi, G. M. Homsy, *Phys. Fluids* **2001**, *13*, 1594.
- [25] E. Lajeunesse, G. M. Homsy, *Phys. Fluids* **2003**, *15*, 308.
- [26] P. Garstecki, M. J. Fuerstman, H. A. Stone, et al., *Lab Chip* **2006**, *6*, 437.
- [27] P. Garstecki, G. M. Whitesides, H. A. Stone, *Phys. Rev. Lett.* **2005**, *94*, 1645011.
- [28] J. H. Xu, G. S. Luo, S. W. Li, et al., *Lab Chip* **2006**, *6*, 131.
- [29] B. J. Adzima, S. S. Velankar, *J. Micromech. Microeng.* **2006**, *16*, 1504.
- [30] M. De Menech, P. Garstecki, F. Jousse, et al., **2008**, *595*, 141.
- [31] C. Priest, S. Herminghaus, R. Seemann, *Appl. Phys. Lett.* **2006**, *88*, 024106.

Chapter 5

Geometry-Controlled Droplet Generation in Head-on Microfluidic Devices

We investigated the generation of droplets in a head-on microfluidic device operated with the two identical channels as inlets and the “long leg” as a constriction channel leading to a wider outlet section. For capillary numbers (Ca) of approximately 10^{-5} or less, we find a Ca -independent droplet volume equal to the volume of the constriction channel, which decreases at higher Ca when shear forces become relevant. The droplet generation mechanism is explained in terms of a global capillary instability involving surprisingly stable intermediate surface configurations.

This chapter was published in *Applied Physics Letters*, 93: 1531131-153113 (2008).

5.1 Introduction

Droplet-based multiphase microfluidics is rapidly becoming an important area in microfluidics with many possible applications for chemical and biological purposes [1-7]. The creation of monodisperse droplets is one of the most important requirements for many of these applications. The most commonly used geometries for two-phase flow are T-junctions [8-11] and flow-focusing devices (FFD) [12-14]. Experiments have mostly been performed in microchannels fabricated in PDMS where water droplets in oil phase were obtained due to the hydrophobicity of PDMS. However, the permeability and deformability of PDMS prevents investigators from using extremely low or high flow rates. Generally, flow rates corresponding to capillary numbers (Ca) of 10^{-3} ~1 have been investigated [9, 15]. ($Ca = \eta v/\sigma$, where η and v are the viscosity and average flow velocity of the continuous phase, respectively, and σ is the interfacial tension [10, 16].) Microfluidic droplet generation is therefore affected by shear forces in these geometries under these conditions.

In the present chapter, we are interested in droplet generation at extremely low Ca numbers in “head-on devices” consisting of two identical channels as inlets and the “long leg” as a constriction channel leading to a wider outlet section, as shown in Fig. 5.1.

5.2 Experimental

Microchannels were fabricated in silicon-glass using standard photolithography with homogeneous and regular cross sections. Chips were placed in a home-made chip-holder which can easily be connected to gas-tight syringes (Hamilton) using nanoport connectors (Upchurch Scientific). Water (DI water with 0.01M sodium dodecyl sulfate (SDS) and 0.01M fluorescein sodium salt, $\eta_w = 10^{-3}$ Pa.s) and oil (hexadecane, $\eta_o = 3 \times 10^{-3}$ Pa.s) phases were pumped using a syringe pump (Harvard PHD 22/2000). The water-hexadecane interfacial tension with SDS is 0.01 N.m^{-1} . Flow rates (Q) were varied between 10^{-3} ~1 $\mu\text{L}/\text{min}$ corresponding to $Ca = 10^{-7}$ ~ 10^{-3} . Water flows as

continuous phase and oil as dispersed phase due to the channel hydrophilicity. The flow was visualized using an inverted microscope (Leica DMIRM) and recorded by using a CCD camera (Orca ER).

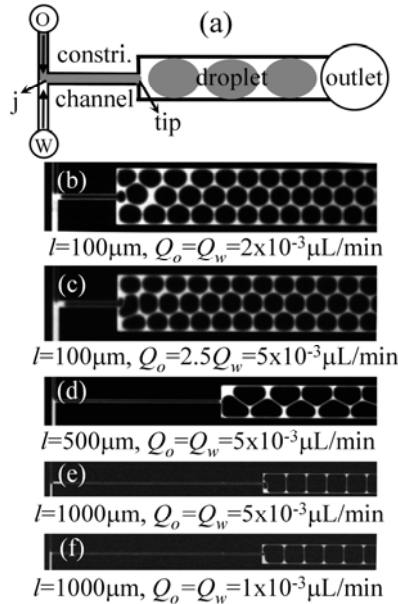


Figure 5.1 (a) Sketch of the head-on configuration. j and tip indicate junction and oil tip areas, respectively. The channel depth (h) is either 10 or 20 μm . Outlet channel width (W) is 100 μm . Two identical inlet channels are $10 \times 10\mu\text{m}$ or $20 \times 20\mu\text{m}$. Constriction channels lengths (l) are 100, 400, 500 or 1000 μm , and widths (w) are 10, 20 or 40 μm . (b-f) Snapshots of the geometrically induced droplet formation in different devices and at different flow rate and flow rate ratios.

5.3 Results and Discussion

Fig. 5.2 illustrates the typical droplet formation process. An oil thread advances along the constriction channel towards the outlet region. Its tip is separated by a short (bright) water slug from the previous thread. The oil thread is separated from the channel walls

by the continuous water phase. The presence of the water is clearly visible at the edges of the channel, where a wetting corner film gives rise to enhanced fluorescence signal in the pictures. As the oil thread advances, its cross-sectional shape remains constant from the junction area to the tip. In the junction area, an oil-water interface with a constant in-plane curvature of order $2/w$ connects the oil in the inlet channel to the oil thread in the constriction channel. Once the tip reaches the wider outlet channel, it expands and begins to form a droplet. Nearly simultaneously, the oil thread in the junction area becomes thinner and thinner and eventually breaks. Subsequently, the rest of the now disconnected thread advances through the constriction channel and produces the droplet. Fig. 5.3a and Fig. 5.3b show the volume (V) of the droplets formed in this manner for several channel geometries as a function of Ca . It turns out that V is independent of Ca below a certain channel-dependent threshold value Ca_c . The final droplet volume is thereby almost exactly given by the volume of the constriction channel provided that the latter is sufficiently long. This is demonstrated in Fig. 5.3c where we plotted the obtained droplet volume (experimental results) in units of the constriction channel volume (theoretical values). The droplet volume is thus determined in a very robust fashion by the design of the channel geometry.

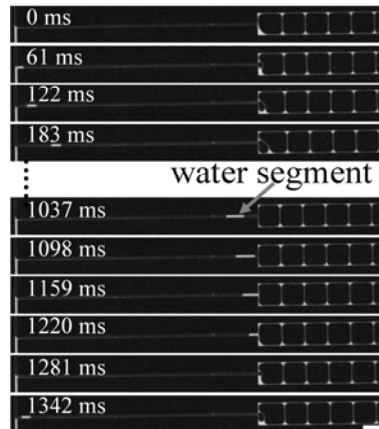


Figure 5.2 The process of droplet generation: $h = 10 \mu\text{m}$, $w = 10 \mu\text{m}$ and $l = 1000 \mu\text{m}$. The scale bar is $100 \mu\text{m}$.

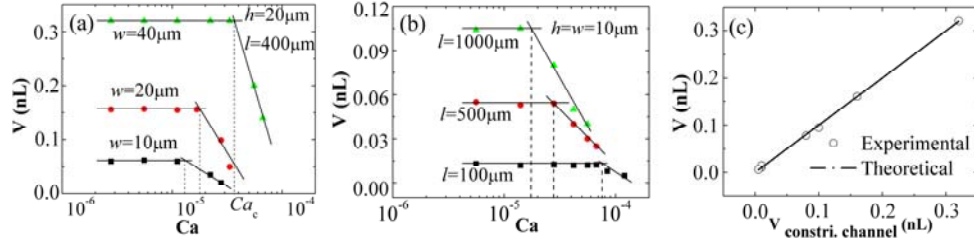


Figure 5.3 V versus Ca in different devices: (a) varied w at $h = 20 \mu\text{m}$ and $l = 400 \mu\text{m}$, and (b) varied l at $h = w = 10 \mu\text{m}$. The dash lines indicate Ca_c . Here $Q_w = Q_o$. (c) V versus $V_{\text{constr. channel}}$ (theoretical constriction channel volume) in different devices.

We now focus on two aspects of the process described above: (i) the flow pattern of the co-flowing oil and water phases and (ii) the stability and breakup mechanism of the oil phase in the junction area.

Let us first consider the flow regime. Operating in the regime of low Ca we expect viscous forces to be negligible. This can be verified explicitly by comparing the hydrodynamic pressure drop ΔP_{hy} in the system to the characteristic Laplace pressure ΔP_L , which is of order σ/w . Assuming laminar flow, the pressure drop following Hagen-Poiseuille can be simply expressed as $\Delta P_{\text{hy}} \approx \eta L Q / d^4$, with L the length of the emerging droplet and d a characteristic dimension [17]. Inserting typical numbers we find that $\Delta P_{\text{hy}} = O(10 \text{ Pa})$, while, $\Delta P_L = O(10^4 \text{ Pa})$. Hence, the viscous pressure drop can indeed be neglected. Under these conditions, the quasi-static oil-water interface has to obey the constraint of constant mean curvature.

Since the mean curvature of the tip of the oil thread is given by $\kappa_{\text{tip}} = (2/h + 2/w)/2$, the cross-sectional area of the oil thread behind the tip has to be of rectangular shape with rounded corners [18-21] (see Fig. 5.5), with the curvature in the corners (κ_{corn}) corresponding to the tip curvature (κ_{tip}), $\kappa_{\text{corn}} = \kappa_{\text{tip}}$. (Between these rounded corners there will be a microscopically thin water film at very low flow rate

($Ca^{2/3} \ll 1$), which we neglect for the purposes of this work.) The water flows parallel with the oil thread, in the corners taking a fillet shape. Apart from generating fluorescence along the channel edge, the presence of the co-flowing water manifests itself also in both the speed of the advancing oil tip as well as the size of the water slugs separating two consecutive oil threads in the constriction channel: the oil thread tip moves typically about 10% faster than expected if based on the volume flow rate with the simple single phase Poiseuille flow for a rectangular channel. The length of the water slug is found to increase as it travels down the constriction channel, showing that the continuous phase flows past the oil thread like in a leaky piston [22-24]. These observations are in line with the imposed water flow rate and the requirement of volume conservation, as indicated earlier by others.

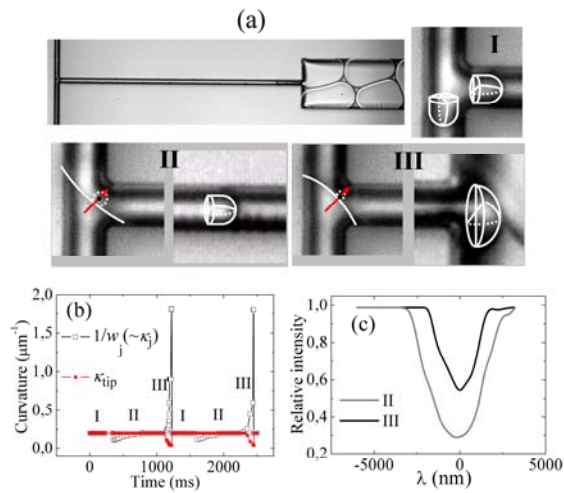


Figure 5.4 (a) The shapes of the oil thread in the junction and tip areas at different stages, visualized in transmitted light. (b) The mean curvature of the oil thread in the junction ($\kappa_j \approx 1/w_j$, w_j is the smallest oil thread width across the junction) and tip (κ_{tip}) areas versus time, $h = 10 \mu\text{m}$, $w = 10 \mu\text{m}$ and $l = 500 \mu\text{m}$. (c) The fluorescence intensity profile measured across the oil thread center in the junction area at stages II and III (red arrows). λ is the distance to the oil thread center. Intensity values are in arbitrary units normalized to the

fluorescent intensity in the water inlet channel.

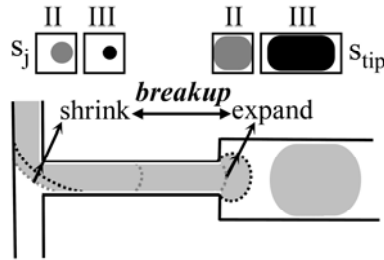


Figure 5.5 Schematic of the droplet formation mechanism in stage II and III. Cross sections through the oil thread in the junction area (S_j) at its narrowest point and through the oil tip at its widest point (S_{tip}) are sketched. Measurements (Fig. 5.4) indicate the detachment of the oil thread from the confining walls and its narrowing in stage III.

What determines the breakup of the capillary bridge in the junction area and its stability prior to breakup? Fig. 5.4a shows the typical evolution of the oil thread in the junction and tip areas in a device where $w = h = 10\mu\text{m}$. As discussed above, the oil-water interface has a constant mean curvature - given by κ_{tip} - at all times (except immediately prior to pinch off). In the junction area, a transient stage I occurs in the beginning when the oil bulges into the water channel (Fig. 5.4aI) giving a local mean curvature equals to κ_{tip} . When stage II commences the oil retreats to form a thread running through the junction area. In stages II and III the in-plane curvature (solid line) is negligible compare to the out-of-plane curvature (dotted line), as shown in Fig. 5.4aII. The mean curvature in the junction area can then be approximated by the local oil thread width: $\kappa_j \approx 1/w_j$. Open squares and solid circles in Fig. 5.4b compare $1/w_j$ ($\sim \kappa_j$) in stage II and III with κ_{tip} . As expected $1/w_j$ is equal to κ_{tip} most of the time while the oil thread advances along the constriction channel ($\sim 0.7\text{s}$ for the data shown here), except for a short phase between stage I and II, when the in-plane curvature can not be neglected. The equality of $1/w_j$ ($\sim \kappa_j$) and κ_{tip} in stage II implies that $w_j = h/2$. To retain a circular cross-section means that the oil thread is detached from the channel walls. This is indeed confirmed by the fluorescence profile as measured across the oil thread in the

junction area (Fig. 5.4c).

At first glance, one might be surprised that such a thin thread is stable for such a long time since it should break up within approximately 0.01~0.1s following the Rayleigh Plateau instability scenario. However, unlike the classical Rayleigh Plateau instability, the oil thread in our present experiments is not part of a free jet but connected to the oil threads in the inlet and the constriction channels, respectively. The channel wall confinement now stabilizes the thin oil thread in the junction area [25] (see Fig. 5.5). Once the tip reaches the wider outlet region (stage III), it expands as described above, leading to a sudden decrease of the local pressure. Owing to the finite imposed oil flow rate and the hydrodynamic resistance in the junction area, this leads to the breakup of the oil thread in this area. The breakup process takes between 10 and 100ms, depending on the cross-section of the constriction channel and the flow rate. During that time, liquid still flows from the inlet channel through the junction into the forming droplet. As a consequence, the final droplet volume is slightly larger than the constriction channel volume.

5.4 Conclusions and Outlook

In summary, we found that the generation of oil droplets in a “head-on” two-phase microfluidic device for Ca numbers of 10^{-5} and less is controlled by the geometry of the device and the resulting Laplace pressure. Confinement due to the channel walls leads to the stabilization of otherwise unstable liquid morphologies.

References

- [1] A. v. d. Berg, T. S. J. Lammerink, *Top. Curr. Chem.* **1998**, 21.
- [2] L. Shui, J. C. T. Eijkel, A. van den Berg, *Adv. Colloid Interfac.* **2007**, 133, 35.
- [3] B. Zheng, J. D. Tice, L. S. Roach, et al., *Angew. Chem. Int. Ed.* **2004**, 43, 2508.
- [4] M. W. Losey, R. J. Jackman, S. L. Firebaugh, et al., *J. Microelectromech. Syst.* **2002**, 11, 709.
- [5] J. Tien, C. M. Nelson, C. S. Chen, *PNAS* **2002**, 99, 1758.
- [6] D. Sinton, *Microfluid. Nanofluid.* **2004**, 1, 2.
- [7] A. Gunther, K. F. Jensen, *Lab Chip* **2007**, 7, 399.
- [8] J. D. Tice, A. D. Lyon, R. F. Ismagilov, *Anal. Chim. Acta.* **2004**, 507, 73.

-
- [9] P. Garstecki, M. J. Fuerstman, H. A. Stone, et al., *Lab Chip* **2006**, 6, 437.
- [10] J. D. Tice, H. Song, A. D. Lyon, et al., *Langmuir* **2003**, 19, 9127.
- [11] T. Thorsen, R. W. Roberts, F. H. Arnold, et al., *Phys. Rev. Lett.* **2001**, 86, 4163.
- [12] F. Malloggi, S. A. Vanapalli, H. Gu, et al., *J Phys-Condens Mat* **2007**, 19.
- [13] S. L. Anna, N. Bontoux, H. A. Stone, *Appl. Phys. Lett.* **2003**, 82, 364.
- [14] P. Garstecki, I. Gitlin, W. DiLuzio, et al., *Appl. Phys. Lett.* **2004**, 85, 2649.
- [15] P. Garstecki, G. M. Whitesides, H. A. Stone, *Phys. Rev. Lett.* **2005**, 94, 1645011.
- [16] B. Zheng, J. D. Tice, R. F. Ismagilov, *Anal. Chem.* **2004**, 76, 4977.
- [17] A. Aota, A. Hibara, T. Kitamori, *Anal. Chem.* **2007**, 79, 3919.
- [18] V. S. Ajaev, G. M. Homsy, *J. Colloid Interface Sci.* **2001**, 244, 180.
- [19] V. S. Ajaev, G. M. Homsy, *J. Colloid Interface Sci.* **2001**, 240, 259.
- [20] H. Wong, C. J. Radke, S. Morris, *J. Fluid Mech.* **1995**, 292, 95.
- [21] H. Wong, C. J. Radke, S. Morris, *J. Fluid Mech.* **1995**, 292, 71.
- [22] A. Mazouchi, G. M. Homsy, *Phys. Fluids* **2001**, 13, 1594.
- [23] E. Lajeunesse, G. M. Homsy, *Phys. Fluids* **2003**, 15, 308.
- [24] V. van Steijn, M. T. Kreutzer, C. R. Kleijn, *Chem. Eng. Sci* **2007**, 62, 7505.
- [25] *We rationalize the stabilization as follows. The fastest growing unstable modes in the classical Rayleigh plateau instability distribute the liquid only on a local scale, i.e., they would force liquid from the junction area into the entrance of the adjacent constriction channel. Such a perturbation, however, would experience a restoring force because it requires forcing the liquid-liquid interface further into the corners. As a consequence, such perturbations are no longer unstable and the breakup can only occur through slower nonlocal perturbations. Note that this picture is also different from the convective stabilization of confined jets discussed by P. Guillot, Phys. Rev. Lett. 99, 104502 (2007) operated at much higher Ca.*

Chapter 6

Interfacial Tension Controlled W/O and O/W 2-Phase Flow in Microchannels

In microfluidic systems, interfacial tension plays a predominant role in determining the two-phase flow behavior due to the high surface area to volume ratio. We investigated the influence of both solid-liquid (σ_{SL}) and liquid-liquid (σ_{LL}) interfacial tensions on water-oil two-phase flows in microfluidic devices. Experimental results show that, unlike macroscopic systems, σ_{SL} plays a dominant role, determining the emulsion type created in microchannels: oil-in-water (O/W) flow in hydrophilic microchannels and water-in-oil (W/O) flow in the corresponding hydrophobically treated microchannels. Modification of σ_{LL} by surfactants only plays a secondary role. By tuning σ_{LL} , oil-water two-phase flow patterns could be changed from droplet-based to stratified flows under constant flow conditions in the same device. In addition, also droplet deformation, coalescence and emulsion inversion could be achieved by tailoring σ_{SL} and σ_{LL} in microfluidic devices. Microfluidic technology therefore provides a valuable additional tool for quantitatively manipulating and evaluating these phenomena which are difficult to realize in the macroscale devices.

This chapter was published in *Lab on Chip*, 9: 795-801 (2009).

6.1 Introduction

An emulsion is a mixed system (water and oil) in which one phase (referred to as the dispersed phase) is suspended in the other one (referred to as the continuous phase) as small droplets. The basic simple emulsion types are water-in-oil (W/O) and oil-in-water (O/W). In terms of (technological) applications, emulsions are vital in our daily life. Food, cosmetic, pharmaceutical and oil industries need to control emulsion properties, such as emulsion type, viability and stability, to obtain the desired products [1-3]. However, an emulsion produced by simply mixing oil and water without adding any surfactant is not stable and will quickly revert to the two individual phases. Emulsifiers such as surfactants are used to create stable emulsions; where their function is to decrease interfacial tension in order to reduce the mixing energy and to generate stable interfaces between the two phases. Emulsification is typically not a spontaneous process, but extra energy needs to be supplied for instance by stirring, shaking, spraying or sonication. Recently, microfluidic technology has become an alternative reliable method to create controlled and monodisperse emulsions [4-6]. When device dimensions shrink to the micrometer scale, surface-to-volume ratio greatly increases, and consequently the interfacial tensions are found to have a dramatic effect on the multiphase flow phenomena. The manipulation of the interfacial tension (solid-liquid, liquid-liquid) is currently becoming a very important aspect in the trend toward miniaturization.

The liquid-liquid interfacial properties are usually be tuned by applying surfactants. A typical surfactant (or surface active agent) molecule consists of a hydrophilic head and a hydrophobic tail (Fig. 6.1). At the macroscale, without the solid surface effect, the nature of an emulsion is mainly determined by the respective affinity of the surfactant molecules for the water and the oil phases. The affinity of a surfactant molecule to water and oil can be empirically evaluated by the balance of the size and strength of the hydrophilic and hydrophobic parts in a surfactant molecule which is called Hydrophilic-Lipophilic-Balance (HLB) value [7, 8]. In macroscale emulsion fabrication, this affinity scale is a way of predicting the emulsion type from the surfactant molecular

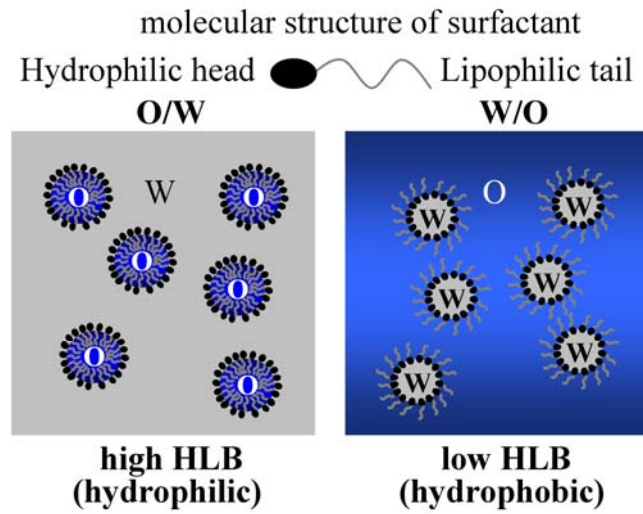


Figure 6.1 Surfactant structure and emulsion types in macroscale emulsion preparation corresponding to HLB values. O and W indicate oil and water phases, respectively.

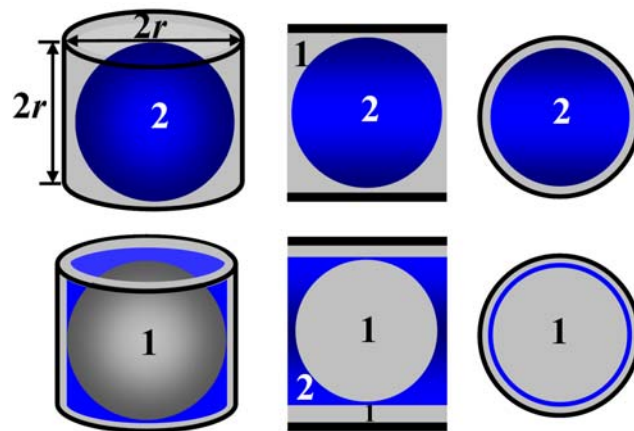


Figure 6.2 Schematic of L_2 -in- L_1 (upper) and L_1 -in- L_2 (lower) emulsions formed in a L_1 -philic cylindrical microchannel (cylinder diameter $2r$, length $2r$). 1 and 2 represent L_1 and L_2 . The left, middle and right pictures are a 3D, side-view and top-view sketch, respectively.

composition. Surfactants with high HLB values (more hydrophilic) preferentially encapsulate oil as droplets in water, and vice versa, surfactants with low HLB values (more hydrophobic) give W/O emulsions easily (Fig. 6.1). A requisite HLB value for different purposes can be obtained by blending two surfactants [9-11]. Selection of surfactants is therefore crucial in creation of emulsions at the macroscale.

When the size of the emulsion container decreases down to the micrometric scale ($<$ capillary length), it will become equal to the typical size of the emulsion droplets. Furthermore the effect of gravity and inertial forces on microfluidics can be neglected due to the small Weber and Bond numbers [4], and the surface-to-volume ratio increases dramatically. As a result the solid-liquid interfacial tension plays a dominant role for emulsions created in a microsystem [12-14]. Fig. 6.2 illustrates how the formation of an emulsion where the non-wetting phase is the continuous phase (lower) involves the creation of one extra interface when compared to an emulsion where the wetting phase is the continuous phase (upper). The extra surface necessitates the introduction of extra surface energy, so that the resulting emulsion is thermodynamically unstable. This argument can also be made in a more formal way. It is well-known that, when two immiscible liquids L_1 and L_2 (oil and water, for instance) contact a solid surface (S), one preferentially wets the surface. The contact line shapes itself due to the differences among interfacial tensions [12, 13]. If we confine circular droplets (diameter $2r$) of L_1 and L_2 together in an L_1 -philic cylindrical microchannel of equal diameter and of length $2r$ (Fig. 6.2), the minimum amount of energy required to form an L_2 -in- L_1 emulsion is

$$\Delta E_{L_2/L_1} = 4\pi r^2 \sigma_{SL_1} + 4\pi r^2 \sigma_{L_1L_2} \quad (6.1)$$

However, formation of L_1 -in- L_2 emulsion requires

$$\Delta E_{L_1/L_2} = 4\pi r^2 \sigma_{SL_1} + 4\pi r^2 \sigma_{L_1L_2} + 4\pi r^2 \sigma_{L_2L_1} \quad (6.2)$$

In the latter case, since the channel is preferentially wetted by L_1 , there must exist a thin layer of L_1 on the surface and an extra interface is introduced [15]. Since

$\Delta E_{L_2/L_1} < \Delta E_{L_1/L_2}$, an L_2 -in- L_1 emulsion is energetically preferred in an L_1 wetting microchannel, and vice versa. In general, if $r_{\text{droplet}} \approx r_{\text{container}}$, the creation of the wetting phase as the continuous phase is always favorable in a channel of any diameter when gravity and inertial forces can be neglected. However, the energy difference between L_1 -in- L_2 and L_2 -in- L_1 emulsifications, $(\Delta E_{L_1/L_2} - \Delta E_{L_2/L_1})$, can be small if σ_{L_1/L_2} is low.

The manipulation of surface wettability is therefore critical for droplet manipulation in microfluidic devices [16-19]. The materials which are commonly used to make microfluidic devices are oxide-covered silica and glass which are natively hydrophilic, or PDMS which is normally hydrophobic [20-24]. Simulations [25-31] have demonstrated that surface wettability of fluids is crucial to describe the flow of two immiscible fluids flow in microfluidic devices. However, only a few works [17, 18] have been reporting on the effect of surfactants on oil-water two-phase microfluidics.

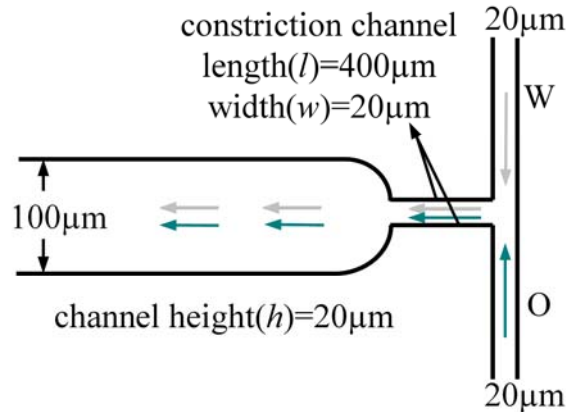


Figure 6.3 Schematic of the microfluidic device.

In this chapter, we investigate the influence of both solid-liquid and liquid-liquid interfacial tensions on water-oil two-phase flow in microfluidic devices. Head-on microfluidic devices (Fig. 6.3) are designed and used to ensure the same entry conditions for the water and oil phases. Solid-liquid interfacial tension is modified by either using natively hydrophilic microchannels or the same microchannels chemically hydrophobized by silane molecules. Fluid-fluid interfacial tension is controlled by using different surfactants (SDS, Tween80 and Span80), looking at the influence of the wettability in the range of HLB values of 4~40 and the interfacial tension in the range of 10^{-2} ~ 10^{-4} N.m⁻¹. The combination or competition of solid-liquid and liquid-liquid interfacial properties in the microchannel will be seen to engender complex flow behaviors. A precise theoretical study of these is postponed for subsequent studies. By applying the same flow conditions using our devices, we can investigate how interfacial tensions influence on oil-water two-phase flow behaviors at the micrometric scale.

6.2 Experimental

6.2.1 Chip fabrication

The design of the microfluidic device is shown in Fig. 6.3. Microchannels were fabricated (reactive ion etched) in a silicon (100) wafer using the standard photolithography process. Interconnection holes were opened from the backside of the wafer using powder-blasting techniques. The silicon wafer was then bonded to an empty Pyrex (transparent borosilicate glass) wafer using anodic bonding techniques. The resulting bonded wafers were then diced into 10 mm × 20 mm chips. Chips were fixed in a home-made chip holder and connected to syringes *via* capillary tubing (OD 1/16 inch, ID 50 μm) and Nanoport connectors including a filter (INACOM INSTRUMENTS BV, Upchurch Scientific, Holland). Flow was controlled using a dual syringe pump (Harvard PHD 22/2000, HUGO SACHS ELECTRONIK-HAVARD APPARATUS GmbH) to ensure constant flow ratios for the two phases

introduced into the two inlets. The water and oil phases met at the entrance of the constriction channel, and then flowed through constriction and wide outlet channel (Fig. 6.3). The flow was visualized using an inverted microscope (Leica DMIRM) and recorded by a CCD camera (Orca ER).

In order to avoid the dependence of phase volume ratio and shear conditions [10, 32], we performed all experiments under the same volume ratio (1:1), flow rate (shear) and flow rate ratios in the microfluidic devices. The flow rates of water (Q_w) and oil (Q_o) phases were both $0.10 \mu\text{L}\cdot\text{min}^{-1}$ ($Re \approx 0.1$). In order to preserve the channel wettability, note that the hydrophilic and hydrophobic microfluidic devices were stored in water and hexadecane in glassware and a plastic container, respectively, before using.

6.2.2 Surface modification of microchannels

Our microfluidic devices were made of hydrophilic native oxide covered silica and Pyrex (borosilicate glass). The same microfluidic devices from the same wafer were also modified to become hydrophobic using a silanization treatment with a solution of isooctane containing 2 v/v% 1H, 1H, 2H, 2H - perfluorodecyltrichlorosilane (FDTS, $\text{C}_{10}\text{H}_4\text{Cl}_3\text{F}_{17}\text{Si}$, 97%, ABCR GmbH & Co. KG, Karlsruhe, Germany). The coating process is sketched in Fig. 6.4.

The organosilane molecules adsorb onto the surface and a Si-Cl group of each organosilane reacts with a surface OH group to form Si-O-Si bonds. The remaining Si-Cl bonds on each molecule react with neighboring organosilane molecules in the presence of trace pre-adsorbed water molecules to form a network of Si-O-Si bonds over the surface. The presence of the resulting long fluorinated hydrocarbon chain on the treated surface consequently causes water repulsion from the surface, which therefore exhibits a preferential affinity for organic solvents. A water droplet exhibits a contact angle of 110°C on the FDTS covered surface. The FDTS treated surface is strong and stable, withstanding long time, high temperature and different chemical treatments [19].

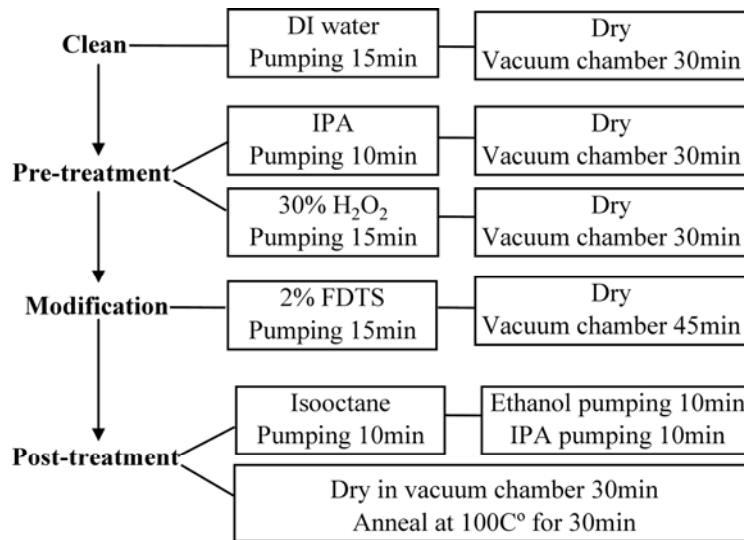


Figure 6.4 Schematic process of microchannel hydrophobic surface modification.

6.2.3 Preparation of fluids

The water phase was made fluorescent by dissolving fluorescein sodium salt (Sigma-Aldrich Chemie GmbH, Germany) in DI water at a final concentration of 0.01M. The organic phase consists of hexadecane without any added fluorescent markers. Two-phase flows were visualized in fluorescent mode.

Solutions were prepared by solving hydrophilic surfactants in water and hydrophobic surfactant in hexadecane. Surfactant concentrations were all above the critical micelle concentration (cmc). Hydrophilic surfactants used were sodium dodecyl sulfate (SDS 99+%, CH₃(CH₂)₁₁OSO₃Na, HLB = 40, cmc = 0.2 wt%, Sigma-Aldrich Chemie GmbH, Germany) and Tween80 (HLB = 15, cmc = 0.1 wt%, Sigma-Aldrich Chemie GmbH, Germany), while the hydrophobic surfactant was Span80 (HLB = 4.3, cmc = 0.02 wt%, Sigma-Aldrich Chemie GmbH, Germany). Solutions were degassed under vacuum. The components of solutions and water-hexadecane interfacial tensions

are listed in Table 6.1 [18, 33-42]. The resulting water-hexadecane interfacial tensions are $\sim 10^{-2}$ N.m⁻¹ except for (SDS + Span80) which is $< 10^{-4}$ N.m⁻¹.

6.3 Results and Discussion

6.3.1 Emulsion types at the macroscale

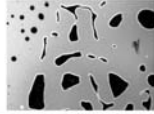
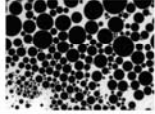
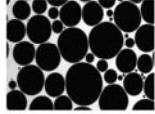
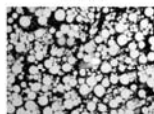
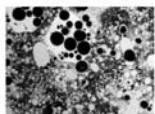
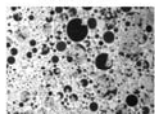
The macroscale emulsion types were determined by mixing different solutions (Table 6.1) at the volume ratio of 1:1. Every mixture was sonicated for 5 min in a glass cuvette. A drop of mixture was then deposited onto a glass slide and imaged. Emulsion types can be easily determined since the fluorescein dye in the water phase shows bright white in the images while the oil phase is in black.

The emulsion types are listed in Table 6.2. It is seen that the type of emulsion obtained in the macroscale device depends primarily on the surfactant used. The single hydrophilic surfactants Tween80 (HLB = 15) and SDS (HLB = 40) create O/W emulsions, while the single hydrophobic surfactant Span80 (HLB = 4.3) creates W/O emulsion. The HLB value of Tween80 and Span80 blended at 1:1 volume ratio is 9.65 which falls between hydrophilic and hydrophobic regions [7, 11], therefore both W/O and O/W emulsions are obtained in the same system. The (water + SDS)/(hexadecane + Span80) interfacial tension is less than 10^{-4} N.m⁻¹, multi-emulsion (W/O/W or O/W/O) can be created [43-46]. Double emulsions, mainly W/O/W, are obtained by using SDS and Span80 together in our experiments.

Table 6.1 Interfacial tensions ($\sigma_{ow}/N.m^{-1}$) of different solution compositions

W \ O	DI water+0.01M Fluorescein (W1)	W1+2 wt% Tween80 (W2)	W1+0.01M SDS (W3)
Hexadecane (O1)	5×10^{-2}	1×10^{-2}	1×10^{-2}
O1+2wt% Span80 (O2)	1×10^{-2}	1×10^{-2}	$<10^{-4}$

Table 6.2 Emulsion types at the macroscale

W \ O	W1	W2	W3
O1	unstable 	O/W 	O/W 
O2	W/O 	W/O&O/W 	W/O/W 

– 50 μ m

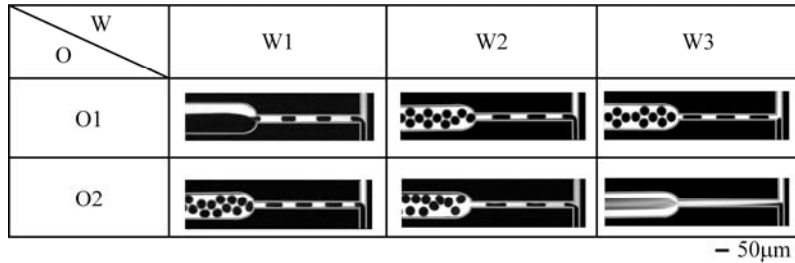
6.3.2 Emulsions in microchannels

6.3.2.1 Emulsion types – solid-liquid interfacial tension (surface wettability)

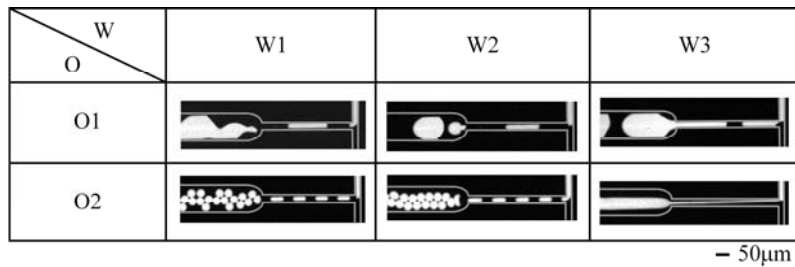
When water and oil phases meet at the entrance of the constriction channel without the use of surfactants, O/W flows are generated in native hydrophilic microchannels (Table 6.3a), while W/O flows are formed in the same channels modified by FDTS (Table 6.3b).

Table 6.3 Emulsions in microfluidic devices

(a) O/W emulsions created in hydrophilic microchannels, $Q_o = Q_w = 0.10 \mu\text{L}\cdot\text{min}^{-1}$



(b) W/O emulsions created in hydrophobic microchannels, $Q_o = Q_w = 0.10 \mu\text{L}\cdot\text{min}^{-1}$



* The gray lines in the pictures are used as a guide to the eye to indicate the channel walls.

In the same channel (hydrophobic or hydrophilic), under identical flow conditions, the emulsion types subsequently do not change from the ones obtained without surfactants when using different surfactants, indicating the predominance of σ_{SL} in determining emulsion type. Such behavior can indeed be explained from equations 1 and 2 as discussed above. In a silicon or glass microchannel the water phase is energetically inclined to flow along the hydrophilic channel walls as the continuous phase, creating an O/W flow; while a W/O flow can be obtained in a FDTS-coated hydrophobic microchannel. Increase of the concentration of Span80 and Tween80 concentration from 1 wt% to 10 wt% in hexadecane and water does not change the emulsion type. Although surfactants, such as Tween80, can temporarily coat the channel surface, the coating layer will be removed when the water flows through

the microchannel at $0.1 \mu\text{L}\cdot\text{min}^{-1}$. Surfactants therefore do not remain to modify the channel surfaces and the original surface properties determine the solid-liquid interfacial tension. Although surfactants with different HLB values were used in water or hexadecane, the emulsion types did not change. Both stable droplet deformation (Tables 6.3a and 3b: W2 + O2) was observed as well as coalescence (Table 6.3b: W2 + O1 and W3 + O1) when the HLB value and the contact angle tended to create opposite interfacial curvatures.

Emulsion types in these microfluidic devices thus depend only on the original microchannel surface wettability, independent of what surfactant is used. We can therefore easily control emulsion types (O/W or W/O) in microfluidic devices by simple surface modification methods. This behavior is different from the normal macroscale emulsification techniques which are strongly surfactant-dependent (liquid-liquid interface).

6.3.2.2 Flow patterns – liquid-liquid interfacial tension (surfactants)

When inspecting the experimental results listed in Table 6.3, it is seen that, in these microfluidic devices, at the flow rate and flow rate ratios used, droplet-based flows are obtained for all surfactants except for the combination of SDS and Span80 where stratified flows are generated. This can be explained in the following way.

At the microscale, two forces – interfacial force and viscous force – dominate with respect to inertial and gravity forces. The capillary number is the ratio of these two competitive forces, and can be expressed as:

$$Ca = \frac{\eta v}{\sigma} \quad (6.3)$$

where η (Pa.s) and v ($\text{m}\cdot\text{s}^{-1}$) are the continuous phase viscosity and flow velocity, and σ ($\text{N}\cdot\text{m}^{-1}$) is the oil-liquid interfacial tension. Addition of surfactants decreases the interfacial tension. Water-hexadecane interfacial tensions are about $10^{-2} \text{ N}\cdot\text{m}^{-1}$ when using Tween80, SDS, Span80 or (Tween80 + Span80), and Ca falls in the range of $10^{-3}\sim 10^{-2}$ ($\eta = 10^{-3} \text{ Pa}\cdot\text{s}$, $Q = 0.1 \mu\text{L}\cdot\text{min}^{-1}$) for these surfactants. The viscous force is

much smaller than the interfacial force; therefore, droplet-based flows are generated in these systems. However, the interfacial tension of water-hexadecane is less than 10^{-4} N.m⁻¹ when using (SDS + Span80). Ca then is in the range of 0.1~1 under the same flow conditions. In this case, the viscous force dominates interfacial force, and a stratified flow pattern is obtained.

Furthermore, as shown in Table 6.3, the combination or competition between solid-liquid and liquid-liquid interfacial properties can create complex two-phase flow phenomena, such as deformation and coalescence, when the flow conditions slightly change. We only showed important phenomena but omitted some detailed fluidic dynamics which is out of our view in this manuscript. In microfluidic systems, the use of surface and surfactant combinations can be a useful tool for quantitatively manipulating and evaluating droplet generation, deformation and coalescence phenomena which are difficult to realize in the macroscale devices.

6.3.3 Emulsion inversion in microchannels

As discussed in previous sections, in microchannels the solid-liquid interfacial tension is the determinant factor for emulsion type. It has been shown that change of microchannel surface wettability can therefore induce coalescence. Here we will demonstrate that it can even cause emulsion inversion. We prepared a microchannel patterned with adjacent hydrophobic and hydrophilic patches. Fig. 6.5 shows a water-in-oil two phase emulsion moving through this channel from top to bottom. A water droplet in oil flow (top of the picture) arriving at the interface between both patches turns, after a brief rearrangement phase in which no clear emulsion type is visible, into an oil droplet in water flow (bottom of the picture).

For the first time, we could hereby realize an emulsion inversion in the same microchannel. The capability of inverting emulsions might be very useful in real life, for instance to obtain desired food products [3, 47]. Furthermore, this result proves our previous conclusion that it is the solid-liquid interfacial tension which determines the emulsion type in microfluidic devices.

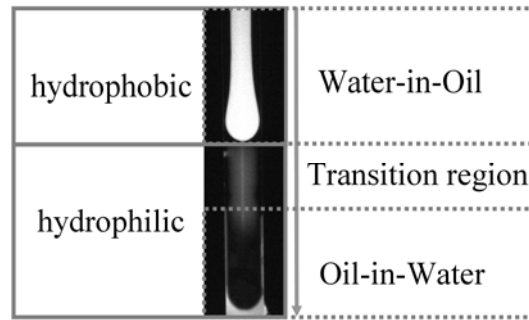


Figure 6.5 The emulsion inversion in a hydrophobic-hydrophilic microchannel: $h = 20 \mu\text{m}$ and $w = 100 \mu\text{m}$. The two-phase emulsion moves from top (hydrophobic walls) to bottom (hydrophilic walls). The emulsion type is seen to change from W/O (a white droplet in a black background) to O/W (a black droplet in a white background) after a brief transition region between. The two phases were oil (hexadecane, shown in black) and water (aqueous solution with 0.01M fluorescein and 0.3 wt% SDS, shown in white).

6.4 Conclusions and Outlook

The surface-to-volume ratio increases on downscaling. The predominance of interfacial tension in microfluidic systems can be harnessed to tailor the two-phase flow behavior within the system. We experimentally investigated the influence of solid-liquid and liquid-liquid interfacial tensions on oil-water two-phase flow behavior in microchannels. The emulsion types, at the macroscale, predominantly determined by surfactant wettability – HLB value. However, at the microscale, the channel wall wettability (the solid/oil with respect to the solid/water interfacial tension) mainly determines the emulsion types generated in microchannels under the same flow conditions. Emulsion inversion could be realized by reversing microchannel surface wettability. The surfactants play a secondary role, determining the flow type. Both droplet-based flows and stratified flows have been obtained under the same flow condition by varying liquid-liquid interfacial forces in the range of $10^{-2} \sim 10^{-4} \text{ N}\cdot\text{m}^{-1}$.

Microdroplet deformation and coalescence have also been observed by combining solid-liquid and liquid-liquid interfacial properties.

Microfluidic technology can thus be useful to manipulate generation, deformation and coalescence of microdroplets. Furthermore, by observation and analysis of these flow behaviors under precisely controlled flow conditions using a microfluidic device, we might be able to estimate interfacial properties. The phenomenon of surface-wettability-determined emulsion types may be useful to invert emulsion types, such as food emulsions, to change food product types. The channel surface properties will be even more important if the dimension decreases further. Surface-determined flow phenomena may then be able to explain fluid transfer in some biological processes, such as water permeation in leaves.

References

- [1] O. Ozer, *Eur. J. Pharm. Sci.* **2007**, 32, S11.
- [2] J. E. Vinatieri, *Soc. Petrol. Eng. J.* **1980**, 20, 402.
- [3] C. W. Hutton, A. M. Campbell, *J. Food Sci.* **1977**, 42, 457.
- [4] H. A. Stone, A. D. Stroock, A. Ajdari, *Annu. Rev. Fluid Mech.* **2004**, 36, 381.
- [5] A. S. Utada, E. Lorenceau, D. R. Link, et al., *Science* **2005**, 308, 537.
- [6] H. Song, D. L. Chen, R. F. Ismagilov, *Angew. Chem.-Int. Edit.* **2006**, 45, 7336.
- [7] W. C. Griffin, *J. Soc. Cosmetic Chem.* **1949**, 1, 311.
- [8] C. Y. Lin, L. W. Chen, *Fuel Processing Tech.* **2006**, 87, 309.
- [9] K. Shinoda, T. Yoneyama, H. Tsutsumi, *J. Disper. Sci. Technol.* **1980**, 1, 1
- [10] J. V. Kloet, L. L. Schramm, *J. Surfactants & Detergents* **2002**, 5, 19.
- [11] J. Boyd, P. Sherman, Parkinso.C, *J. Colloid Interface Sci.* **1972**, 41, 359.
- [12] A. Quinn, R. Sedev, J. Ralston, *J. Phys. Chem. B* **2005**, 109, 6268.
- [13] T. Roques-Carnes, S. Palmier, R. A. Hayes, et al., *Colloid Surface A* **2005**, 267, 56.
- [14] D. T. Wasan, A. D. Nikolov, *Nature* **2003**, 423, 156.
- [15] *In this analysis we assumed that droplet and container radii were equal and the surface energy independent of emulsion type. When however the droplet radius is smaller than the channel diameter and the interfacial energy of L1-in-L2 emulsions is different from L2-in-L1 emulsions due to the introduction of surfactants with suitable HLB factors (see below), it can become energetically favorable for the continuous phase to be the non-wetting phase.*
- [16] B. Zhao, N. O. L. Viernes, J. S. Moore, et al., *J. Am. Chem. Soc.* **2002**, 124, 5284.
- [17] M. J. Geerken, R. G. H. Lammertink, M. Wessling, *Colloid Surface A* **2007**, 292, 224.
- [18] R. Dreyfus, P. Tabeling, H. Willaime, *Phys. Rev. Lett.* **2003**, 90, 1445051.
- [19] K. Handique, D. T. Burke, C. H. Mastrangelo, et al., *Anal. Chem.* **2000**, 72, 4100.
- [20] Y. C. Tan, V. Cristini, A. P. Lee, *Sens. Actuator B, Chem.* **2006**, 114, 350.

-
- [21] J. H. Xu, S. W. Li, J. Tan, et al., *Aiche J.* **2006**, *52*, 3005.
- [22] P. Garstecki, M. J. Fuerstman, H. A. Stone, et al., *Lab Chip* **2006**, *6*, 437.
- [23] H. Maenaka, M. Yamada, M. Yasuda, et al., *Langmuir* **2008**, *24*, 4405.
- [24] S. Li, J. Xu, Y. Wang, et al., *Langmuir* **2008**, *24*, 4194.
- [25] O. Kuksenok, D. Jasnow, A. C. Balazs, *Phys. Rev. Lett.* **2005**, *95*, 2406031.
- [26] O. Kuksenok, D. Jasnow, J. Yeomans, et al., *Phys. Rev. Lett.* **2003**, *91*, 1083031.
- [27] O. Kuksenok, D. Jasnow, A. C. Balazs, *Phys. Rev. E* **2003**, *68*, 0515051.
- [28] R. Verberg, C. M. Pooley, J. M. Yeomans, et al., *Phys. Rev. Lett.* **2004**, *93*, 1845011.
- [29] O. Kuksenok, A. C. Balazs, *Physica D* **2004**, *198*, 319.
- [30] O. Kuksenok, J. M. Yeomans, A. C. Balazs, *Phys. Rev. E.* **2002**, *65*, 0315021.
- [31] O. Kuksenok, A. C. Balazs, *Phys. Rev. E* **2003**, *68*, 0115021.
- [32] C. H. Villa, L. B. Lawson, Y. M. Li, et al., *Langmuir* **2003**, *19*, 244.
- [33] V. Schroder, H. Schubert, *J. Colloid Interface Sci.* **1999**, *152*, 103.
- [34] G. Bai, M. L. Brusseau, R. M. Miller, *J. Contam. Hydrol.* **1997**, *25*, 157.
- [35] J. H. Xu, S. W. Li, W. J. Lan, et al., *Langmuir* **2008**, *24*, 11287.
- [36] G. T. Vladislavjevic, I. Kobayashi, M. Nakajima, et al., *J. Membrane Sci.* **2007**, *302*, 243.
- [37] I. Kobayashi, M. Nakajima, S. Mukataka, *Colloid Surface A* **2003**, *229*, 33.
- [38] P. Somasundaran, H. K. Lee, E. D. Shchukin, et al., *Colloid Surf. A-Physicochem. Eng. Asp.* **2005**, *266*, 32.
- [39] N. K. Dimov, V. L. Kolev, P. A. Kralchevsky, et al., *J. Colloid Interface Sci.* **2002**, *256*, 23.
- [40] S. C. Oh, D. O. Shah, *J. Phys. Chem.* **1993**, *97*, 284.
- [41] L. Lobo, A. Svereika, *J. Colloid Interface Sci.* **2003**, *261*, 498.
- [42] K. Giribabu, P. Ghosh, *Chem. Eng. Sci.* **2007**, *62*, 3057.
- [43] P. Stroeve, P. P. Varanasi, *J. Colloid Interface Sci.* **1984**, *99*, 360.
- [44] E. J. Clayfield, A. G. Dixon, A. W. Foulds, et al., *J. Colloid Interf. Sci.* **1985**, *104*, 500.
- [45] M. Kanouni, H. L. Rosano, N. Naouli, *Adv. Colloid Interfac.* **2002**, *99*, 229.
- [46] L. Wen, K. D. Papadopoulos, *J. Colloid Interface Sci.* **2001**, *235*, 398.
- [47] O. Skurtys, J. M. Aguilera, *Food Biophys.* **2008**, *3*, 1.

Chapter 7

Two-Phase Flow in Nanochannels

We developed a novel method to control liquid flow in a nanochannel using an integrated regulating microchannel connected to the nanochannel. Stable flows with flow rates as low as a $\text{pL}\cdot\text{s}^{-1}$ can be obtained. Mixing of two miscible liquids in nanochannels is used to validate the flow control method. Using this method, we also demonstrate two-phase flow (dripping and threading) in nanochannels by confluence of two immiscible liquids.

7.1 Introduction

Precise understanding of biological or chemical functions requires tools comparable in size to the basic components. With their specific characteristics, smaller droplets in two-phase flow are highly required. Small containers can provide a means of confining single molecules inside of a femtoliter measurement volume. To study single molecules in a solution with a nM activity, one needs femtoliter size containers. Although measurements can be made on single molecules in a dilute solution as they diffuse through the measurement volume, most such approaches rely on sophisticated optical strategies to limit the detection volume. Single molecule studies have revealed molecular behavior usually hidden in the ensemble and time-averaging of bulk experiments. Using this method however, it is difficult to follow the dynamics of a single molecule for longer than the transit time through the measurement volume, usually on the order of a few ms. An attractive approach is therefore to perform the assay inside very small containers. To study dynamics on longer time scales, methods have been developed to immobilize and isolate or confine the molecule or molecular complexes under study while still permitting physiological interactions and optical observations to occur. Researchers seek to work with smaller volumes since both physical movement and diffusional mixing of chemicals in very small volumes become very rapid. The container should however be closed or sufficiently isolated from the environment that the substances held in the container do not escape into the surrounding medium, by evaporation or diffusion. The contents of individual containers should if possible be independently controllable so that distinct reactions can take place in separate containers. Open container nanovials in solid substrates have been scaled down to the femtoliter size [1]. However, these containers were not closed, with the consequences that water evaporates quickly. Furthermore the contents of the container is difficult to access and not reusable, so that it can not be independently controlled. An emulsion in which one liquid forms droplets in another immiscible liquid (water-droplet-in-oil or oil-droplet-in-water) is a simple and attractive way of

creating very small closed containers and does not have the disadvantages of the open nanovials [2, 3]. Studies have demonstrated single molecule enzymatic dynamics [2] and single molecule PCR [3] within droplets.

Smaller droplets allow the use of higher concentrations of the molecules under study, which greatly simplifies operational procedures. Creation and control of small and monodisperse droplets is therefore needed. A microfluidic device is ideal for the manipulation of small volumes of fluids. It therefore is our platform of choice for tailoring fluids to create size-controlled monodisperse droplets. The formation of a liquid filament thereby is in most cases a mandatory preliminary step for producing a droplet. Smaller droplets can be formed using flow focusing by increasing shear gradients [4]. The flow focusing confinement is however highly dependent on fluid properties and flow rates, which is not convenient. We therefore prefer to use an identical setup as demonstrated in previous chapters, namely the head-on flow geometry. As we also have seen from previous chapters, the droplet size will now be determined by the confining channel size. To obtain smaller droplets, it is therefore necessary to downscale this device to the nanometer scale.

Nanochannels can currently be easily fabricated by the standard photolithography process. However, the specific interfacial area of a nanochannel is very high, so that interfacial phenomena become dominant. Size-confinement effects in nanochannels are therefore distinct, as for instance a high hydrodynamic flow resistance, overlap of electric double layers (EDL) [5-10]. The flow control in nanochannels is therefore difficult because of their high pressure loss and very small volume flow rate. When two-phase flow is created in nanochannels, an additional experimental difficulty is introduced, since capillary pressures are very high in the nanochannel confinement. Moreover, the non-conductive phase, gas or oil, makes other pumping methods as for example EOF (electro-osmotic-flow), unavailable. Pressure-driven flow is therefore preferred for an oil-water two-phase nanofluidic system, even though it is experimentally difficult due to the high backpressure and the low flow rates needed.

In conventional pressure-driven flow, the standard method is to apply pressure

from a syringe pump directly to a nanochannel. A volume flow rate of less than one $\mu\text{L}\cdot\text{min}^{-1}$ however is difficult to obtain, and it takes a very long time to replace the liquid due to the dead volume of e.g. the connecting capillaries. Nanofluidic flow using external pressure control method has been demonstrated by Kitamori et al [11-13]. In this chapter, we solved these complications and designed an integrated internal flow control system using a microchannel connected to a nanochannel to regulate the flow rate in the nanochannel. The design is shown in Fig. 7.1. Liquids are introduced to the nanochannels (blue) from the sides, by microchannels (green) which are connected between an inlet and a flow regulating channel. Since most of the liquid that is pumped by the syringes flows through the regulating microchannels, nanochannel volume flow rates lower to $\text{pL}\cdot\text{min}^{-1}$ can be obtained and the flow (or pressure) in nanochannel remains stable. In order to verify this flow control method, the mixing of two miscible liquids in the nanochannels was investigated. In addition, the behaviour of an oil-water immiscible two-phase system was studied in the nanochannels, showing dripping and threading.

7.2 Experimental

7.2.1 Device design

The schematic chip design is shown in Fig. 7.1. For the experiments described in this work, except for the regulating microchannels the nanofluidic channel section consists of two identical inlets and a constriction channel. Two identical microchannel sections run from the syringe inlet to an outlet via a flow regulating channel, and also connect to both of the nanochannel inlets. The inlets and constriction nanochannel dimensions are of height (h) = 150 ~ 900 nm, width (w) = 10 μm and length (l) = 500 μm ; and the microchannel dimensions are of height (H) = 10 μm , width (W) = 50 or 100 μm , length (L) = 5 mm.

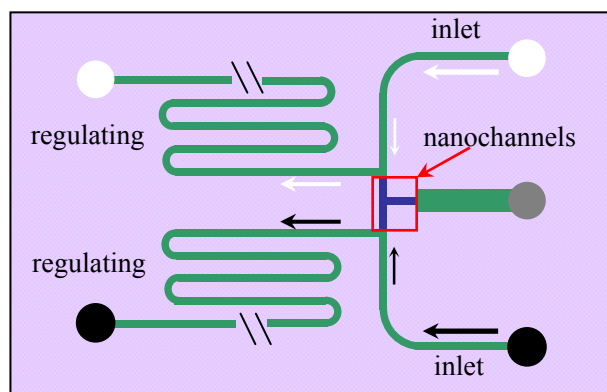


Figure 7.1 Sketch of the nano-micro fluidic chip design.

7.2.2 Fabrication and setup

The devices were fabricated using standard photolithographic techniques. Nanochannels and microchannels were etched into a borosilicate glass wafer. The connection holes were drilled in a second borosilicate glass wafer using powder blasting techniques. Subsequently, these two wafers were aligned and thermally bonded together. We diced the bonded wafers to 10 mm × 20 mm sized chips, which were mounted in a home-made chip holder and connected to gas-tight syringes (Microliter Syringes, Hamilton) *via* nanoport connectors (Upchurch Scientific). Harvard syringe pumps (PHD 22/2000, Harvard Apparatus) were used to drive the liquid flow. The two-phase flow was visualized by an inverted microscope (Leica DMIRM) and recorded using a CCD camera (Orca ER).

7.2.3 Fluids

The water phase was made fluorescent (appearing white in the microphotographs) by dissolving fluorescein sodium salt (Sigma-Aldrich Chemie GmbH, Germany) in de-ionized water at a final concentration of 0.01 mol.L⁻¹ ($\eta_w = 1$ mPa.s). The organic

phase (dark in the images) consisted of hexadecane (Sigma-Aldrich Chemie GmbH, Germany) without any added fluorescent markers ($\eta_0 = 3 \text{ mPa}\cdot\text{s}$). Surfactants were used to stabilize generated droplets. The surfactants used were sodium dodecyl sulfate ($\text{CH}_3(\text{CH}_2)_{11}\text{OSO}_3\text{Na}$, SDS 99+%, Sigma-Aldrich Chemie GmbH, Germany), Tween80 (Sigma-Aldrich Chemie GmbH, Germany), and Span80 (Sigma-Aldrich Chemie GmbH, Germany). Solutions were prepared by dissolving hydrophilic surfactants (0.3 wt% SDS and 1 wt% Tween80) in water or hydrophobic surfactant (1 wt% Span80) in hexadecane. The surfactant concentrations were in all cases above the critical micelle concentrations. The interfacial tensions of hexadecane / (0.3 wt% SDS aqueous solution), hexadecane / (1 wt% Tween80 aqueous solution), (1 wt% Span80 hexadecane solution) / water are all about $10 \text{ mN}\cdot\text{m}^{-1}$, and the interfacial tension of (0.3 wt% SDS aqueous solution / 1 wt% Span80 hexadecane solution) was about $0.1 \text{ mN}\cdot\text{m}^{-1}$. Solutions were degassed under vacuum for 1 hour.

7.3 Results and Discussion

7.3.1 Flow control in nanochannels

Using the Hagen-Poiseuille equation, the pressure drop in a channel can be expressed as:

$$\Delta P = C \frac{\eta L Q}{wh^3} \quad (7.1)$$

where ΔP , η , L , Q , w and h correspond to pressure drop (Pa), viscosity (Pa.s), length (m), flow rate ($\text{m}^3\cdot\text{s}^{-1}$), channel width (m) and height (m), and C is a dimensionless constant which is the same for the nanochannel and microchannel since $w \gg h$ and $W \gg H$. The liquid is introduced from an inlet microchannel and at a junction it splits into two flows, one into the nanochannel and the other into a regulating microchannel. Since the outlet pressure of both is the same, which is P_{atm} , the pressure drop over a regulating microchannel equals that over the nanochannels. Therefore, we obtain:

$$\frac{Q_n}{Q_m} = \frac{Lwh^3}{lWH^3} \quad (7.2)$$

The subscript m and n indicate microchannel and nanochannel, respectively. When the channel dimensions are constant, Q_n is determined by Q_m which is approximately the same as the applied flow rate of the syringe pump since $h \ll H$ and $Q \ll Q$. Therefore, we can calculate Q_n by simply using applied flow rates. For instance, we can obtain that $Q_n = 2.1 \times 10^{-4} \mu\text{L} \cdot \text{min}^{-1}$ (or flow velocity $v = 0.8 \text{ mm} \cdot \text{s}^{-1}$) when $Q_m = 1 \mu\text{L} \cdot \text{min}^{-1}$, $L = 5 \text{ mm}$, $l = 1 \text{ mm}$ (including the length of the arm), $w = 10 \mu\text{m}$, $W = 30 \mu\text{m}$, $h = 0.5 \mu\text{m}$, and $H = 10 \mu\text{m}$. Flow rates in the nanochannel (Q_n) of $10^{-5} \sim 10^{-3} \mu\text{L} \cdot \text{min}^{-1}$ can therefore be obtained by varying Q_m from 0.1 to $10 \mu\text{L} \cdot \text{min}^{-1}$, rates conveniently within the range of the syringe pump employed.

At the nanoscale, interfacial tension plays a highly important role due to the extremely high surface-to-volume ratio. The capillary pressure inside a channel is given by:

$$P_{\text{cap}} = \frac{\sigma}{r} \quad (7.3)$$

where σ is the water-oil interfacial tension, and r is the radius of the interfacial curvature. Since the channels are hydrophilic, the capillary pressure plays different roles for the water and oil phases. Water is hydrophilic and spontaneously fills into the nanochannels due to the capillarity. However, the oil phase does not enter the channel until the applied pressure in the oil phase $P_o > \Delta P_{\text{cap}}$. The minimum applied oil flow rate at which the oil starts to enter the nanochannels for Q_w (the water flow rate in nanochannel) is zero, Q_{min} (the nanochannels are filled with water) can then be calculated as (simply taking $r = h/2$ by assuming completely wetting of nanochannels):

$$Q_{\text{min}} = \frac{2\sigma WH^3}{C\eta Lh} \quad (7.4)$$

It can be seen that Q_{min} is dependent on the regulating microchannel geometry (W , H and L), and inversely proportional to the nanochannel height h ($h \ll w$). For instance,

oil can not enter the nanochannel until $Q_o \approx Q_{\min} = 0.12 \mu\text{L}\cdot\text{min}^{-1}$ for a device with $h = 500 \text{ nm}$, and $H = 10 \mu\text{m}$, $W = 100 \mu\text{m}$, $L = 5 \text{ mm}$, assuming $C = 32$.

In order to check the flow control method, we designed and fabricated devices with different heights of the nanochannel section, as seen in Fig. 7.1. Experiments indeed showed that, for different devices, the oil did not enter the nanochannel until the oil flow rate surpassed a critical value. Fig. 7.2 shows the plot of Q_{\min} as a function of nanochannel height (h). The experimental and calculated data fit quite well. Due to the coexistence of oil and water in the same channel, not only the geometry but also the flow of water and oil will influence each other, amongst others by shearing. We also observed that Q_{\min} increased with the water flow rate.

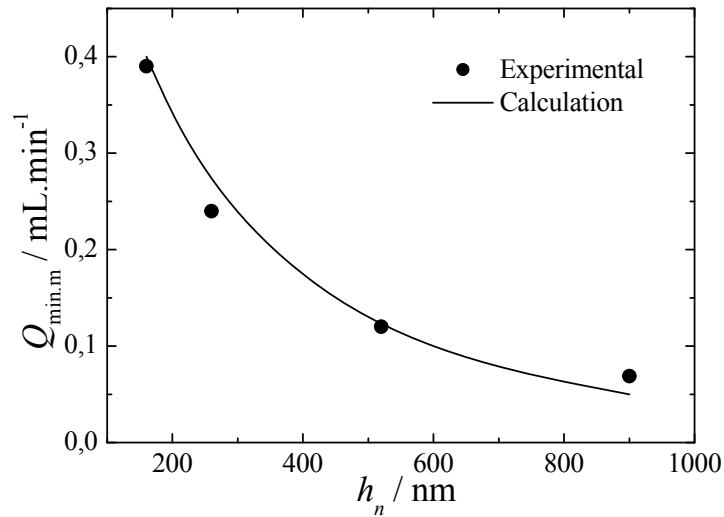


Figure 7.2 Plot of minimum applicable oil flow rate vs nanochannel depth (h). Here, $H = 10 \mu\text{m}$, $W = 100 \mu\text{m}$, $L = 5 \text{ mm}$, $\sigma = 30 \text{ mN}\cdot\text{m}^{-1}$ and $\eta_o = 3 \text{ mPa}\cdot\text{s}$.

7.3.2 Miscible two phases mixing in nanochannels

In order to validate the flow control method, we investigated the mixing of two aqueous solutions in the nanochannel. Fig. 7.3 shows fluorescent microscopy photographs of two aqueous solutions flowing in the nanochannels at different flow rates. The nanochannels are 500 nm deep and 10 μm wide. The two solutions are 0.01 M fluorescein aqueous solution (from top channel) and DI water (from bottom channel). The applied DI water flow rate was fixed at $0.1 \mu\text{L}\cdot\text{min}^{-1}$ so that the flow rate in the nanochannel was calculated to be $2.1 \times 10^{-5} \mu\text{L}\cdot\text{min}^{-1}$. The flow rate of the fluorescein solution in the microchannel was increased from $0.1 \mu\text{L}\cdot\text{min}^{-1}$ (Fig. 7.3a) to $0.15 \mu\text{L}\cdot\text{min}^{-1}$ (Fig. 7.3b), and $0.2 \mu\text{L}\cdot\text{min}^{-1}$ (Fig. 7.3c). The expected flow rates of the fluorescein solution in the nanochannel are 2.1×10^{-5} , 3.1×10^{-5} and $4.2 \times 10^{-5} \mu\text{L}\cdot\text{min}^{-1}$, respectively.

By analyzing fluorescent images, the fluorescent intensity of one channel (DI water) is obviously lower than that of another channel (fluorescein solution), see Fig. 7.3. Two liquids start to mix when they contact at the junction, and then flow together through the horizontal nanochannel to the outlet. Comparing the intensity profile across the nanochannel at the junction (position 1) and 200 μm downstream (position 2), we clearly obtain that the two liquids are fully mixed when downstream. The measured average intensity of mixtures of a, b and c, with the theoretical values between brackets, are 0.48 (0.5), 0.63 (0.6) and 0.71 (0.67), respectively. The intensity therefore increases with the flow rate ratio of fluorescein solution to DI water according to the expected values. These observations clearly indicate that two solutions were pumped into the nanochannels and mixed in the nanochannel in the expected proportions, and that the flow rate control method is valid.

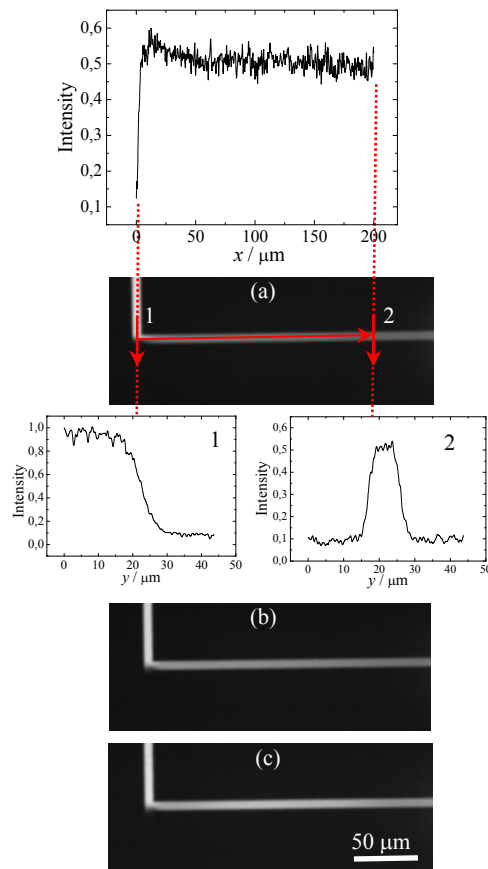


Figure 7.3 Mixing of 0.01M fluorescein aqueous solution and DI water in nanochannels ($h = 500 \text{ nm}$). (a) DI water and fluorescein aqueous solution flow rates are both $2.1 \times 10^{-5} \mu\text{L} \cdot \text{min}^{-1}$, (b) DI water flow rate and fluorescein solution flow rates are 2.1×10^{-5} and $3.1 \times 10^{-5} \mu\text{L} \cdot \text{min}^{-1}$, and (c) DI water flow rate and fluorescein solution flow rates are 2.1×10^{-5} and $4.2 \times 10^{-5} \mu\text{L} \cdot \text{min}^{-1}$. The intensity profiles along and across the horizontal channel (a) at the junction (1) and $200 \mu\text{m}$ downstream (2) are presented. The red arrows indicate the location and direction of the intensity profiles taken. All fluorescent intensities are normalized by the intensity in the top nanochannel.

7.3.3 Immiscible two phases flow in nanochannels

Oil (inner) and water (outer) phases were introduced from the two inlets into the nanochannel. Our design enables us to obtain flow rates in the nanochannels which are as low as $10^{-5} \mu\text{L}\cdot\text{min}^{-1}$. The water phase spontaneously filled into the channel as long as the device was connected to the syringe with water. However, there was no oil entering the nanochannel when $P_o < P_{\text{cap}}$. When the oil flow rate was increased above the threshold value Q_{min} , both oil and water flowed into the nanochannels. Oil and water met at the junction and flowed together in the constriction nanochannel. An oil-in-water flow pattern, where the water flowed along the channel walls and the oil in the middle were obtained due to the hydrophilicity of the channel walls. Either droplet-based or stratified (parallel) flow was obtained. A flow map showing the flow modes obtained based on the two flow rates of water and oil is displayed in Fig. 7.4.

The three typical flow regimes are named: non-oil, dripping and threading. In this device, non-oil flow means a regime that there is no oil in the constriction channel. Dripping corresponds to a flow regime where the emerging inner liquid (oil) breaks to form droplets in the constriction channel. Threading is distinguished from dripping, since here the oil and water liquid threads display continuous morphology along the constriction nanochannel, as illustrated in the inset of the flow diagram. Compared to the flow map in microchannels (Fig 4.3), we can observe that the dripping regime is smaller and threading regime is larger. This can be explained mainly by the very high aspect ratio (channel width/channel depth) of the nanochannel (62.5~11), as discussed in Chapter 6 (geometry factor).

The droplet size decreases as the water flow rate increases and the oil flow rate decreases in the same nanofluidic device (Fig. 7.5a). The droplet formation can also be divided into four stages, which is similar to the behavior observed in a microfluidic device. A high shear stress from the water phase could deform the droplets in the nanochannel, see Fig. 7.5b, at high water flow rates. Depending on flow rates of oil and water, the threading also displays different shapes in the nanochannel. The oil thread width increases as oil flow rate increases and water flow rate decreases (Fig. 7.5c).

Under the same flow conditions, the width also decreases with oil-water interfacial tension.

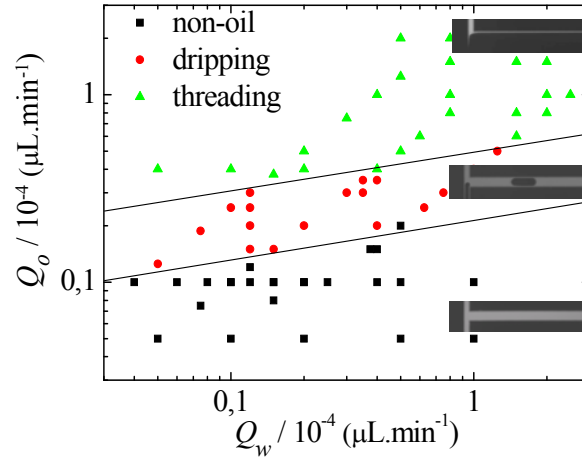


Figure 7.4 Flow diagram of water-oil two-phase flow in nanochannels ($h = 500$ nm). The micrographs were taken in fluorescent mode.

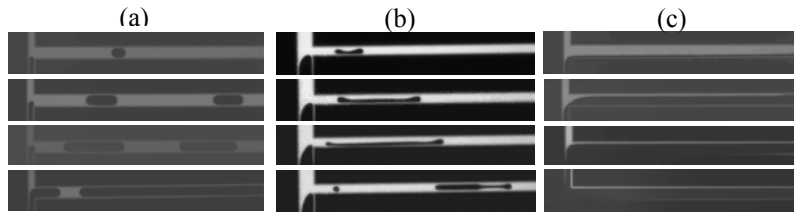


Figure 7.5 Droplet size and thread width change with relative flow rates. The flow rates are (a) from top to bottom: $Q_o = Q_w = 1 \times 10^{-5} \mu\text{L}\cdot\text{min}^{-1}$, $Q_o = 2.5Q_w = 2.5 \times 10^{-5} \mu\text{L}\cdot\text{min}^{-1}$, $Q_o = 2.5Q_w = 5 \times 10^{-5} \mu\text{L}\cdot\text{min}^{-1}$ and $Q_o = 5Q_w = 5 \times 10^{-5} \mu\text{L}\cdot\text{min}^{-1}$; (b) from top to bottom: $Q_o = 0.5Q_w = 3 \times 10^{-5} \mu\text{L}\cdot\text{min}^{-1}$, $Q_o = 0.25Q_w = 3 \times 10^{-5} \mu\text{L}\cdot\text{min}^{-1}$, $Q_o = 0.2Q_w = 3 \times 10^{-5} \mu\text{L}\cdot\text{min}^{-1}$ and $Q_o = 0.3Q_w = 3 \times 10^{-5} \mu\text{L}\cdot\text{min}^{-1}$; (c) from top to bottom: $Q_o = 0.1Q_w = 4 \times 10^{-5} \mu\text{L}\cdot\text{min}^{-1}$, $Q_o = Q_w = 1 \times 10^{-4} \mu\text{L}\cdot\text{min}^{-1}$, $Q_o = 2.5Q_w = 1 \times 10^{-4} \mu\text{L}\cdot\text{min}^{-1}$, $Q_o = 5Q_w = 1 \times 10^{-4} \mu\text{L}\cdot\text{min}^{-1}$.

7.4 Conclusions and Outlook

We have developed and applied an on-chip flow control method for manipulating fluids flow in nanochannels. This method enables us to obtain flow rates in nanochannels as low as $10^{-5} \mu\text{L}\cdot\text{min}^{-1}$ ($< 1\text{pL}\cdot\text{s}^{-1}$). We have validated this method by demonstrating diffusional mixing of two liquids in nanochannels. By applying this method, we could also investigate immiscible two-phase (water and oil) flow in nanochannels.

References

- [1] Y. Rondelez, G. Tresset, K. V. Tabata, et al., *Nat. Biotechnol.* **2005**, 23, 361.
- [2] H. P. Lu, L. Y. Xun, X. S. Xie, *Science* **1998**, 282, 1877.
- [3] M. Nakano, J. Komatsu, S. Matsuura, et al., *J. Biotechnol.* **2003**, 102, 117.
- [4] S. L. Anna, N. Bontoux, H. A. Stone, *Appl. Phys. Lett.* **2003**, 82, 364.
- [5] Q. S. Pu, J. S. Yun, H. Temkin, et al., *Nano Lett.* **2004**, 4, 1099.
- [6] F. H. J. van der Heyden, D. J. Bonthuis, D. Stein, et al., *Nano Lett.* **2007**, 7, 1022.
- [7] Y. C. Wang, A. L. Stevens, J. Y. Han, *Anal. Chem.* **2005**, 77, 4293.
- [8] S. R. Liu, Q. S. Pu, L. Gao, et al., *Nano Lett.* **2005**, 5, 1389.
- [9] D. Kim, A. Raj, L. Zhu, et al., *Lab Chip* **2008**, 8, 625.
- [10] J. T. Mannion, C. H. Reccius, J. D. Cross, et al., *Biophys. J.* **2006**, 90, 4538.
- [11] A. Hibara, T. Tsukahara, T. Kitamori, *J. Chromatogr. A* **2009**, 1216, 673.
- [12] T. Tsukahara, K. Mawatari, A. Hibara, et al., *Anal. Bioanal. Chem.* **2008**, 391, 2745.
- [13] E. Tamaki, A. Hibara, H. B. Kim, et al., *J. Chromatogr. A* **2006**, 1137, 256.

Chapter 8

Monodisperse Femtoliter Droplet Formation using Nanochannel-Microchannel Interfaces

We demonstrate a novel method to create monodisperse femtoliter droplets by using the nanochannel-microchannel interface. A perfectly steady nanoscopic liquid filament can be formed by a geometric confinement which eventually gives rise to a stable production of nearly perfectly monodisperse femtoliter droplets. In a certain range of physical parameters and geometrical configurations, the liquid filament size and therefore the droplet size is determined by the nanochannel geometry, mainly its height which determines the Laplace pressure. Droplet diameter of 0.7~3.5 μm (aL~fL volume) can be produced using different size nanochannels.

8.1 Introduction

Microfluidics has received enormous attention because of the availability of fabrication and measurement methods [1-5]. Many areas of fluidic systems employ multiphase droplet-based microfluidics [6, 7], including inkjet printers [8], separation of biochemical samples [9], manipulation of biomolecules [10], bio-sensing [11], enhanced mixing for bio-sample reactions [12], biomolecular detection [13], microelectronic cooling [14], drug delivery devices [15], explosives detection [16], bubble computing [17], dairy analysis [18], interfacial tension measurement [19] and analysis of emulsions, foams, and bubble coalescence [20]. As general characteristics, the droplets should be as *fine, stable, monodisperse, reproducible, and controllable* as possible.

Precise understanding of biological or chemical functions requires the ability to isolate single molecules. To study single enzyme molecule activity we will need femtoliter size containers with a nM solution. Open container nanovials in solid substrates have been demonstrated, and have been scaled down to femtoliter [21]. However, such containers are not closed, water evaporates quickly, and the contents of the container is difficult to access and not reusable, with the consequences that it can not be independently controlled. In contrast, an emulsion in which one liquid forms droplets in another immiscible liquid is a simple and elegant way of creating very small closed containers which we will demonstrate here [22, 23].

Droplets can be formed using flow focusing, either by increasing shear gradients or by drawing the stream into a thin filament that breaks up by the Rayleigh-Plateau instability [24]. Droplets generated in microfluidic devices are commonly created by squeezing or shearing the dispersed liquid (oil or water) into the continuous liquid (water or oil). Droplet size depends on microchannel geometry [25-28], flow conditions [29-31] and fluid properties [32-35]. Many parameters make the droplet formation process complex and sensitive to many environmental influences.

Furthermore, the droplet size is limited by the microfabricated channel size (typically 10-100 μm). Therefore, a method is required which can not only produce monodisperse droplets, but is also stable and robust, and insensitive to changes in the flow rate.

The formation of a liquid filament is in most cases a mandatory preliminary step for producing of a droplet. A cylindrical liquid bridge is unstable when its length is longer than its circumference, the Plateau-Rayleigh limit [36]. The capillary instability can be induced by drawing the stream into a thin filament, a procedure widely applied in flow focusing devices. Notably, the dynamics of flow-focusing droplet-forming systems is largely independent of Ca for both low- Re and high- Re flows [37-41]. In these devices, an inner liquid thread can be created by an outer liquid shearing [31, 38, 40, 42]. However, the confinement is not stable and can be easily disturbed by dynamic fluctuations. A stable and strong confinement, on the other hand, can be obtained by solid structures (channels or holes). The size-confinement effect in nanochannels is distinct. Since the specific interfacial area of a nanochannel is very high, interfacial phenomena become increasingly important. The interface of nanochannel-microchannels has been used for active control of partitioning, electro-convection for mixing and pre-concentration of molecules [43-47]. Restraints in the photolithographic manufacturing techniques usually require the microfabricated nanochannel width to be $> 1 \mu\text{m}$. Nanochannels of sub-micrometer height can however be easily produced using a standard photolithography process. Such channels therefore have a high aspect ratio (width/height). Fortunately, also with high aspect ratio channels, which by consequence are asymmetric, highly monodisperse droplets can be obtained when compared to circular or square microchannels as demonstrated by Nakajima et al [48-50].

Here, we present a liquid stream which is confined to a thin filament using solid nanochannel walls. Due to the high capillary pressure inside the nanochannel the confinement is strong and stable over a wide range of flow dynamic conditions. We designed and fabricated a nano-microfluidic device which integrates nanochannels and microchannels. When two immiscible liquids moved from the nanochannel

environment to the microchannel environment, droplets formed at the nanochannel-microchannel interface. The droplet size was found to be solely determined by nanochannel geometry (height) over a wide range of flow conditions. The generated droplets were *stable* (over several months), *monodisperse* (highly patterned in 3D arrays) and *highly reproducible* over time. Above a critical flow rate larger monodisperse or polydisperse droplets could also be obtained.

8.2 Experimental

The channel structure used for the experiments is shown in Fig. 8.1 (top). The flow is regulated by the entire channel structure (see chapter 7). For the experiments described in this work, the nano-microfluidic interface is of prime importance, consisting of two identical inlets, a constriction channel and a microchannel, see Fig. 8.1 (bottom). The inlets and constriction channel are nanochannels with dimensions of height (h) = 150 ~ 900 nm, width (w) = 10, 20 or 50 μm and length (l) = 500 or 1000 μm ; and the microchannel dimensions are: height (H) = 10 μm , width (W) = 50 or 100 μm , length (L) = 5 mm.

The devices were fabricated using the same process as described in the previous chapter (see chapter 7), and the setup was also identical. The experiments were mainly done by using 1 wt% Tween80 aqueous solution (water phase) and hexadecane (oil phase). Other solutions, 0.3 wt% SDS aqueous solution and 1 wt% Span80 hexadecane solution were also been used to modify interfacial tensions. All chemicals were bought from Sigma-Aldrich Chemie GmbH (Germany) and used without further treatment. The viscosity of water and oil phases is 1 and 3 mPa.s, respectively. Water-oil interfacial tension varied in the range of 0.1 ~ 10 mN.m⁻¹ by combining different water and oil phases. Typically, flow rates of 10⁻⁵~10⁻³ $\mu\text{L}\cdot\text{min}^{-1}$ could be obtained in the nanochannel when a flow rate of 0.1~10 $\mu\text{L}\cdot\text{min}^{-1}$ was applied in the microchannel (split ratio~1:10⁴).

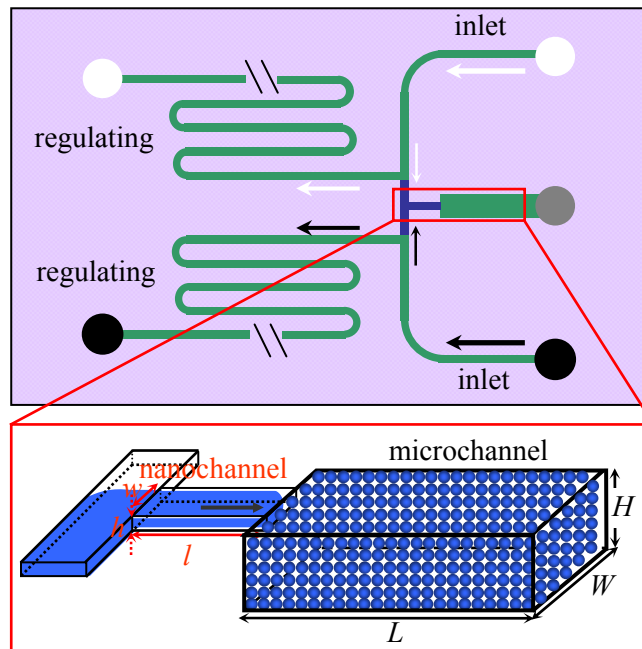


Figure 8.1 Sketch of the nano-micro fluidic chip design. When two immiscible liquids (oil – inner liquid and oil – outer liquid) step from the nanochannel to the microchannel monodisperse droplets form at the nano-microchannel interface.

8.3 Results and Discussion

8.3.1 Droplet formation at the nanochannel-microchannel interface

Oil and water are introduced from the two inlets. Our design enables us to obtain flow rates in the nanochannels as low as $10^{-5} \mu\text{L}\cdot\text{min}^{-1}$. The water phase spontaneously filled the channel as long as the device was connected to the syringe with water. However, the oil flowed through the microchannel without entering the nanochannel when the oil flow rate was below a certain threshold value (see chapter 7). As the oil flow was increased above this threshold, both oil and water flowed into the nanochannels. Oil and water met at the junction and flowed together in the constriction nanochannel. In

the nanochannel, the oil phase flowed either as droplets (Fig. 8.2a) or parallel with water (Fig. 8.2b). However, whenever oil (large droplets or thread) and water exited from the nanochannel into the microchannel, monodisperse oil-in-water droplets were spontaneously obtained.

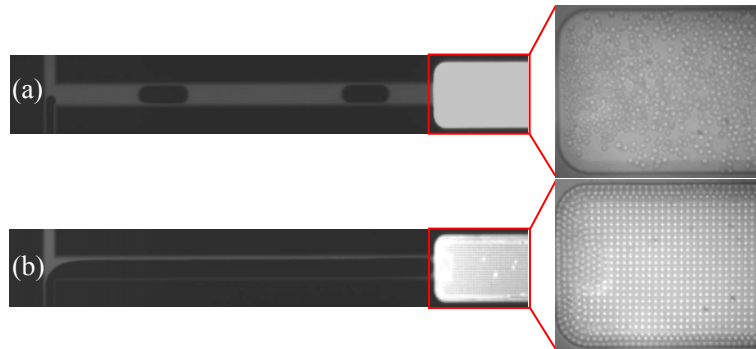


Figure 8.2 Snapshots of the droplets formation at the nanochannel-microchannel interface. (a) Oil droplets from nanochannel split to smaller droplets at the nanochannel-microchannel interface. (b) Oil flows parallel with water in the nanochannel, however, forms droplets at the nanochannel-microchannel interface. The device dimensions are: $h = 500$ nm, $w = 20$ μm , $l = 500$ μm , $H = 10$ μm and $W = 50$ μm .

In our device, the oil phase was pushed through the inlet nanochannel as a filament when the hydrodynamic pressure of oil was sufficiently large compared to the interfacial tension stress that acts at the oil-water interface. The filament width remained almost constant along the constriction channel up to a point close to the interface where the oil tip surprisingly shrank to a narrow filament (see Figs. 8.3(a-d)). Once the oil filament exited the nanochannel and entered the microchannel, its tip broke up into droplets (Fig. 8.3e).

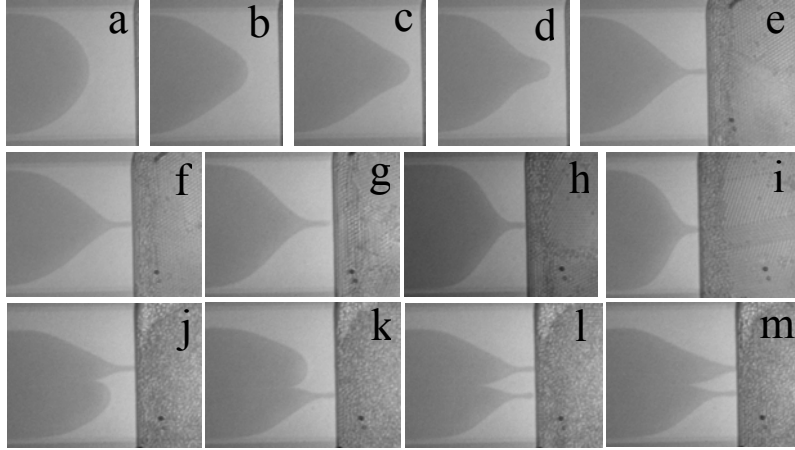


Figure 8.3 (a-e) Filament shrinking process; the time interval between images is 60 ms. (f-m) Filament shapes at different flow rates in nanochannels: (f) $Q_o = Q_w = 5 \times 10^5 \mu\text{L}\cdot\text{min}^{-1}$, (g) $Q_o = Q_w = 7.5 \times 10^5 \mu\text{L}\cdot\text{min}^{-1}$, (h) $Q_o = Q_w = 1.0 \times 10^4 \mu\text{L}\cdot\text{min}^{-1}$, (i) $Q_o = Q_w = 2.0 \times 10^4 \mu\text{L}\cdot\text{min}^{-1}$, (j-m) $Q_o = 5 \times 10^5 \mu\text{L}\cdot\text{min}^{-1}$ and $Q_w = 3 \times 10^5 \mu\text{L}\cdot\text{min}^{-1}$. The device dimensions are: $h = 250 \text{ nm}$, $w = 50 \mu\text{m}$, $l = 500 \mu\text{m}$, $H = 10 \mu\text{m}$, $W = 100 \mu\text{m}$ and $L = 5 \text{ mm}$.

Inside the nanochannel ($h = 250 \text{ nm}$, $w = 10 \mu\text{m}$, $l = 500 \mu\text{m}$), the Laplace pressure (due to interfacial force) is $\Delta P_L \approx 2\sigma/h = 2.0 \times 10^5 \text{ Pa}$. The dynamic (or inertial) pressure drop of oil phase is calculated using Bernoulli's equation $\Delta P_{\text{inert}} \approx \rho_o Q_o^2 / 2w^2 h^2 = O(10^4 Q_o^2)$, where ρ_o is the oil phase density and Q_o is the oil flow rate in nanochannel in units of $\mu\text{L}\cdot\text{min}^{-1}$. The viscous pressure drop along the oil filament can be calculated using the Hagen-Poiseuille equation $\Delta P_{\text{visc}} \approx 12\eta l Q / wh^3 = O(10^9 Q)$ ($1.3 \times 10^9 Q_w$ or $3.9 \times 10^9 Q_o$). The neglect of the inertial terms is therefore justified; however the viscous force has to be considered for the values of Q between $10^{-5} \mu\text{L}\cdot\text{min}^{-1}$ and $10^{-3} \mu\text{L}\cdot\text{min}^{-1}$ where the device is operated. In the nanochannel, stratified flow is obtained due to the channel confinement, although the capillary number $Ca = \eta v / \sigma$ falls in the range of $10^{-6} \sim 10^{-4}$ [51]. The oil filament width remains almost

constant along the constriction nanochannel away from the nanochannel exit. However, inside the microchannel the viscous force can be neglected due to the increase in both width and height. Therefore, inside the nanochannel close to the junction, the viscous pressure drop is negligible and the interfacial tension dominates and mainly determines the flow behavior. The oil filament then starts to shrink when it moves close to the nanochannel-microchannel interface due to the predominance of the interfacial tension. When the oil filament reaches the microchannel, a sudden drop in the Laplace pressure occurs, with a magnitude approximately equal to $2\sigma/h$, sucking the oil from the nanochannel and accelerating shrinking the oil thread to a thinner filament. The interfacial tension stress remains almost constant in the wide filament, but increases in this narrow section. The sudden drop of the interfacial tension at the interface of nanochannel and microchannel finally breaks up the oil filament tip into droplets by the capillary instability, driven by the minimization of surface energy. It has been found that for a fixed filament diameter the flow velocity does not affect the droplet size, a behavior similar to our observations [31, 52].

Depending on the flow rates, different oil filament shapes could be obtained, shown in Figs. 8.3(f-m). However, we have indications that the width of the filament tip is determined by the nanochannel height and therefore remains constant in the same device, which ensures the same sized droplets, though visual observations were too unreliable to clearly confirm this. When a perturbation is applied to the tip, for example by a small obstruction, the oil tip can split into two filaments with the same filament size close to the nanochannel exit (Figs. 8.3(j-m)). The same sized droplets were also observed broken up from the two oil filaments. Typically, we find that the oil filament shapes are obvious in small nanochannels and at low flow rates.

8.3.2 The dependence of the droplet size on the nanochannel height

In the limit of nanochannel confinement, the filament diameter at the nanochannel exit

is only determined by the Laplace pressure drop which is determined by the channel geometry. This filament diameter remains almost constant up to the breakup point since the pressure after the exit is negligible. In the Rayleigh breakup of a liquid jet into droplets at low Reynolds number, the droplet size is determined by the jet diameter and independent on flow velocity [31, 38]. The size of the droplets broken from an oil tip is therefore solely determined by the nanochannel geometry. In order to verify the geometry effects, different nanochannel heights h (160, 260, 520 and 900 nm), width w (10, 20 and 50 μm), and length l (500 and 1000 μm) have been used. The droplet diameter was measured in the microchannel. It was found that the nanochannel width and length have almost no effect on the droplet size; however, the nanochannel height significantly influences the generated droplet size. Figs. 8.4(a-d) show the droplets created in the devices with different nanochannel height. Fig. 8.4e shows the droplet size as a function of flow rate in different devices. At a constant height nanochannel, over a wide range of flow conditions, typically $Q = 10^{-5} \sim 10^{-3} \mu\text{L}\cdot\text{min}^{-1}$, the observed oil droplets were monodisperse and remained stable for at least several weeks. However, droplet size increased with the flow rates when the flow rates increased over a threshold ($Q > 10^{-3} \mu\text{L}\cdot\text{min}^{-1}$). Smaller nanochannel heights (narrower filaments) showed wider velocity operating ranges [31]. The insert demonstrates that the droplet size in the platform region increases linearly with the channel height. So far, there is no theoretical explanation for this.

We have also investigated liquid viscosity (0.3~10 mPa.s) and interfacial tension effects (0.01~30 mN.m⁻¹). We did not observe significant droplet size variation with liquid viscosity and interfacial tension in the platform regime. However, the transition values from the platform region to the velocity-dependent region were influenced by the relative liquid viscosities and interfacial forces. Typically, the frequency of droplet formation in these devices ranged from 10 to 10⁴ Hz, dependent on the flow rate. The frequency could be increased by integrating parallel channels.

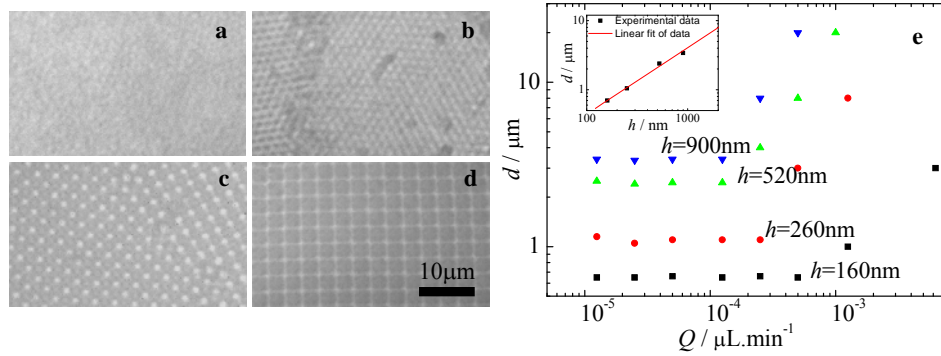


Figure 8.4 The microphotographs of monodisperse droplets in different devices: (a) $h = 160$ nm, (b) $h = 260$ nm, (c) $h = 520$ nm and (d) $h = 900$ nm. The images were taken using transmitted light. (e) The oil droplet diameter as a function of oil flow rates at $Q_o = Q_w$. The scale bars are $10\ \mu\text{m}$.

8.3.3 Transitions

The transition from the monodisperse droplets region to the region of flow rate-dependent droplet size can be understood by considering a competition of two time scales [53, 54]. These two time scales are: the capillary time t_c for the growth of interfacial disturbance and the flow time t_f for the fluid convection. The capillary disturbance is dominated by the interfacial tension and viscosity, $t_c \sim d_f \eta_o / \sigma$, where d_f is the characteristic filament diameter. t_f is expressed as the time needed for the oil phase traveling from the thin oil filament to the forming droplet, $t_f \sim d_f^3 / Q_o$. The capillary disturbance occurs as soon as the oil filament tip reaches the exit of the nanochannel. If $t_c \leq t_f$ the pinch-off the oil filament tip occurs immediately at the nanochannel-microchannel interface. The droplet size is thereby determined by the filament diameter. If $t_c > t_f$, the pinch-off speed is lower than the fluid convection speed. There is more fluid transported into a droplet when it is pinched off from the oil filament. Therefore, the droplet size is dependent on the oil flow rate. The higher the oil flow rate is applied, the shorter the t_f is, thus the larger the droplet is (see Fig. 8.5).

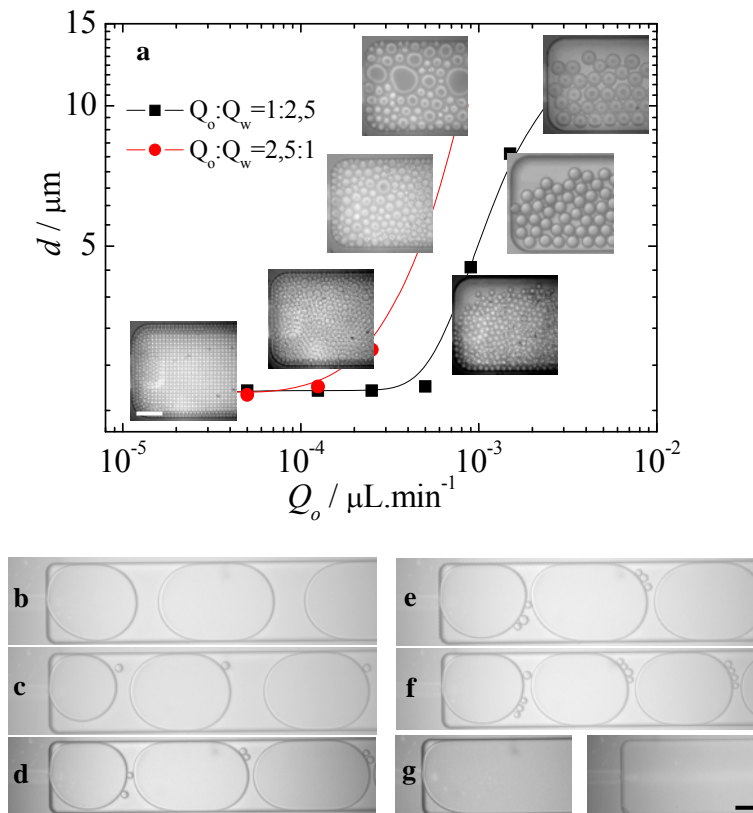


Figure 8.5 (a) The influence of flow rate on droplet size and polydispersity. Images along the red line were taken at $Q_o = 0.5, 1.2, 1.5$ and $2.0\ \mu\text{L}\cdot\text{min}^{-1}$ with Q_o to Q_w ratio of 1:2.5. Images along the black line were taken at $Q_o = 0.6, 2.0, 4.0$ and $5.0\ \mu\text{L}\cdot\text{min}^{-1}$ with Q_o to Q_w ratio of 2.5:1. (b-f) Dripping: (b) without satellite droplet, (c) one satellite droplet, (d) two satellite droplets, (e) three satellite droplets and (f) four satellite droplets. (g) Threading. The nanochannel height is $500\ \text{nm}$ for (a) and $900\ \text{nm}$ for (b-g). The scar bars are $20\ \mu\text{m}$.

On the other hand, at a high oil-to-water flow rate ratio, when the oil flow rate increases above a certain limit, the dynamic energy becomes sufficiently large to overcome the energy barrier (stabilized by surfactants) of droplet coalescence. The droplets start to rupture and coalesce into larger entities which induces polydispersity,

see Fig. 8.5a (circular dots). By analysis of t_c and t_f , we can obtain that t_c increases with η_o but decreases with σ . This is coincident with the experimental result that, by increasing the water phase viscosity or decreasing the water-oil interfacial tension, the transition occurs earlier. t_c and t_f are proportional to d_f and d_f^3 , respectively, therefore, smaller filaments (smaller nanochannel) show a wider velocity operating range and transit relatively later than that of the bigger filaments (larger nanochannel).

During the transition between regions, satellite droplets with different number and size have also been observed, as shown in Figs. 8.5(b-f). Continuous stratified flows without droplet formation could always be observed at high absolute or relative oil and water flow rates (Fig. 8.5g).

8.4 Conclusions and Outlook

We have demonstrated a strong and stable confinement of the inner liquid during emulsification using solid nanochannels. This confinement induces a stable oil (inner liquid) filament in the nanochannel even at low capillary numbers due to the high Laplace pressure. When the oil transits from a nanochannel to a microchannel, the change of confinement causes a large change in Laplace pressure. As long as the Laplace pressure dominates, it induces a stable and constant thin oil filament at the exit of the nanochannel. Over a wide range of absolute and relative flow rates, highly stable and monodisperse small (0.7~3.5 μm in diameter) droplets were obtained by breaking up the oil filament at the nanochannel-microchannel interface. The smaller nanochannel heights demonstrated wider flow rate operating ranges. The droplet size was linearly related to the nanochannel height which determines the Laplace pressure at very high aspect ratio. An increase in water and oil flow rates above a certain threshold generated bigger droplets without or with different satellite droplets, as well as threading, generating parallel flows of oil and water. The femtoliter to attoliter droplets are small containers which will on average encapsulate one molecule per droplet if the analyte concentration is in nM, which would be a promising tool for single molecular studies.

References

- [1] B. Zheng, J. D. Tice, L. S. Roach, et al., *Angew. Chem. Int. Ed.* **2004**, *43*, 2508.
- [2] M. W. Losey, R. J. Jackman, S. L. Firebaugh, et al., *J. Microelectromech. Syst.* **2002**, *11*, 709.
- [3] J. Tien, C. M. Nelson, C. S. Chen, *PNAS* **2002**, *99*, 1758.
- [4] D. Sinton, *Microfluid. Nanofluid.* **2004**, *1*, 2.
- [5] A. van den Berg, T. S. J. Lammerink, *Micro total analysis systems: Microfluidic aspects, integration concept and applications*, Vol. 194, Springer-Verlag, Berlin 33 **1998**.
- [6] L. Shui, J. C. T. Eijkel, A. van den Berg, *Adv. Colloid Interfac.* **2007**, *133*, 35.
- [7] A. Gunther, K. F. Jensen, *Lab Chip* **2007**, *7*, 399.
- [8] D. B. van Dam, C. Le Clerc, *Phys. Fluids.* **2004**, *16*, 3403.
- [9] T. Fujimura, A. Ikeda, S. Etoh, et al., *Jpn J. Appl. Phys. I* **2003**, *42*, 4102.
- [10] H. C. Lo YC, Hsu W, Wang C, "Neural guidance by open-top SU-8 microfluidic channel ", presented at *ICMENS*, **2004**.
- [11] K. G. Wang, S. L. Yue, L. Wang, et al., *Microfluid. Nanofluid.* **2006**, *2*, 85.
- [12] I. D. Yang, Y. F. Chen, F. G. Tseng, et al., *J. Microelectromech. S.* **2006**, *15*, 659.
- [13] F. G. Tseng, K. H. Lin, H. T. Hsu, et al., *Sensor Actuat. a-Phys.* **2004**, *111*, 107.
- [14] R. H. Nilson, S. W. Tchikanda, S. K. Griffiths, et al., *Int. J Heat Mass Tran.* **2006**, *49*, 1603.
- [15] A. J. Chung, D. Kim, D. Erickson, *Lab Chip* **2008**, *8*, 330.
- [16] B. D. Piorek, S. J. Lee, J. G. Santiago, et al., *PNAS* **2007**, *104*, 18898.
- [17] M. Prakash, N. Gershenfeld, *Science* **2007**, *315*, 832.
- [18] O. Skurtys, J. M. Aguilera, *Food Biophys.* **2008**, *3*, 1.
- [19] J. H. Xu, S. W. Li, W. J. Lan, et al., *Langmuir* **2008**, *24*, 11287.
- [20] J. G. Kralj, M. A. Schmidt, K. F. Jensen, *Lab Chip* **2005**, *5*, 531.
- [21] Y. Rondelez, G. Tresset, K. V. Tabata, et al., *Nat. Biotechnol.* **2005**, *23*, 361.
- [22] H. P. Lu, L. Y. Xun, X. S. Xie, *Science* **1998**, *282*, 1877.
- [23] M. Nakano, J. Komatsu, S. Matsuura, et al., *J. Biotechnol.* **2003**, *102*, 117.
- [24] S. L. Anna, N. Bontoux, H. A. Stone, *Appl. Phys. Lett.* **2003**, *82*, 364.
- [25] B. Dollet, W. van Hove, J. P. Raven, et al., *Phys. Rev. Lett.* **2008**, *1*.
- [26] S. Sugiura, M. Nakajima, M. Seki, *Langmuir* **2002**, *18*, 3854.
- [27] T. S. Ravigururajan, *J. Heat Transf.-Trans. ASME* **1998**, *120*, 485.
- [28] D. R. Link, S. I. Anna, D. A. Weitz, et al., *Phys. Rev. Lett.* **2004**, *92*, 545031.
- [29] P. Garstecki, M. J. Fuerstman, H. A. Stone, et al., *Lab Chip* **2006**, *6*, 437.
- [30] L. Martín-Banderas, M. Flores-Mosquera, P. Riesco-Chueca, et al., *Small* **2005**, *1*, 688.
- [31] A. S. Utada, A. Fernandez-Nieves, H. A. Stone, et al., *Phys. Rev. Lett.* **2007**, *99*.
- [32] A. M. Ganan-Calvo, P. Riesco-Chueca, *J Fluid Mech* **2006**, *553*, 75.
- [33] J. D. Tice, A. D. Lyon, R. F. Ismagilov, *Anal. Chim. Acta.* **2004**, *507*, 73.
- [34] A. M. Ganan-Calvo, M. Perez-Saborid, J. M. Lopez-Herrera, et al., *Eur. Phys. J. B* **2004**, *39*, 131.
- [35] P. Lam, K. J. Wynne, G. E. Wnek, *Langmuir* **2002**, *18*, 948.
- [36] Y. J. Chen, R. Abbaschian, P. H. Steen, *J. Fluid Mech.* **2003**, *485*, 97.
- [37] P. Garstecki, I. Gitlin, W. DiLuzio, et al., *Appl. Phys. Lett.* **2004**, *85*, 2649.
- [38] A. M. Ganan-Calvo, J. M. Gordillo, *Phys. Rev. Lett.* **2001**, *87*, 2745011.
- [39] J. M. Gordillo, M. Perez-Saborid, A. M. Ganan-Calvo, *J. Fluid. Mech.* **2001**, *448*, 23.
- [40] A. M. Ganan-Calvo, *Phys. Rev. Lett.* **1998**, *80*, 285.
- [41] A. Barrero, A. M. Ganan-Calvo, J. Davila, et al., *Phys. Rev. E* **1998**, *58*, 7309.
- [42] O. Amyot, F. Plouraboue, **2007**, *19*.

-
- [43] Y. C. Wang, A. L. Stevens, J. Y. Han, *Anal. Chem.* **2005**, *77*, 4293.
[44] S. R. Liu, Q. S. Pu, L. Gao, et al., *Nano Lett.* **2005**, *5*, 1389.
[45] Q. S. Pu, J. S. Yun, H. Temkin, et al., *Nano Lett.* **2004**, *4*, 1099.
[46] D. Kim, A. Raj, L. Zhu, et al., *Lab Chip* **2008**, *8*, 625.
[47] J. T. Mannion, C. H. Reccius, J. D. Cross, et al., *Biophys. J.* **2006**, *90*, 4538.
[48] S. Sugiura, M. Nakajima, M. Seki, *Langmuir* **2002**, *18*, 5708.
[49] I. Kobayashi, S. Mukataka, M. Nakajima, **2004**, *279*, 277.
[50] S. Sugiura, T. Kuroiwa, T. Kagota, et al., *Langmuir* **2008**, *24*, 4581.
[51] L. Shui, F. Mugele, A. van den Berg, et al., *Appl. Phys. Lett.* **2008**, *93*, 1531131.
[52] T. M. Squires, S. R. Quake, *Rev. Mod. Phys.* **2005**, *77*, 977.
[53] B. Ambravaneswaran, H. J. Subramani, S. D. Phillips, et al., **2004**, *93*.
[54] C. F. Zhou, P. T. Yue, J. J. Feng, **2006**, *18*.

Chapter 9

Liquid Crystallography: 3D Microdroplet Arrangements Using Microfluidics

Monodisperse liquid particles (femtoliter oil-droplets) are shown to self-organize into 3D close-packed face-centered cubic (fcc) arrangements. Droplets were formed at a nanochannel/microchannel interface, and the formation of these arrangements occurred at certain flow rate ratios of oil and water. The remarkably robust and stable structures formed in two different ‘crystallographic’ orientations of a face-centered cubic lattice, fcc(100) and fcc(111), as evidenced by the occurrence of square and hexagonal patterns at the plane adjacent to the channel wall. The orientation was found to depend on the oil-to-water flow rate ratio. Similar to solid state crystals, ‘crystallographic’ features were observed, such as dislocation lines and defects. The 3D arrays presented in this work could provide platforms for a number of applications.

A manuscript is submitted.

9.1 Introduction

Pattern formation in general is ubiquitous in nature [1-3]; fluid systems in particular provided a fertile ground for studies of the self-organization of complex superstructures [4, 5]. Periodic organization of chemical, mechanical, optical, electrical or magnetic properties is important in materials. Regular 3D arrays of solid particles have shown many possible applications, for example as photonic crystal structures, liquid chromatography packing and data storage [6-10]. The use of liquid particles instead of solid particles leads to a simple way of tuning the array properties due to the large variation in chemical and optical properties of liquids.

Liquid flows confined within microfluidic devices offer specific and unique fluid dynamics and boundary conditions, which may be used to induce pattern formation of many sorts. Recently, the creation and flow of nano- and micro-particles (colloid particles, liquid droplets or gas bubbles) in microfluidic systems has attracted considerable attentions [11-15]. The micrometric length scale is sufficiently small to warrant neglecting inertial and gravity effects in the fluid (low Reynolds and Bond numbers) [16, 17]. These dynamical systems can therefore be generally described by simple physical models involving a limited number of variables.

Several groups have investigated the formation and periodic 2D arrangements of fluid particles (liquid droplets or gas bubbles) inside microchannels [18-21]. Generally, highly complex structures result from the system drive to minimize the local interfacial energies. In this respect, fluid particles, which are ‘soft’ and deformable, are distinctly different from solid particles. The self-organization of the fluid particles is seen to be determined by the particle size, the channel geometry, the volume fractions and the relative fluid pressures. In most previous reports on droplet formation and organization in microchannels, droplets were created by shearing the dispersed liquid (oil or water) into the continuous phase (water or oil). Typically, the volume of the generated droplets (or bubbles) for these systems is comparable to or larger than the volume of the largest sphere that can be inscribed inside the microchannel. In these

cases only 2D structures will be formed.

In contrast to these previous results, in this work we report on the creation of droplets with a diameter considerably smaller than the microchannel height, therewith allowing for multiple layers of droplets to be assembled inside the microchannel. For their formation we use a junction between a nanochannel and microchannel, where droplets are formed by capillary instability. Depending on specific flow conditions, the high-density monodisperse microdroplets are shown to self-organize into 3D close-packed face-centered cubic (fcc) superstructures after being generated and flowing together with a continuous water phase in microfluidic channels. The remarkably rigid and stable close-packed structure formed in the microchannel exhibits itself in square and hexagonal patterns at the plane adjacent to the channel wall, corresponding to two ‘crystallographic’ orientations, (100) and (111) of the same fcc structure. Different regimes, i.e. ‘phases’ of the droplet arrangements, depend strongly on the specific flow conditions. Variation of the (relative) flow rates of oil and water thus enabled construction of a ‘flow phase’ diagram. Similar to solid state crystals, we distinguish ‘crystallographic’ features, such as dislocation lines and defects in our dynamical fluidic systems. For the first time, we present the 3D (multilayer) crystallography of small monodisperse liquid droplets in a microfluidic device.

9.2 Experimental

9.2.1 Device design

For the experiments described in this chapter, we use a nano-micro fluidic device which integrates nanochannels and a microchannel, as schematically shown in Fig. 9.1. It consists of two identical inlets, a constriction channel and a microchannel. The inlets and constriction channel are nanochannels with dimensions of height (h) = 500 nm, width (w) = 10 μm and length (l) = 500 μm ; and the microchannel dimensions are that height (H) = 10 μm , width (W) = 50 or 100 μm , length (L) = 5 mm.

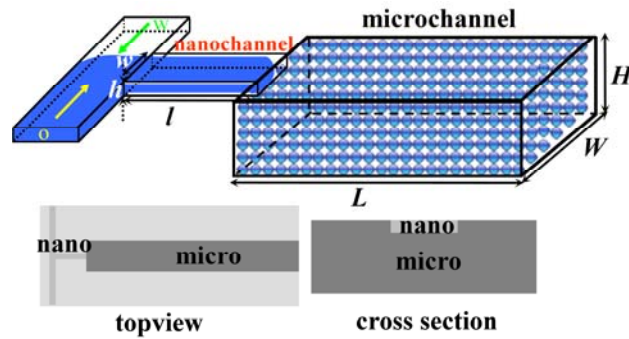


Figure 9.1 Schematic representation of the channel structure. h , w and l are nanochannel height, width and length; and H , W , L are microchannel height, width and length. w and o indicate water and oil phases, respectively.

9.2.2 Fabrication and setup

The devices were fabricated in glass using standard microlithographic techniques. Nanochannels and microchannels were etched into a borosilicate glass wafer using BHF and 25% HF solutions, respectively. The connection holes were drilled in a second borosilicate glass wafer using powder blasting techniques. Subsequently, these two wafers were aligned and thermally bonded together. We diced the bonded wafers to 10 mm \times 20 mm sized chips, which were mounted in a home-made chip holder and connected to gas-tight syringes (Microliter Syringes, Hamilton) *via* nanoport connectors (Upchurch Scientific). Harvard syringe pumps (PHD 22/2000, Harvard Apparatus) were used to drive the liquid flow. The two-phase flow was visualized by an inverted microscope (Leica DMIRM) and recorded using a CCD camera (Orca ER).

9.2.3 Fluids

The water phase was made fluorescent (appearing white in the microphotographs) by dissolving fluorescein sodium salt (Sigma-Aldrich Chemie GmbH, Germany) in de-

ionized water at a final concentration of 0.01 mol.L^{-1} ($\eta_w = 1 \text{ mPa.s}$). The organic phase (dark in the images) consisted of hexadecane (Sigma-Aldrich Chemie GmbH, Germany) without any added fluorescent markers ($\eta_o = 3 \text{ mPa.s}$). Surfactants were used to stabilize generated droplets. The surfactants used were sodium dodecyl sulfate ($\text{CH}_3(\text{CH}_2)_{11}\text{OSO}_3\text{Na}$, SDS 99+%, Sigma-Aldrich Chemie GmbH, Germany), Tween80 (Sigma-Aldrich Chemie GmbH, Germany), and Span80 (Sigma-Aldrich Chemie GmbH, Germany). Solutions were prepared by dissolving hydrophilic surfactants (SDS and Tween80) in water or hydrophobic surfactant (Span80) in hexadecane. The surfactant concentrations were in all cases above the critical micelle concentrations. Solutions were degassed under vacuum for 1 hour.

9.3 Results and Discussion

9.3.1 3D microdroplet arrangements

Fig. 9.1 shows the scheme of our nano-micro fluidic device which consists of a nanochannel section connected to a microchannel. Oil (inner) and water (outer) phases are introduced from two inlets into the nanochannel in continuous flow. When oil and water are forced to flow together from the hydrophilic nanochannel into the microchannel, oil-droplets are formed in the water phase at the junction of the nanochannel and microchannel. Over a wide range of flow conditions (flow rates of $10^{-5} \sim 10^{-3} \mu\text{L.min}^{-1}$), the diameter of the observed oil droplets is independent of flow rate and remarkably monodisperse. At the low flow rates used, the capillary pressure difference between nanochannel and microchannel is expected to dominate droplet formation. Since this pressure difference is constant and dominates droplet formation, droplets obtained are monodisperse. By varying the nanochannel and microchannel geometry, we can easily obtain monodisperse droplets with size in the range of $0.7 \sim 3.5 \mu\text{m}$. For the experiments reported here, we use a device with $h = 500 \text{ nm}$, $w = 10 \mu\text{m}$, $l = 500 \mu\text{m}$, $H = 10 \mu\text{m}$, $W = 50 \text{ or } 100 \mu\text{m}$ and $L = 5 \text{ mm}$. The droplets are

$2.5 \pm 0.1 \mu\text{m}$ in diameter. The emulsion that formed remained stable for at least several weeks.

Optical microscopy on the microchannel region reveals that under the proper flow conditions, the oil-droplets self-organize into highly ordered 3D structures in the microchannel. Depending on the relative flow rates of water and oil, different droplet arrangements at the plane adjacent to the channel wall are observed, as displayed in Fig. 9.2. Different ‘phases’ of these droplet arrangements can be distinguished when the arrangement observed at the plane is taken as the criterion: disordered, square, hexagonal and coalescent. The corresponding FFT (Fast Fourier Transform) images are also shown. The FFT images clearly show the highly ordered, nearly perfect square (Fig. 9.2b) and hexagonal (Fig. 9.2c) arrangements of the liquid droplets at the plane, as witnessed by the periodic structures. The absence of bright spots in the other two FFT images (Figs 9.2a and 9.2d) is in agreement with the random distribution of droplets in the disordered and coalescent ‘phases’. Careful inspection of the FFT image for the disordered phase reveals a ring-like structure. The concentric rings represent the short-range, non-directional ordering within the droplet phase, which arises from the fact that all droplets have the same size and that there is a net short-range steric repulsion. For the coalescent phase, the high degree of polydispersity leads to the absence of such a concentric ring pattern.

The flow conditions were seen to affect the process of the droplet formation and the self-organization into the ordered superstructures. In Fig. 9.2e the occurrence of the various different patterns at the plane adjacent to the channel wall are shown as a function of the oil and water volume flow rates (Q_o and Q_w , respectively). In this flow map, four well-separated regimes are found: (i) At low oil-to-water flow rate ratios ($Q_o < 2Q_w$) the oil-droplets flow disorderly in the microchannel after generation. (ii) When the flow rate ratio rises above a certain threshold ($Q_o > 2Q_w$), the oil droplets self-organize into ordered square patterns at the plane. (iii) At still higher oil-to-water flow rate ratios ($Q_o > 7Q_w$) a hexagonal pattern is observed at the plane. (iv) Above a certain oil flow rate (typically $Q_o > 3 \times 10^{-4} \mu\text{L}\cdot\text{min}^{-1}$) the oil droplets start to coalesce in the

microchannel. These observed patterns remain intact when the droplets continuously flow downstream, and slightly reorganize with time (interchanging droplets and rotation of domains).

As mentioned in the experimental section, different surfactants were used to create stable droplets. Very similar flow phases are obtained using various surfactants: 1 wt% Tween80, 0.3 wt% SDS and 1 wt% Span80. Apparently, the precise nature of the surfactant does not play a significant role in defining microdroplet size and self-organization.

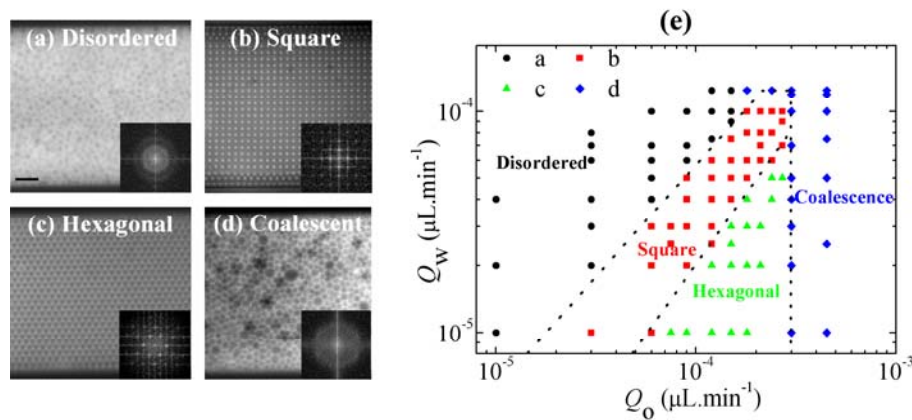


Figure 9.2 (a-d) Snapshots of oil-droplets organizations in the plane adjacent to the microchannel wall. The insets represent their corresponding FFT, which reveal random organizations for (a) disordered and (d) coalescent structures, and nearly perfect (b) square and (c) hexagonal organizations in microchannels. (e) Structural domains vary with the volume flow rates of oil (Q_o) and water (Q_w). The organization is considered as square if > 50% of the area is occupied by square lattice. The same criterion was applied for the hexagonal case. The surfactant used in these experiments was Tween80 at 1 wt% concentration. The scar bar is 10 μm .

9.3.2 Liquid crystallography

The square and hexagonal arrangements unambiguously demonstrate the well-defined close-packed 3D lattices of microdroplets. Fig. 9.3a show typical microscopic images of hexagonal and square arrangements of the droplets observed at the plane adjacent to the channel wall. Since the oil-droplet diameter is 2.5 μm and the channel height amounts to 10 μm , there are typically several (4-5) layers of droplets in the microchannel, as could be visualized by moving the focal plane of the microscope deeper into the channel (Fig. 9.3b, red solid and blue dotted lines indicate patterns in two different layers). If we hypothesize that both observed patterns correspond to the same specific 3D organization but viewed in different orientations, the observed distances between the droplets in the square and hexagonal arrangements should be related. This was indeed confirmed, and we conclude that the droplets with diameter d (due to their close packing, d is equal to the minimum center-to-center distance between droplets) are both organized in a face-centered cubic (fcc) structure (see Fig. 9.3c). The size of the corresponding unit cell (indicated by the white cube in Fig. 9.3c) with lattice parameter a amounts to $a = d\sqrt{2} = 3.5 \mu\text{m}$, since the center-to-center distance between the droplets in the hexagonal pattern corresponds to the half of the diagonal of a face of this unit cell. The highly ordered patterns we observe in Figs 9.3a and 9.3b are thus related to two different “crystallographic” orientations of the fcc arrangement in both droplet arrays. The square pattern corresponds to the (100) plane, while the hexagonal arrangement corresponds to the (111) plane of the fcc structure. The organized structures proved to be very stable (typically for several weeks) and highly reproducible under the same flow conditions. This indeed proves that the patterning can be solidified to form 3D structures which will be very useful for real life applications [8-10, 22, 23].

Since the structures exist in the dynamical microfluidic system, perturbations can induce instability. Therefore, the system does not always display perfect packing of the droplets in the microfluidic device. We observed ‘grain’ boundaries, ‘dislocations’ and vacancy defects in the patterns, as well as the coexistence of square and hexagonal patterns (Fig. 9.4). Owing to the fluorescence of the water phase, vacancies in the oil droplet ‘crystals’ are exposed as the bright spots in the patterns (both in square and hexagonal arrangements).

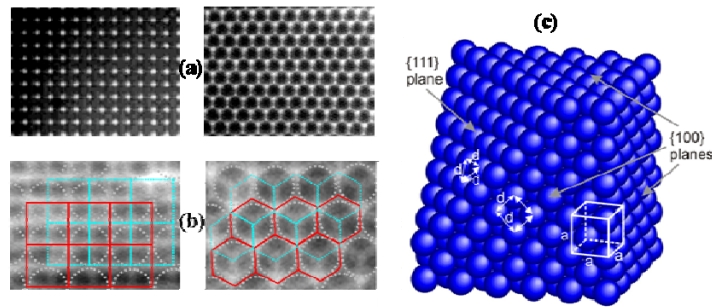


Figure 9.3 (a) Self-organized square (left) and hexagonal (right) arrangements observed at the plane adjacent to the channel wall. (b) Microphotographs demonstrate two layers of the arrangements where the dotted circles indicate oil droplets, the red solid lines and blue dotted lines are drawn to indicate the arrangements in the two different layers. (c) Schematic representation of the face-centered cubic (fcc) crystal structure; the square and hexagonal patterns correspond to fcc (100) and (111) planes, respectively. The white cube frame indicates a unit cell, with lattice parameter a , while the smallest center-to-center particle distance d is indicated in the different planes.

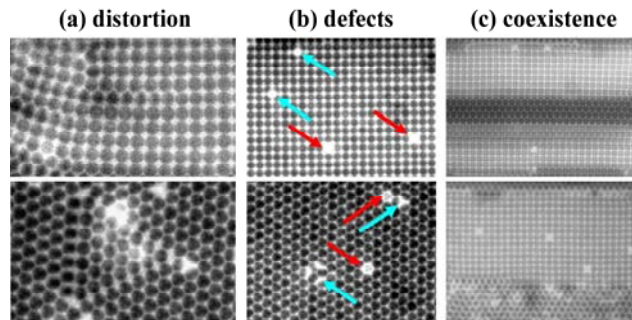


Figure 9.4 Different dynamic organizations of microdroplets. (a) Distortion in square (top) and hexagonal (bottom) patterns. (b) Defects in square (top) and hexagonal (bottom) patterns. The red arrows indicate defects in the top layer, or a deeper layer where the microdroplets have the identical position. The blue arrows indicate vacancies which are in the layer beneath the top layer. (c) Coexistence of square and hexagonal patterns in the microchannel.

9.3.3 Phase transition

Now we turn to the two different orientations of the fcc superstructures, i.e. regimes (ii) and (iii) described above, as witnessed by the square and hexagonal arrangement of microdroplets at the plane adjacent to the channel wall. We believe that the oil volume fraction $V_f = Q_o / (Q_w + Q_o)$ mainly determines the observed arrangements. The square arrangement occurs at $V_f > 0.67$. Since in this arrangement the vertical space needed in the microchannel for n layers is $(n-1) / \sqrt{2} d + d$, five layers need $9.57 \mu\text{m}$ and thus will fit into the channel. Assuming 5 droplet layers, the packing density is 0.65, agreeing well with the observed transition from disordered to square at $V_f = 0.67$. The transition from square to hexagonal is seen to occur approximately at $V_f > 0.87$. This is higher than the packing density for the fcc structure (0.74), therefore some deformation of the oil droplets is expected to occur. For example, five layers in a hexagonal arrangement will give a packing density of 0.75 but need a channel height of $10.64 \mu\text{m}$ so that deformation will occur. Such droplet deformation was indeed observed at high oil flow rate ratios.

A sufficiently large perturbation was seen to lead to a transition of the system from one organization pattern to another, i.e. to a reorientation of the 3D superstructure. As already shown in Fig. 9.2e, a hexagonal to square transition is observed when decreasing the oil-to-water volume flow ratio. Inversely, upon increasing the relative oil flow rate, a transition from square to hexagonal arrangement is induced.

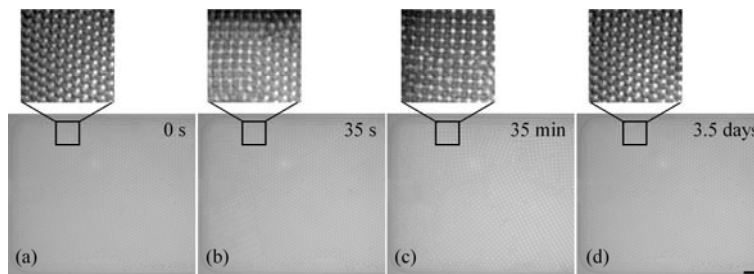


Figure 9.5 Transition of hexagonal-square-hexagonal at the flow-free state: (a) hexagonal, (b) hexagonal + square, (c) square and (d) hexagonal. The scar bar is $10 \mu\text{m}$.

The reorientation mechanism described in the previous paragraph pertains to quasi-static conditions, i.e. in which the fluid flow is constant. Now we consider the situation in which the flow of both water and oil is abruptly interrupted; the new situation is referred to as the flow-free state. Starting from a quasi-static state with hexagonally arranged droplets at the plane, initially we observe a gradual transition from the hexagonal to the square ‘phase’, typically within a few hours (Figs. 9.5(a-c)). Assuming that the hexagonal fcc orientation is accompanied by a slight droplet deformation, we hypothesize that the system in this phase relaxes to the lower energy state in which droplets are non-deformed. For this to happen the oil volume fraction inside the microchannel must decrease, and the source of water for this process could be the microchannel water outlet reservoir and the emulsion outlet reservoir. Simultaneously, a slight retraction of the oil thread into the nanochannel is indeed observed, which can also only occur as the result of an influx of water. After prolonged relaxation of the flow-free state, typically for a few days, we often observe a transition from square to hexagonal arrangement (Figs.9.5c and 9.5d). In this case, we can account for the observations by considering the gradual disappearance of water from the system by evaporation from the open outlet reservoir. Therefore, at the free-flow state, we can obtain a hexagonal-square-hexagonal transition starting from a hexagonal arrangement or a square-hexagonal transition starting from a square arrangement.

9.4 Conclusions and Outlook

We have demonstrated a new nano-micro fluidic system which enables multilayer emulsion formation and patterning. Oil-droplets, created at the junction of the nanochannel and microchannel, are independent of flow rates, highly monodisperse and remarkably stable over a wide range of flow conditions. Over a large range of absolute and relative flow rates, the microdroplets self-organize into close-packed 3D superstructures, which can be identified as a face-centered cubic lattice. Different orientations of this face-centered cubic lattice, depending on the specific flow conditions, are observed by square or hexagonal droplet arrangements in the plane

adjacent to the channel wall, corresponding to (100) and (111) facets. In these dynamical multiphase fluidic systems, perturbations, mainly from the flow of the liquids, induce dislocation lines and defects, and even transition between square and hexagonal patterns. This study is expected to lead to a better understanding of 3D periodic close-packed two-phase metastable systems and their applications in real life. Incorporation of large quantities of monodisperse domains in an organized fashion within suitable matrices is useful. The liquid particle patterning offers a flexible alternative to solid particle arrays in use for, for example, photonic crystal structures (opals and inverted opals), liquid chromatography packings and data storage [9, 10, 22-26].

References

- [1] E. Cox, *Nature* **1998**, 396, 731.
- [2] S. H. Lim, S. Che, H. Yoshitake, et al., *Chem. Lett.* **2005**, 34, 792.
- [3] L. J. Fu, T. Zhang, Q. Cao, et al., *Electrochem. Commun.* **2007**, 9, 2140.
- [4] J. P. Gollub, J. S. Langer, *Rev. Mod. Phys.* **1999**, 71, S396.
- [5] M. C. Cross, P. C. Hohenberg, *Rev. Mod. Phys.* **1993**, 65, 851.
- [6] Y. A. Vlasov, X. Z. Bo, J. C. Sturm, et al., *Nature* **2001**, 414, 289.
- [7] S. K. Lee, G. R. Yi, S. M. Yang, *Lab Chip* **2006**, 6, 1171.
- [8] S. A. Vanapalli, C. R. Iacovella, K. E. Sung, et al., *Langmuir* **2008**, 24, 3661.
- [9] C. W. Kuo, J. Y. Shiu, K. H. Wei, et al., *J. Chromatogr. A* **2007**, 1162, 175.
- [10] A. Ethirajan, U. Wiedwald, H. G. Boyen, et al., *Adv. Mater.* **2007**, 19, 406.
- [11] N. V. Dziomkina, G. J. Vancso, *Soft Matter* **2005**, 1, 265.
- [12] M. Joanicot, A. Ajdari, *Science* **2005**, 309, 887.
- [13] T. Thorsen, S. J. Maerkl, S. R. Quake, *Science* **2002**, 298, 580.
- [14] B. H. Weigl, P. Yager, *Science* **1999**, 283, 346.
- [15] N. J. Carroll, S. B. Rathod, E. Derbins, et al., *Langmuir* **2008**, 24, 658.
- [16] T. M. Squires, S. R. Quake, *Rev. Mod. Phys.* **2005**, 77, 977.
- [17] L. Shui, J. C. T. Eijkel, A. van den Berg, *Sensor Actuat. B-Chem.* **2007**, 121, 263.
- [18] T. Thorsen, R. W. Roberts, F. H. Arnold, et al., *Phys. Rev. Lett.* **2001**, 86, 4163.
- [19] J. P. Raven, P. Marmottant, *Phys. Rev. Lett.* **2006**, 97, 154501.
- [20] P. Garstecki, G. M. Whitesides, *Phys. Rev. Lett.* **2006**, 97, 024503.
- [21] A. Woodward, T. Cosgrove, J. Espidel, et al., *Soft Matter* **2007**, 3, 627.
- [22] G. M. Gratson, F. Garcia-Santamaria, V. Lousse, et al., *Adv. Mater.* **2006**, 18, 461.
- [23] A. Penrose, P. Myers, K. Bartle, et al., *Analyst* **2004**, 129, 704.
- [24] G. R. Yi, S. J. Jeon, T. Thorsen, et al., *Synth. Met.* **2003**, 139, 803.
- [25] V. N. Manoharan, A. Imhof, J. D. Thorne, et al., *Adv. Mater.* **2001**, 13, 447.
- [26] J. Wijnhoven, W. L. Vos, *Science* **1998**, 281, 802.

Chapter 10

Summary and Recommendations

This chapter summarizes the results achieved and presented in this thesis. Furthermore, several aspects are mentioned that can be useful for improvement of two-phase micro- and nanofluidics. Finally, some proposals for future research are formulated.

10.1 Summary

As defined in the project aims of this thesis, micro- and nanofluidic devices were investigated for the creation and manipulation of oil and water systems, and for the production of femtoliter-size droplets. Although two-phase microfluidics has obtained enormous attentions and has been applied and developed quickly in many fields since it was introduced in the 1990s, its use in micro- and nanofluidic devices is still in a nascent stage and leaves a large room for the development of reliability, controllability and stability. It remains therefore very important to understand and utilize micro- and nanofluidics fundamentals to design and develop improved micro- and nano-devices. We hope that the work presented in this thesis forms a small contribution in this process. (Chapters 1-3)

This thesis provides experimental data and theoretical analysis on two-phase flow in devices with different layouts of micrometer or nanometer-size channels. A full flow diagram is presented for oil and water flow in head-on microfluidic devices. Morphologically different flow regimes (dripping, jetting and threading) are observed over a broad range of capillary numbers: 10^{-6} ~ 10^{-1} . We have provided a theoretical framework to understand the different breakup mechanisms by considering the different forces acting in the system: capillary instability, squeezing and shearing. This head-on device provides us with the choice to generate droplet-based flow in regimes that are determined either by flow-rate or device geometry. At extremely low flow rates, we obtained a new droplet formation regime in which a droplet formation due to the device geometry is solely determined by capillary instability, independent on flow rates and liquid properties. We can thus determine the droplet volume in a very robust fashion by the design of the channel geometry. (Chapters 4 and 5)

The interfacial forces become dominant on downscaling due to the increasing in the surface area-to-volume ratio. To investigate the role of interfacial tensions in micro- and nanofluidics, we modulated solid-liquid and liquid-liquid interfacial forces. In microchannels, the emulsion types (oil-in-water or water-in-oil) are mainly

determined by the solid-liquid interfacial forces. By combination of different interfacial forces, we could obtain the designed emulsion type, determine droplet deformation, obtain coalescence and even emulsion conversion. The channel surface properties will be even more important if the dimension decreases further. Surface-determined flow phenomena may therefore be important to explain fluid transfer in some biological processes and to estimate interfacial properties. (Chapter 6)

The strong confinement and flow resistance in nanochannels challenges high pressure and low flow rate fluidic interconnections. We developed a flow control method to smoothly manipulate liquid in nanochannels with flow rates as low as $\text{pL}\cdot\text{s}^{-1}$. Using this method, we investigated the mixing of two miscible liquids and flows of two immiscible liquids in nanochannels. (Chapter 7)

An interface between a nanochannel and a microchannel has specific properties. In devices with nanochannel/microchannel interfaces, the creation of stable and monodisperse attoliter to femtoliter droplets was obtained at the nanochannel-microchannel interface in a wide range of flow rates and ratios. Considering the advantages of high surface area-to-volume ratio and small volume of these droplets, they can be applied as atto- or femtoreactors and single molecular containers. (Chapter 8)

Finally, microfluidic manipulation of fluids at the microscale enabled us to form and control liquid microspheres in three-dimensional lattices which are highly applicable in many fields: photonic crystal structures, liquid chromatography packings, data storage and so on. (Chapter 9)

In conclusion, we have demonstrated the extremely important role of interfacial energy in micro- and nanochannels. The solid surface energy (wettability) mainly determines emulsion types, and the liquid-liquid interfacial energy affects flow patterns in microchannels. Downscaling channel sizes further changes the order of pressures inside the system. The predominance of the capillary pressure (or Laplace pressure which is inversely proportional to the channel dimension) leads us to have explored geometrically determined droplet formation regimes (monodisperse and stable), especially in nanochannels. Micro- and nanofluidic devices can not only create small droplets but also control them to flow or organize into stable structures.

Therefore, for different purposes, it is highly required to precisely understand and design suitable micro- and nano-structures (or networks).

10.2 Recommendations and Proposals for Further Investigations

10.2.1 Materials









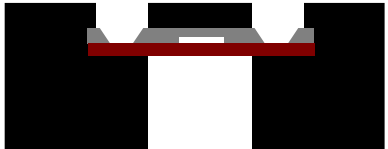
The material choice is the most important issue before starting experiments. The materials nowadays mostly used for chip fabrication are PDMS, glass and silicon. We will discuss these materials now.

10.2.1.1 Wettability

To study the micro- and nanofluidics of the two phases, water and oil, the channel surface wettability is critical for different applications. As we have demonstrated, the emulsion type is mainly determined by the channel surface wettability for the water or oil phase. PDMS $((\text{H}_3\text{C})_3\text{SiO}[\text{Si}(\text{CH}_3)_2\text{O}]_n\text{Si}(\text{CH}_3)_3)$ typically presents an external hydrophobic surface. This surface chemistry makes it difficult for polar solvents (such as water) to wet its surface, but hydrophobic solvents (such as organic solvent) can wet the surface. Therefore water-in-oil emulsions are typically obtained in PDMS microchannels without extra treatment. Many organic solvents can diffuse into the material and cause it to swell, which will then be incompatible with water/organic solvent two-phase flows. Silicon and glass show hydrophilic properties due to the silanol (SiOH) groups on the surface. Typically, oil-in-water emulsions can be obtained in glass or silicon microchannels. The glass and silicon surfaces can be functionalized by reacting with trichlorosilanes to become hydrophobic. Therefore, water-in-oil flow can also be obtained in glass or silicon microchannels. These factors make glass or silicon a more suitable material for micro- or nanochannel devices for the study of two-phase micro- and nanofluidics.

10.2.1.2 Fabrication

Table 10.1 The basic chip fabrication scheme.

Steps	Process description	Cross-section after process
A	Selecting wafers: silicon or glass	
B	Marking and Cleaning	
C	Lithography	
(a)	Coating photoresist	
(b)	Exposing and Developing	
(c)	Etching Si: dry etching Glass: wet etching	
(d)	Resist Stripping	
D	Powder Blasting (from backside)	
E	Cleaning and Bonding Si-glass: anodic bonding Glass-glass: thermal bonding	
F	Dicing and Fixing a Chip in a Holder	

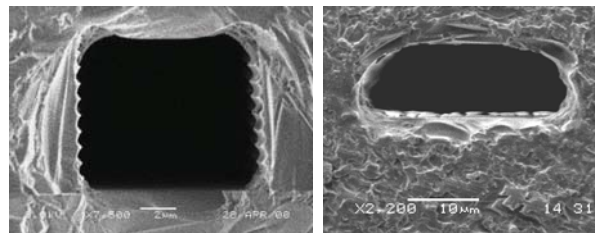


Figure 10.1 SEM (scanning electron microscope) images of cross sections of channels fabricated using dry etching in Si (left) and wet etching in glass (borofloat) (right).

For the study of nanofluidics, the material must be easy for nanofabrication. Silicon and glass are both hard materials which are not deformable. Also, many cleanroom processes have been developed to fabricate complicated devices from silicon or glass. Channels, with sizes as small as 10 nm, can be fabricated in glass or silicon. A PDMS device is typically made using soft lithography. It is cheap but the obtainable channel size is typically in the micrometer range and the controllability is poor. Furthermore, PDMS is deformable and permeable. It is thus incompatible for the application of very low or high pressure (flow rate).

Therefore, I would like to recommend using silicon or glass for nanofluidics study. The basic fabrication scheme is show in Table 10.1, and Fig. 10.1 shows the typical dry and wet etched channel cross sections.

10.2.2 Chip design

Many points should be considered when designing a chip for a two-phase flow, for instance the fabrication process (isotropic or anisotropic etch), the filters for liquid introduction, the entrance length, the size of the interconnection holes, and many others. A special issue when studying two-phase nanofluidics is the high hydrodynamic flow resistance. Water is hydrophilic and spontaneously fills into the hydrophilic nanochannels due to the capillarity. However, the oil phase (organic solvent) does not enter the channel until the applied pressure is above the capillary pressure which is very high in the nanochannel (it is up to 10 bar in 100 nm channels!). The conventional pressure-driven flow, simply applying pressure from a syringe directly to a nanochannel, is therefore difficult. It is furthermore difficult to obtain a volume flow rate of less than one $\mu\text{L}\cdot\text{min}^{-1}$, and it takes a very long time to replace the liquid due to the relatively large dead volume. This problem can be solved by the design of an integrated flow control system using a microchannel connected to a nanochannel to regulate the flow rate in the nanochannel (see chapter 7). A flow control system such as this or a variant is therefore recommended for nanofluidics studies.

10.2.3 Proposals

10.2.3.1 Single Molecular Study

Microfluidic and nanofluidic devices can be used to manipulate fluids in a controllable way. We have managed to create and control droplets with diameters from 700 nm to more than 10 μm using nano- and microfluidic devices, as demonstrated in Chapters 4~8. These attoliter to femtoliter droplets (100 aL~1000 fL) are small containers which will on average encapsulate one molecule per droplet if the analyte concentration is in nM. Single molecular studies could then be realized by using these small compartments, as shown in Fig. 10.2.

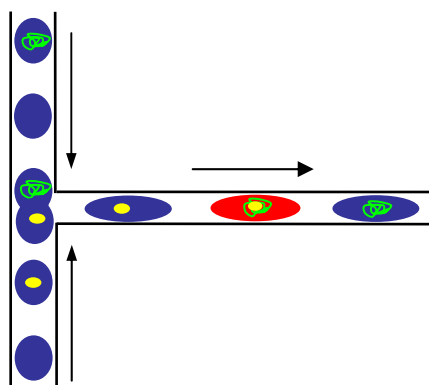


Figure 10.2 A schematic of the study of a single molecular reaction in an attoliter droplet. The two molecules (yellow and green) remain stable inside the original droplets, but show chemical, optical or electrical property changes when they contact and react.

10.2.3.2 Liquid Chromatographic Packing



Figure 10.3 A schematic of a chromatographic column of packed microdroplets used for the separation of different components (blue, red and yellow).

Microfluidic devices are not only ideal for manipulation of fluids but also for control of structures at the microscale. As we have demonstrated in Chapter 9, the small size (nm~ μm) liquid droplets could self-organize to form closely packed 3D structures in microchannels. The rigid and stable 3D structures themselves could be a good candidate for a chromatographic separation matrix due to the highly regular structure, preventing band broadening due to unequal pathways. The structures could be used as such, providing a lipophilic stationary phase and a hydrophilic mobile phase. Furthermore, the solidification (polymerization) of either the microdroplets or the continuous phase would offer a promising approach in producing a mini chromatographic column, as shown in Fig. 10.3.

Many application-driven experimental studies have demonstrated enormously promising applications of two-phase microfluidics in emulsification, encapsulation, microreaction, synthesis, bioassays and so on. On the basis of our experiments we dare saying that two-phase micro- and nanofluidic devices can become promising tools not only for designing functional devices but also for understanding fundamental physics of fluids and interfacial phenomena.

Acknowledgements

Coming from the Master degree in Colloid and Interface Chemistry, I was very interested in learning how water and oil make friends or fight to each other when confined in a very small device in which the surface area-to-volume is extraordinary high. This was the beginning of my journey at Twente, a journey that took me through a wide range of disciplines and a large number of laboratories. At BIOS, in Twente, I really learned about the meaning of collaboration as I struggled to learn physics and to catch technologies. Without the support and guidance of numerous people, this thesis would have never been completed. Here, I would like to express my deepest gratitude and thank all those who helped me.

My first and deepest appreciation certainly goes to my daily supervisor, Jan (Jan C. T. Eijkel) who gave me the opportunity to come to work in BIOS group. Without you many things may not be possible for me. You are always nice and kind to everyone, which makes me feel at home. The freedom and trust you offered me is really something to me. I still remember that you once told me that you assisted me to learn and finish my project instead of supervising. Thank you for your constant support not only in science but also in life. The extraordinary and multidisciplinary knowledge you possess, together with honesty, experience and kindness make you a person with whom work is nothing else but a pleasure.

My special thanks are addressed to Albert (Prof. Albert van den Berg). Thank you for being my promoter. I benefited a lot from your shining ideas during conversation although I could not catch them at the beginning. I wish I could do the same as you in the future. Much fun and happiness (biking and barbecues at Nijverdal, Christmas sports and dinners, the summer and winter workweeks...) in BIOS impressed me a lot; I really enjoyed them very much.

If someone asks me the best thing in BIOS group, I would say that is the great and

Acknowledgements

powerful technicians here. Daniel, you are so nice and always there for helping us doing cleanroom work even you also need to learn new things. Thank you very much for all your support in working and translating Dutch documents for me. Johan, without you, I could never start my cleanroom work easily. You are so patient and careful. I would not be confident of my mask design without your check. I have learnt a lot from you. It is my pleasure to work with you. Jan van Nieuwkastele, you are so good at microscope and interconnections Thank you for being helping me with building up my setup. I believe I would suffer much more without your help. Paul, how can I get my setup and chemicals without you? Thank you for all your help.

I would like to give my very special thanks to Hermine. Since I am a foreign student you have done a lot of work (visa, insurance, tax...) for me. You are so patient and make everything go smoothly for me.

Severine, my roommate, we had many nice experiences of sharing not only the office but also hotel rooms. You offered me many helps even you were busy with your own work and life. Thank you very much!

Edwin and Eddy, your office is a cornucopia. I could get what I wanted (books, small tools, experimental tricks...) almost every time. Thank you, Edwin, for talking and offering me so many things which will leave in my memory forever. Eddy, you are much appreciated for nice talks and helping me with guiding AT students.

Georgette and Wouter Sparreboom, since we all work in the same flagship we had more time of sharing experiences. I am so happy to closely work with you. Iris, thank you for borrowing me the key when I was locked outside the office. Thank you, Ganesh, for being there when I looked around to find somebody to speak English. Working at BIOS group is all a pleasure. I enjoyed a lot working in such a multidisciplinary environment. Ad and Wouter O., thank for listening and solving problems for me. Loes, Floor, Mathieu and Iris, I appreciate and enjoyed all activities you organized. And Songyue, my roommate, thank you for sharing your computation skills with me. Thanks to all the BIOSers: Dietrich, Hans, Masood, Rerngchai, Arpita,

Acknowledgements

Evelien, Cathelijn, Rogier, Oscar and those former BIOSers: Bjorn, Christian, Li, Ana, Monica, Sebastiaan, Dorothy, Erik, Jurjen, Dragana, Anil, Wim, Jacob, Wojtek, Roald, Arjan, Steven, Celio, Joke, Svetlana, Ton..., as well.

To Sumita, many thanks to you! When you first arrived in Twente, I did not know you so much. But later, you showed me your enthusiastic attitude to life and work. I have learnt a lot from you. Thank you for inviting me to visit your nice group. I had a great time of cooking, eating, and playing with your cute little Tony. I also want to thank Prof. George Homsy (Bud) who have shown patient and great knowledge of fluidics to me. You taught me how to start a program from the beginning. It is my great pleasure to know you. Maria, Trent, Cherry, David and Tom, thank you all for giving me a very nice time in UCSB. I would like to thank all people I met in UCSB.

I would like to say “Thanks a lot!” to all my Chinese friends, without you my life here would be less fun and less colorful.

Mum and Dad, I am lucky to be your daughter. You leave me the freedom to make decisions in my life. No word can express my gratitude to you. I also thank you for bringing me my lovely sister and brother. We have a happy and perfect family. My special gratitude also goes to my parents-in-law and sister-in-law. To be the member of this family is my fortune. I wish all the best to you! The last but not the least gratitude goes to my dear husband, Mingliang. It is you who bring me so much happiness, is around me when I am ill, tell me to calm down when I am upset. Thank you for moving to Netherlands. My life can not be so beautiful without you.

Lingling

04. 2009

Publications

Book Chapters

Lingling Shui, Jan C. T. Eijkel, Albert van den Berg, “*Pressure Driven Two Phase Flows*”, *Encyclopedia of Microfluidics and Nanofluidics*, ISBN: 978-0-387-32468-5, 1736-1742 (2008).

International Journal Articles

Lingling Shui, Albert van den Berg, Jan C. T. Eijkel, “*Interfacial Tension Controlled W/O and O/W 2-phase Flows in Microchannel*” *Lab on a Chip*, **9**, 795-801 (2009).

Lingling Shui, S. Pennathur, J. C. T. Eijkel et al., “*Multiphase Flow in Lab on Chip Devices: A real Tool for the Future*” *Lab on a Chip*, **8** (7), 1010-1014 (2008).

Lingling Shui, Frieder Mugele, Albert van den Berg, Jan C. T. Eijkel, “*Geometry-controlled Droplet Generation in Head-on Microfluidic Devices*” *Applied Physics Letters*, **93**, 1531131-1531133 (2008).

Lingling Shui, Jan C. T. Eijkel, Albert van den Berg, “*Multiphase Flow in Micro- and Nanochannels*” *Sensors and Actuators B: Chemical*, 121 (1), 263-276 (2007).

Lingling Shui, Jan C. T. Eijkel, Albert van den Berg, “*Multiphase Flow in Microfluidic System-control and Applications of Droplets and Interfaces*” *Advances in Colloid and Interface chemistry*, 133 (1), 35-49 (2007).

Lingling Shui, E. Stefan Kooij, Albert van den Berg, Jan C. T. Eijkel, “*Liquid Crystallography: 3D Microdroplet Arrangements Using Microfluidics*”, *submitted*.

Conference Proceedings

Lingling Shui, E. Stefan Kooij, Albert van den Berg, Jan C. T. Eijkel, "*Liquid Crystallography in Microchannels*" The Proceedings of μ TAS2008. vol. 1, 125-127 (2008).

Lingling Shui, D. Wijnperle, Albert van den Berg, Jan C. T. Eijkel, "*The Effect of Interfacial Forces on 2-phase Microfluidics*" The Proceedings of μ TAS2008, vol. 1, 790-792 (2008).

Lingling Shui, Albert van den Berg, Jan C. T. Eijkel, "*Droplet Generation in Head-on Microfluidic Devices*" The Proceedings of μ TAS2007, vol. 2, 928-930 (2007).

Lingling Shui, Albert van den Berg, Jan C. T. Eijkel, "Two-phase Flow Control in Nanochannels", submitted.

Lingling Shui, Albert van den Berg, Jan C. T. Eijkel, "Monodisperse Droplet Formation Using Nano-Micro Channel", submitted.

